Doctoral Dissertation

LONG-TERM DISPLACEMENT MEASUREMENT OF FULL-SCALE BRIDGES USING COMPUTER VISION AND LIDAR

Junhwa Lee

Department of Urban and Environmental Engineering
(Urban Infrastructure Engineering)

Graduate School of UNIST

2020

LONG-TERM DISPLACEMENT MEASUREMENT OF FULL-SCALE BRIDGES USING COMPUTER VISION AND LIDAR

Junhwa Lee

Department of Urban and Environmental Engineering
(Urban Infrastructure Engineering)

Graduate School of UNIST

Long-Term Displacement Measurement of Full-Scale Bridges using Computer Vision and LiDAR

A thesis/dissertation proposal
submitted to the Graduate School of UNIST
in partial fulfillment of the
requirements for the degree of
Doctor of Philosophy

Junhwa Lee

May 8th, 2020
Approved by

_____

Advisor: Prof. Young-Joo Lee

_____

Co-Advisor: Prof. Sung-Han Sim

Long-Term Displacement Measurement of Full-Scale Bridges using Computer Vision and LiDAR

Junhwa Lee

This certifies that the thesis/dissertation is approved.

May 8th, 2020

_____

Advisor: Professor Young-Joo Lee

_____

Co-Advisor: Professor Sung-Han Sim

_____

Thesis Committee Member: Professor Myoungsu Shin

_____

Thesis Committee Member: Doctor Kyoung-Chan Lee

_____

Thesis Committee Member: Professor Sukhoon Pyo

Abstract

Bridge displacement is regarded as a key safety indicator that is widely adopted for structural health monitoring (SHM). Bridge structures deflect in response to applied loads and structural degradation. As extensive vibrations of bridges cause passenger's discomfort and accelerate structural degradation, modern societies take the bridge displacement into account in their design codes and regular maintenance protocols to ensure serviceability and safety of the bridge structures. The short-term displacement is generally employed in bridge SHM, together with the level of load carrying capacity. Even though the long-term displacement can also provide essential safety information, in addition to the short-term data, the long-term displacement monitoring of bridges is not commonly conducted owing to practical difficulties. The long-term monitoring of displacement using conventional displacement sensors, such as a linear variable differential transformer, laser displacement sensor, and radar, or indirect estimation methods, such as an acceleration-based method or multimetric sensor-based approaches result in errors, which typically accumulate over time. A limited number of research studies have addressed long-term bridge displacement measurement; however, the sensor drift can still cause errors in those measurements. This paper proposes long-term displacement measurement methods using computer vision and LiDAR, tailored to full-scale bridge structures. The computer vision-based approach compensates for the camera motion-induced errors by using an auxiliary camera and the long-term displacement can be achieved regardless of the camera movement. A LiDAR-based method is also presented, by which the long-term time history of the bridge displacement can be tracked by a temporarily installed LiDAR, thus eliminating the need for a permanent installation in the field. These two long-term measurement approaches were cross validated on a 40 m-long full-scale railway bridge under construction. Over a span of 650 days, these two methods showed a similar trend, thus validating the applicability of each method. Important structural information, such as immediate displacement due to dead load, long-term deflection due to creep, daily fluctuation due to temperature gradient, could potentially provide long-term displacement data in bridge health monitoring.

Contents

List of Figures

List of Tables

1. Introduction

1.1. Motivation and Scope of the Research

The long-term operation of civil engineering structures has led modern society to demand efficient structural management. Bridges are one of the most important civil infrastructures that have been massively constructed over the past decades such that their malfunctioning result in social and economic losses, including casualties, traffic chaos, and rehabilitation costs. However, bridges are prone to failures during the construction and operation phases. Even though structures are carefully designed according to the codes such as the Korean Design Standards (KDS) [1], the code by the American Association of State Highway and Transportation Officials (AASHTO) [2], and the Eurocode [3], construction failures occur mainly due to the misalignment or excessive deformation. Inappropriate maintenance measures during the long-term operation of the bridges also lead to structural failures [4-7] that has been frequently reported across the modern societies as shown in Figure 1. To prevent the social and economic losses caused by the structural failures, bridge owners need to employ efficient and effective methods of bridge maintenance.

(a) The Dale bend bridge in USA, a truss bridge built in 1930

(b) The Nanfang'ao bridge in Taiwan, an arch bridge built in 1998

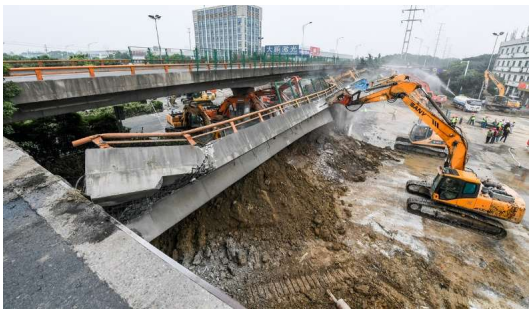

(c) The National highway 312 in China, a concrete bridge built in 2005

(d) The Mirepoix bridge in France, a suspension bridge built in 1931

Figure 1. List of bridges collapsed in 2019.

Structural health monitoring (SHM) is a maintenance process to assess the current condition of civil engineering structures during their lifetime. SHM involves three fundamental steps, namely data acquisition, extraction of structural features, and structural condition assessment [8-10] as summarized in Table 1. The data acquisition step is concerned with the type of physical quantities to be monitored as well as the sensor deployment strategy. In general, SHM for bridge structures employs an array of sensors over the structure, such as accelerometers [11-16], strain gauges [17-24], and displacement sensors [25-29], which are strategically deployed [30-32] in consideration of the structural behavior and deployment cost. Recent research studies have shown efficient, convenient, and cost-effective methods of SHM by employing a wireless data collection protocol [8, 10, 13, 14, 30, 32-37] that helps acquire multiple physical quantities at strategic points. The second step of SHM is to extract useful structural features from the raw sensing data. The vibration information is widely adopted to identify the structural modal property [8, 27, 38-41]. An embedded strain gauge within the bridge helps measure the stress [42-44]. Surface image data are employed in detecting structural defects, such as cracks, efflorescence, spalling, and corrosion [45-50]. Furthermore, recent advances in deep learning-based image classification techniques enable automatic visual inspection [51-53]. Damage detection and localization is a key procedure in SHM that can be directly used for condition assessment [54-58]. The state of a structure can be tracked by continually updating the mathematical dynamic models [59-61] or the finite element models [62-64] of the structure using the identified structural features. Finally, in the third step, the structural features are extensively gathered to evaluate the structural condition. Here, the rating methods are individually established by civil engineering organizations for qualitatively assessing structural condition [65-67]. As such, SHM is an effective tool for bridge maintenance, ranging from data acquisition to overall condition assessment.

Table 1. Components of the SHM.

SHM procedure	**Consideration**
Data acquisition	Choice of physical quantities Location of monitoring point
Extraction of structural features	System identification Damage detection Model updating
Structural condition assessment	Quantification of the structural condition

Displacement is regarded as a key safety indicator that can be adopted in SHM for effective bridge maintenance. Under given loading condition, the amplitude of the displacement is determined by the stiffness of the bridge. Thereby deteriorated structures experience larger deflections owing to a loss of stiffness from section losses or material degradations. The excessive deformation is closely related to the structural degradation; thus, modern societies take displacement into account in their design codes and regular maintenance protocols to ensure serviceability and safety. Design codes regulate deflection limits in association with load combinations. The deflection limits are prescribed based on the span length, as shown in Table 2, in which the most demanding criteria are listed for each design code [1-3]. In the case of railway bridges, deflection limits are further stated along with the train speed to assure passenger comfort, as shown in Table 3 [68]. The displacement induced by dead load is often adjusted by a time-dependent factor to accommodate long-term deformation from creep and shrinkage. For example, to accommodate long-term deformation of a bridge without reinforcement that is used

Table 2. Deflection limit for bridges in design codes.

Code	**Deflection limitation**	**Load condition**
KDS [1]	$L/1000$	Normal vehicle and pedestrian load
AASHTO [2]	$L/1000$	Normal vehicle and pedestrian load
Eurocode [3]	$L/500$	Quasi-permanent loads that can cause damage adjacent parts of the structure

※ L: span length

Table 3. Deflection limit for railway bridges in Korea to assure passenger comfort.

Train speed (km/h)	**Span length (m)**										
	0–20	25	30	35	40	45	50	55	60 –75	80 –95	100– 120
0–200	$\frac{L}{1500}$	$\frac{L}{1500}$	$\frac{L}{1600}$	$\frac{L}{1750}$	$\frac{L}{1900}$	$\frac{L}{2100}$	$\frac{L}{2200}$	$\frac{L}{2350}$	$\frac{L}{2500}$	$\frac{L}{2200}$	$\frac{L}{1900}$
200–270	$\frac{L}{1300}$	$\frac{L}{1400}$	$\frac{L}{1500}$	$\frac{L}{1600}$	$\frac{L}{1700}$	$\frac{L}{1900}$	$\frac{L}{2000}$	$\frac{L}{2100}$	$\frac{L}{2000}$	$\frac{L}{1700}$	$\frac{L}{1400}$
270–350	$\frac{L}{1100}$	$\frac{L}{1200}$	$\frac{L}{1300}$	$\frac{L}{1500}$	$\frac{L}{1500}$	$\frac{L}{1400}$	$\frac{L}{1300}$	$\frac{L}{1200}$	$\frac{L}{1100}$	$\frac{L}{800}$	$\frac{L}{600}$

※ L: span length

over 5 years, the displacement induced by dead load is multiplied by a time-dependent factor of 2 according to KDS [1]. During the operation stage, displacement is regularly examined along with loading test to identify load carrying capacity. As such, the bridge displacement is a widely adopted safety indicator; hence, an efficient displacement measurement method for full-scale bridge structures is necessary for an effective SHM.

Long-term displacement has been limitedly employed in SHM due to difficulty in its measurement. Previous research works have shown successful application of short-term displacement measurement methods in full-scale bridge structures, most of which measure bridge displacement during a loading test. On the other hand, long-term monitoring of displacement is challenging for full-scale bridges. If the sensor system needs to occupy underpass of the bridge, permanent installation of a sensor in the field can be impractical because of traffics. Displacement sensors that can be placed at an arbitrary position are prone to drift error due to continuous sensor motion under harsh field environment. In addition, permanent installation is not desirable for an expensive displacement monitoring system. Due to the practical limitations, most of SHM considers short-term displacement in condition assessment. Considering that the long-term displacement of bridge provides important information about structural integrity such as tendon loss, section loss, and fatigue, practical long-term monitoring solution needs to be developed.

This dissertation presents novel methods of long-term displacement measurement by using computer vision and LiDAR. Computer vision-based method compensates for the drift error induced by camera movement. LiDAR-based method can measure long-term displacement without permanent installation of the sensor in the field such that no drift error is expected. These two methods are cross validated in a full-scale railway bridge under construction. Not only the immediate displacement induced by the superimposed dead load, but also the long-term variation from creep, shrinkage, and thermal fluctuation were successfully measured.

1.2. Dissertation Overview

This dissertation focuses on the development of long-term displacement measurement systems by using computer vision and LiDAR. Chapter 1 discusses the motivation and objective of the dissertation. Chapter 2 reviews conventional displacement measurement methods with their limitation in long-term application. Chapters 3 and Chapter 4 demonstrate the proposed long-term displacement measurement systems by using computer vision and LiDAR, respectively. Chapter 5 validates the proposed methods in the field using a full-scale railway bridge. Finally, Chapter 6 summarizes the contributions of the research work.

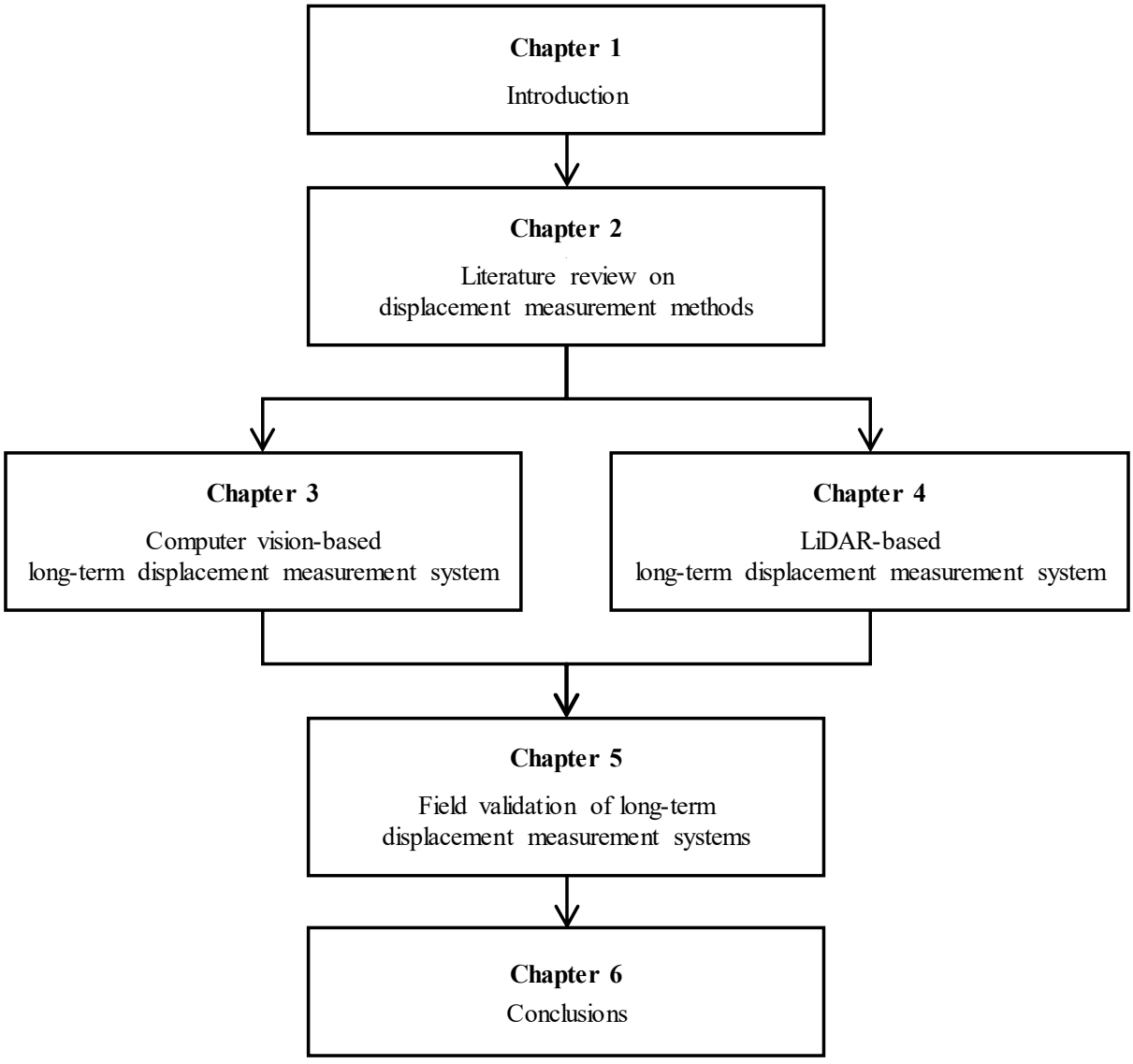

Figure 2. Dissertation overview.

2. Literature Review on Displacement Measurement Methods

2.1. Displacement Measurement Methods

Previous literatures have reported various types of displacement measurement method for full-scale bridges, which can be categorized as indirect estimations and direct measurements, as listed in Table 4. The indirect estimation approach converts other structural responses into displacement. Herein, spatiotemporal derivative of the displacement, such as acceleration and strain, is measured and numerically integrated over time or space to recover displacement. On the other hand, the direct measurement method utilizes a displacement sensor without need for integration. Due to the intuitive measurement procedure, the direct method is often employed in full-scale applications, in which a campaign-type measurement scheme is required by placing a temporary structure such as scaffold under the bridge. Recent research has focused on the development of advanced displacement measurement methods tailored to full-scale bridges, by which sub-mm level of displacement can be remotely acquired without need for underpass occupation. This chapter presents fundamental principles of the existing displacement measurement methods along with performance in field applications.

Table 4. List of displacement acquisition method.

Category	Methods
Indirect estimation	➢ Temporal derivative data-based method ➢ Spatial derivative data-based method ➢ Spatiotemporal derivative data-based method
Direct measurement	➢ Linear variable differential transformer (LVDT) ➢ Ring gauge ➢ Draw wire displacement sensor ➢ Phase-shift-based laser displacement sensor ➢ Time-of-flight-based displacement sensor ➢ Triangulation-based laser displacement sensor ➢ Global navigation satellite system (GNSS) ➢ Hydraulic level meter ➢ Range meter with rotation encoder ➢ Computer vision ➢ Light detection and ranging (LiDAR)

2.1.1. Indirect displacement estimation approaches

The indirect method estimates vertical displacement of bridge structures from the spatial and temporal derivatives of the displacement. Consider that the bridge displacement $v(x,t)$ is a function of time t and spatial location x as shown in Figure 3. Bridge displacement can be computed by using a temporal derivative, such as velocity and acceleration, that is numerically integrated over time to recover displacement. Herein, the signal is assumed to be a zero-mean process, otherwise truncation error is accumulated over time. Spatial derivatives of the displacement, such as rotation and curvature, can be used to calculate displacement at any x. A shape function is assumed, which is spatially integrated to formulate relationship between the spatial derivatives and the displacement. Strain can also be adopted in the indirect displacement estimation with an assumed neutral axis and shape function. Denoting y as the location of the strain gauge with respect to the neutral axis, curvature can be computed by dividing y from the strain. The curvature is then used to recover displacement by using the assumed shape function. Spatiotemporal derivatives of the displacement, such as angular velocity, can be utilized along with zero-mean process and the assumed shape function. As such, the indirect methods recover displacement from the displacement derivatives.

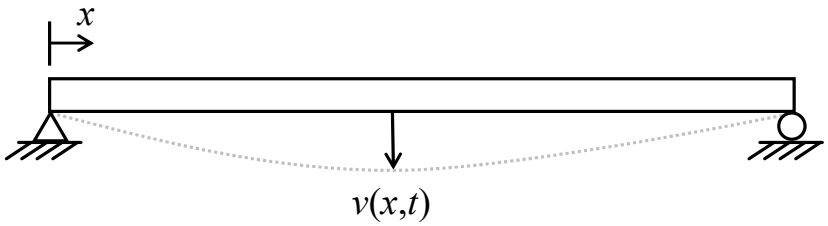

Figure 3. Bridge displacement illustration.

Table 5. Indirect displacement estimation methods.

Physical quantity	**Notation**	**Assumptions**
Velocity	$\partial v(x,t)/\partial t$	Zero-mean process
Acceleration	$\partial^2 v(x,t)/\partial t^2$	Zero-mean process
Rotation	$\partial v(x,t)/\partial x$	Assumed shape function
Curvature	$\partial^2 v(x,t)/\partial x^2$	Assumed shape function
Strain	$\partial^2 v(x,t)/\partial x^2 \cdot y$	Assumed shape function and neutral axis location
Angular velocity	$\partial^2 v(x,t)/\partial x \partial t$	Zero-mean process and assumed shape function

Existing literatures have reported novel indirect displacement estimations tailored to full-scale bridges. Acceleration is widely adopted in the indirect method due to the cost effectiveness and convenience in sensor installation. Double integration of the acceleration results in displacement [69], whereas numerical integration error is accumulated over time because the sensing data is discrete. To remove the low-frequency drift related to the integration error, Lee et al. [70] proposed a dynamic displacement estimation method by removing low-frequency components below the first natural frequency. This method results in zero-mean displacement that often fail to recover pseudo-static displacement component. Rotation-based approaches employs rotation at the supports for simply-supported bridges [71]. The displacement is computed as

$$d(x) = \frac{l^2 - x^2 - a^2}{l^2 - a^2}\theta x \tag{2.1}$$

where $d(x)$ is structural displacement at position x, l is the span length of the bridge, a is the position that load is applied with respect to the support, and θ is the rotation at the support. This method, however, can incorrectly estimate the displacement if the actual shape function is different from the assumed polynomial function. Curvature-based displacement estimation method [72, 73] utilizes at least two strain gauges along the height of the girder to calculate curvature. Note that location of neutral axis needs to be assumed to recover the curvature from the single strain gauge. Once the curvature is computed, displacement is computed as

$$d(x) = \int\int_0^x \kappa(\alpha) d\alpha^2 \tag{2.2}$$

where $\kappa(x)$ is curvature at x. Sinusoidal dynamic mode shapes are typically employed as the shape function [74]. This curvature-based method can estimate the pseudo-static displacement. However, displacement can be incorrectly estimated because of discrepancy in the assumed neutral axis or in the assumed shape function from the actual bridge model. To better recover displacement, multimetric data fusion algorithm has been developed by using multiple physical quantities such as strain-acceleration [75] and strain-rotation [76]. As such, indirect method is a promising displacement monitoring solution if the assumptions such as zero-mean process, shape function, and neutral axis are valid for real structures.

2.1.2. Direct displacement measurement approach

Various types of displacement sensors are employed in condition monitoring of full-scale bridges. Unlike the indirect estimation approaches, the direct measurement method requires a stationary reference point. Based on the difficulty in preparing the reference point, the displacement sensors are categorized into four groups as shown in Table 6. The first category is the contact-type sensor with occupation of the underpass of the bridge, such as LVDT, ring gauge, and draw wire displacement sensor. Temporary structure (e.g. scaffold) is necessarily prepared to reach a tip of sensor to the bottom of the bridge. The second category needs underpass occupation whereas temporary structure is not necessary that provides convenient system installation in the field. The sensor in the third category leaves the underpass of the bridge empty, which is the basic requirement for the long-term displacement monitoring. Because the contact-type sensor is deployed at a point where traffic load is likely to occur, the sensing system requires careful management. The sensor in the fourth category offers a remote displacement measurement without need for underpass occupation, which is the promising solution for long-term monitoring of full-scale bridges. This chapter presents the fundamental principles of the sensors for each category, discussing the pros and cons in practical applications.

Table 6. Displacement measurement sensors.

Category	**Displacement sensor**
1. Contact-type with underpass occupation	➢ LVDT [77, 78] ➢ Ring gauge [79, 80] ➢ Draw wire displacement sensor [81, 82]
2. Noncontact-type with underpass occupation	➢ Phase-shift-based displacement sensor ◦ LDV [83-86] ◦ Radar [87-90] ➢ ToF-based displacement sensor ➢ Triangulation-based laser displacement sensor [91, 92]
3. Contact-type without underpass occupation	➢ GNSS [93-97] ➢ Hydraulic level meter [98]
4. Noncontact-type without underpass occupation	➢ Range meter with rotation encoder ◦ Total station [99-101] ◦ Laser tracker [102] ◦ LiDAR [103, 104] ➢ Computer vision [105]

(1) Category 1: Contact-type with underpass occupation

Sensors in the category 1 are widely adopted for displacement monitoring of full-scale bridge structures. Three major sensors are introduced, which are LVDT [77, 78], ring gauge [79, 80], and draw wire displacement transducer [81, 82]. LVDT consists of a primary winding, couple of secondary windings, and a movable magnetic core as shown in Figure 4(a). The voltage level in the secondary winding have linear relationship with the location of the magnetic core based on the mutual inductance principle. Thereby, movement of the core is synchronized with the structural displacement by contacting the core tip to the bottom of the bridge. Ring gauge has a round plate spring of which deformation has linear relationship with the displacement. Once the gauge is firmly fixed on the ground, a steel wire connects the round plate to the bridge as shown in Figure 4(b). The plate deformation is measured by the attached strain gauges such that displacement is computed from the acquired strain. Draw-wire consists of wire, wire drum, and rotary encoder as shown in Figure 4(c). The amount of winding of the wire is proportional to the displacement, which is recorded by the rotary encoder. The resolution of the sensor is determined by the circumference of the wire drum as well as the resolution of the rotary encoder. Such sensors use precise electromechanical relationship; thereby displacement can be measured with high precision. Sensors in the category 1 are widely adopted in field applications because of the intuitive working principle and inexpensive system cost.

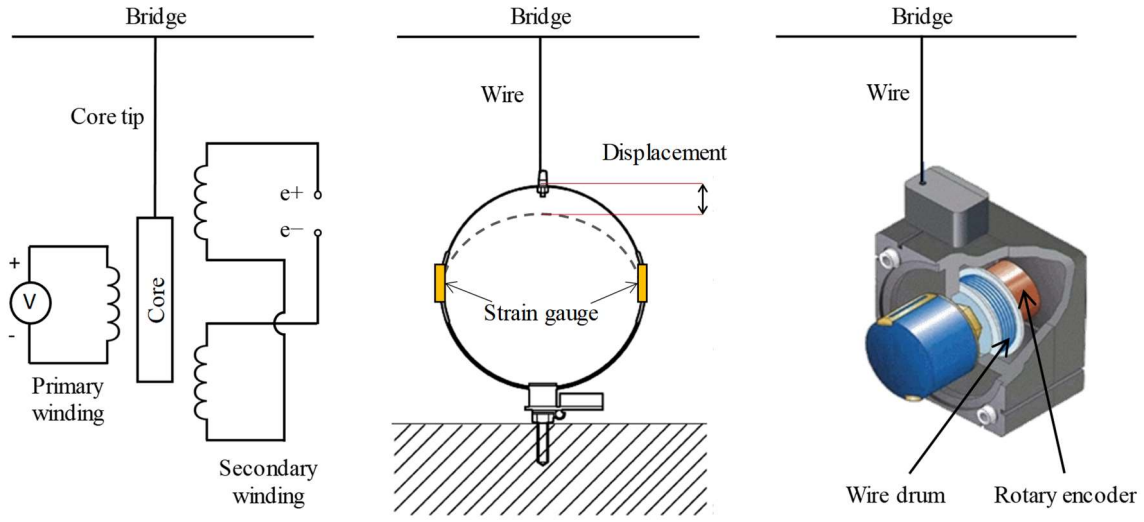

(a) Component of LVDT (b) Component of ring gauge (c) Component of draw wire

Figure 4. Component of displacement sensors in category 1.

Even though the sensors in the category 1 provide sub-mm level of displacement resolution, physical contact of the sensor to the bridge is in general impractical for field applications. As can be seen in Figure 5, temporary structures such as scaffold is necessary in displacement measurement, which needs traffic intervention. In addition, careful protection such as windshield is required for the temporary structures to avoid sensor vibration. As such, category 1 sensors have practical limitation in terms of inefficient sensor installation.

(a) Field application of LVDT

(b) Field application of ring gauge

Figure 5. Field applications of displacement sensors in category 1.

(2) Category 2: Noncontact-type with underpass occupation

Sensors in the category 2 provide a simple installation procedure without need for contact to the bridge. The most widely adopted sensors are introduced, which are respectively based on the phase shift, the triangulation principle, and the Time-of-Flight (ToF). Phase shift-based sensors measure displacement based on the Doppler shift principle which states that frequency and phase information of a wave change in relation to the movement of the target. As shown in Figure 6(a), displacement of a moving object can be obtained as

$$d = \frac{\lambda \Delta\phi}{2} \tag{2.3}$$

where d is the displacement of the moving object, λ is the wavelength of the transmitted wave, and $\Delta\varphi$ is the phase shift. Given the wavelength of the wave, the phase-shift-based sensors can measure the displacement. For example, LDV sensor, a well-known phase-shift-based sensor, utilizes infrared laser with the wavelength of 4×10^{-7}–7×10^{-7}m [83-86]. Triangulation-based sensor [91, 92] measures displacement by emitting a laser and receiving the reflected one by using tilted charge-coupled device (CCD) array as shown in Figure 6(b). The displacement can be calculated as

$$d = \frac{ax'\sin\eta}{b\sin\beta - x'\sin(\beta+\eta)} \tag{2.4}$$

where x' is the image point displacement on the CCD array, a and b are the distance from the receiving lens to the reference surface and CCD array, respectively, β is the reflection angle between the emitted and reflected laser, and η is the tilt angle of the CCD array with respect to the reflected laser. Because a, b, β, and η can be known before the measurement based on the manufacturer's specifications, displacement can be computed from x'. ToF is a range measurement method by using an artificial light signal as shown in Figure 6(c). By counting the time delay since light emission until receiving the signal, displacement can be computed by using the speed of light which is known to be approximately about 300,000 km/s. As such, sensors in category 2 can provide convenient procedure for the sensor installation by using light beam.

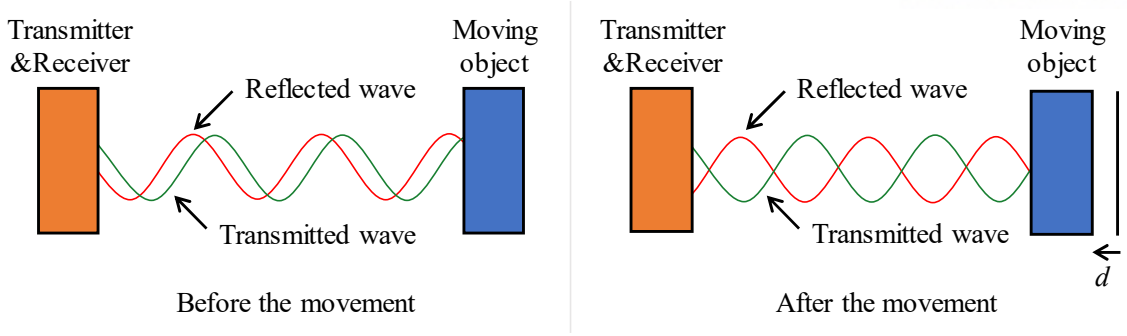

(a) Illustration of phase shift induced by displacement

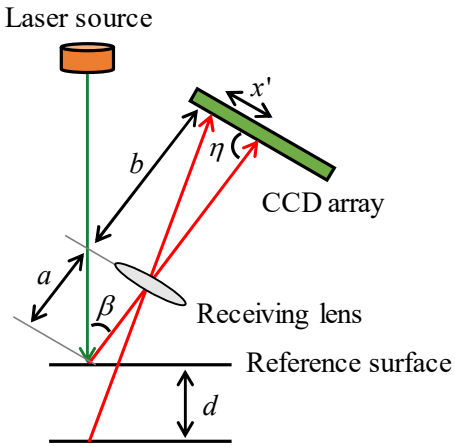

(b) Illustration of laser triangulation

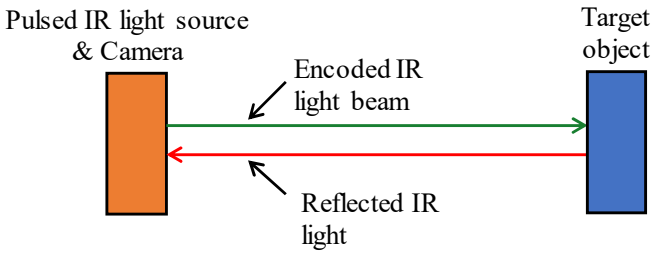

(c) Illustration of ToF sensor

Figure 6. Principle of the sensors in category 2.

Even though the sensors in the category 2 provides simple installation procedure for field applications, the device needs to be placed under the bridge to align the transmitting light along the line of displacement. Because the sensors are deployed under the bridge, traffic needs to be blocked as shown in Figure 7. In case of phase shift-based and ToF-based methods, displacement can be measured at a distance from the target surface such that the sensor can be placed on the ground. On the other hand, triangulation-based method requires proximity. Otherwise, the reflected laser escapes from the CCD array. As such, displacement measurement using the category 2 sensors provides simple installation step, whereas the traffic intervention is required.

(a) Field application of LDV, a phase shift-based displacement sensor

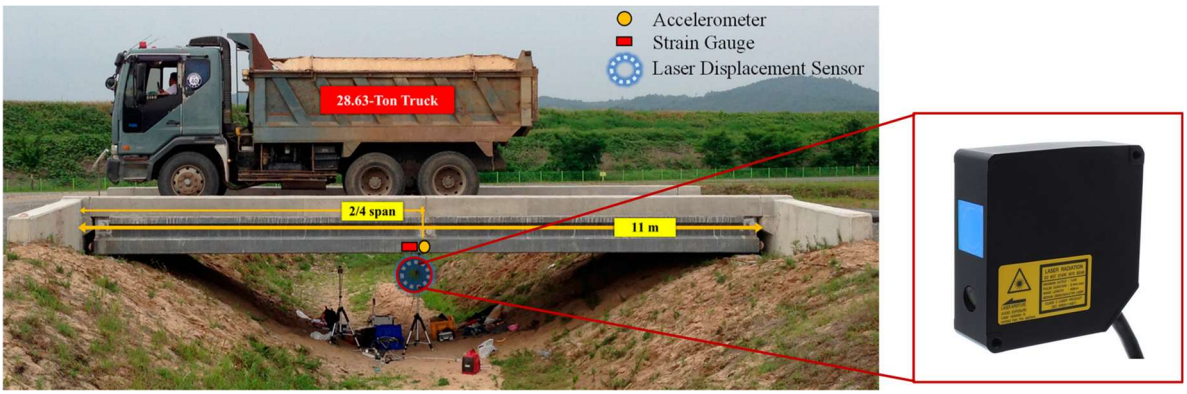

(b) Field application of the triangulation-based laser displacement sensor [92]

Figure 7. Field applications of the sensors in category 2.

(3) Category 3: Contact-type without underpass occupation

Sensors in the category 3 are deployed at the point the displacement is required without underpass occupation. The most widely adopted sensors are global navigation satellite system (GNSS) [93-97] and hydraulic level meter [98]. Given the configuration as shown in Figure 8(a), GNSS receiver can find the location with respect to the satellites by solving a minimization problem given by

$$\min_{x} \sum_{i=1}^{n} \left\| \|x - x_i\|_2 - r_i \right\|_2 \tag{2.5}$$

where x is three-dimensional location of the GNSS receiver with respect to the satellites, n is the number of satellite involved, $\|\cdot\|_2$ is two-norm notation, x_i is the three-dimensional location of the satellite, and r_i is the range measurement from the i-th satellite. Because x_i is given for every satellite, three dimensional displacements can be computed by using the range measurements. Second sensor is Hydraulic level meter that measures displacement by recording the water level against the reference vessel as shown in Figure 8(b). By deploying series of hydraulic meter along bridge, global displacement can be obtained by the level differences. Therefore, sensor in category 3 do not occupy the underpass by measuring their position relative to the reference.

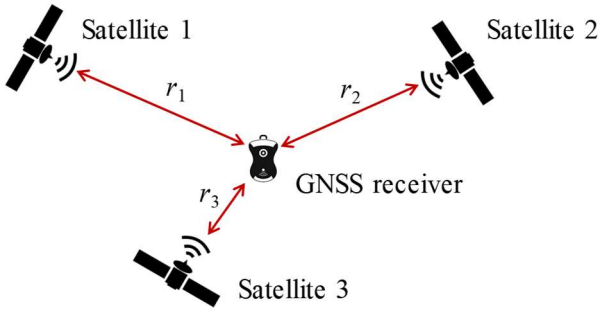

(a) Configuration of GNSS (r_i: range between the GNSS receiver and the i-th satellite)

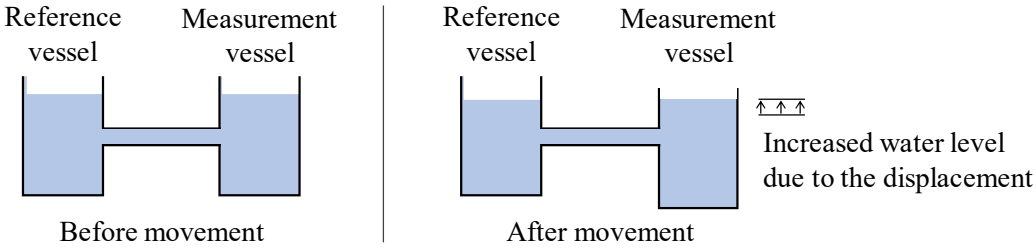

(b) Principle of hydraulic level meter

Figure 8. Principle of the sensors in category 3.

Sensors in the category 3 has been applied to full-scale civil infrastructures. State of the art GNSS sensors provide 20 mm of vertical displacement resolution [25], which is not enough for structural health monitoring of short- and medium-span bridges. In that reason, GNSS sensors are mostly applied to displacement monitoring of long-span bridges as shown in Figure 9 with relatively large structural responses. Hence, recent researches focus on improving the displacement resolution of the GNSS by combining with other sensors such as acceleration [106, 107].

(a) Evripos bridge in Halkida, Greece [108]

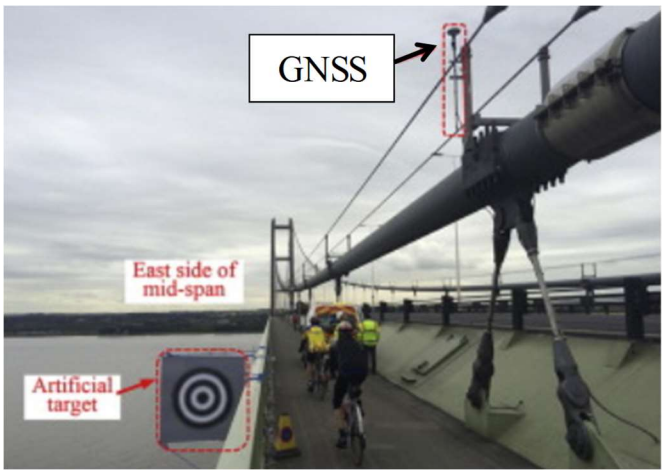

(b) Humber Bridge in Hessle and Barton, United Kingdom [109]

Figure 9. Field application of the GNSS sensor.

(4) Category 4: Noncontact-type without underpass occupation

Sensors in the category 4 are the most promising solution for displacement measurement of full-scale bridges. Compared to the sensors involved with underpass occupation (i.e. Category 1 and 2), the category 4 leaves the space under the bridge empty; thereby displacement can be measured during the regular traffic operation. In addition, unlike the category 3, the sensor is not fully exposed to traffic loads, which helps to maintain the sensor in sound condition for a long period of time. The category 4 is extensively reviewed due to the potential for field applications.

Laser-based three-dimensional displacement sensors, such as total station [99-101], laser tracker [102], and LiDAR [103, 104, 110], can be used for condition monitoring of full-scale bridges. Using a laser, the range to a target point is measured via time of flight method as described in the category 2. The laser is rotated about vertical and horizontal axes, of which angles are measured by a rotary encoder. The range and two angular information are combined to build a spherical coordinate that is the three-dimensional position of the target. Total station and laser tracker are the single point measurement tool as shown in Figure 10 that keep track of three-dimensional position of a retroreflector. On the other hand, LiDAR measures the 3D coordinates of a surrounding scene by scattering distance-measurable light at regular spatial intervals. Here, LiDAR is often equipped with rotating mirror as shown in Figure 11(a) for the rapid scattering of the light. The 3D coordinate information is collected to construct a point cloud of object such as entire bridge as shown in Figure 11(b). Even though the sensors are expensive due to the complex mechanism, three-dimensional information can be acquired by simply placing the sensor in the category 4 at a stationary point near the bridge.

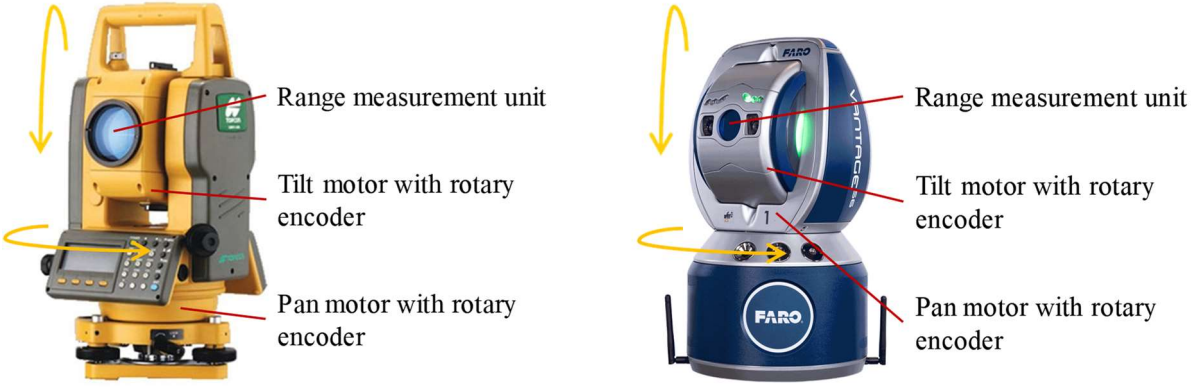

(a) Total station (b) Laser tracker

Figure 10. Three-dimensional displacement measurement sensors.

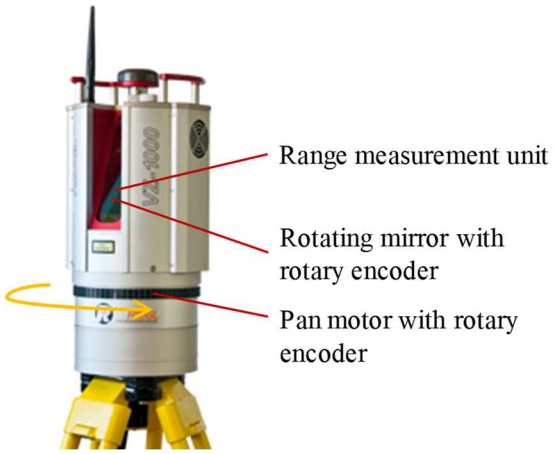

(a) LiDAR configuration

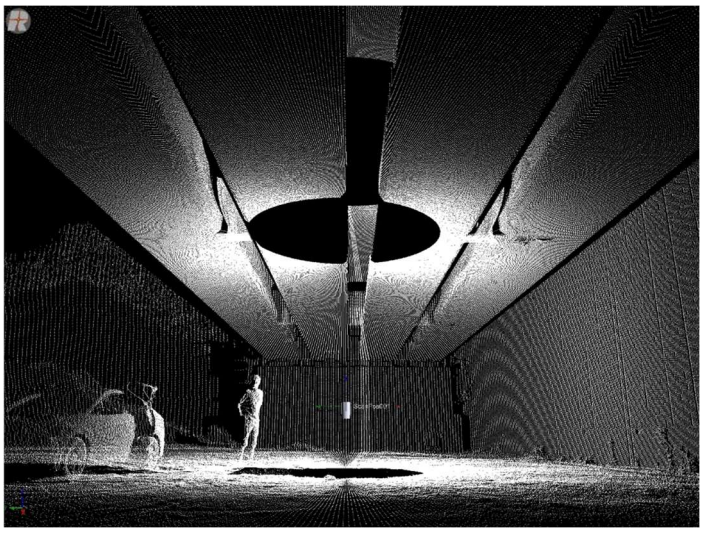

(b) Three-dimensional point cloud of a bridge

Figure 11. Three-dimensional point cloud measurement sensor.

The laser-based sensor in the category 4 has been applied to displacement measurement of full-scale bridge. Robotic total station can be employed as shown in Figure 12, in which retroreflective prism is installed at the midspan and total station measures the three-dimensional position. In case of LiDAR, entire bridge was scanned to collect 3D shape of the bridge before and after a loading condition. Using two three-dimensional point clouds, displacement for each point is calculated by a point matching scheme such as iterative closest point algorithm [110]. By analyzing the displacement for each point, displacement was able to be computed. The conventional approaches show potential of the laser-based three-dimensional displacement measurement with simple installation and underpass occupation-free.

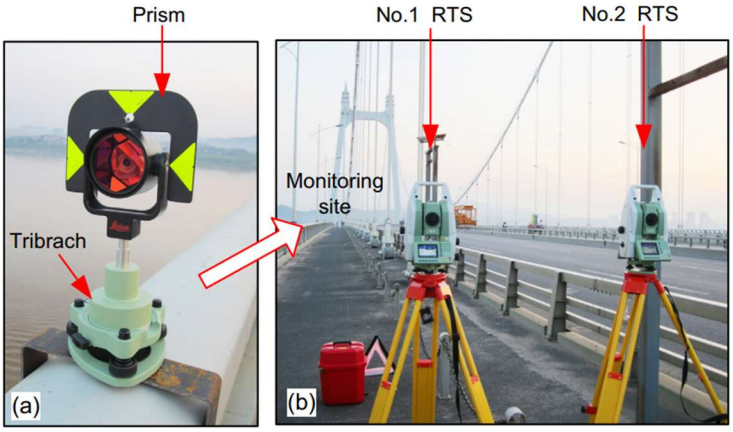

(a) Displacement measurement using a robotic total station [111]

(b) Displacement measurement during a load test using LiDAR [103]

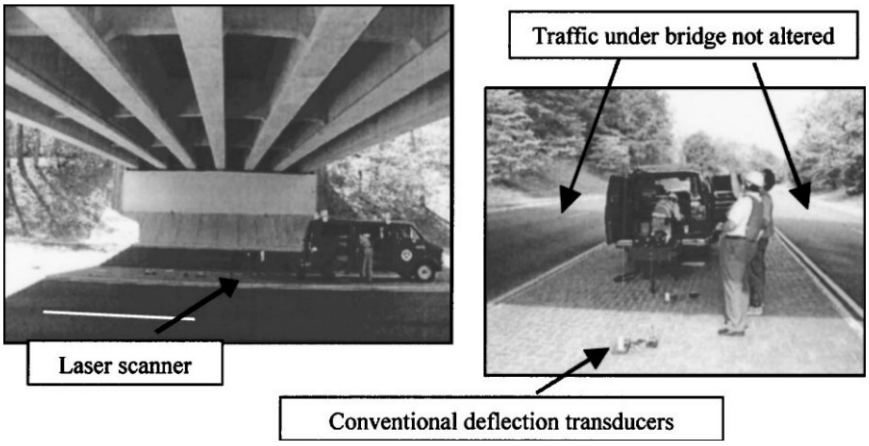

(c) Displacement measurement during a load test using LiDAR [104]

Figure 12. Displacement measurements by using total station and LiDAR.

Another category 4 sensor is computer vision. Vision-based displacement measurement methods typically consist of hardware and software components (see Figure 13). The hardware part can be prepared with a camera, a computer for data acquisition and processing, and a user-defined target marker. The marker movement, which represents structural displacement, are recorded by the camera and transferred to the computer simultaneously. Using the captured video frames, structural displacement is calculated via an image-processing for feature detection and coordinate transforms from pixel-level displacement to physical quantity. Computer vision can be easily employed in displacement measurement of full-scale bridge providing sub-mm resolution with inexpensive system cost.

(a) Hardware configuration

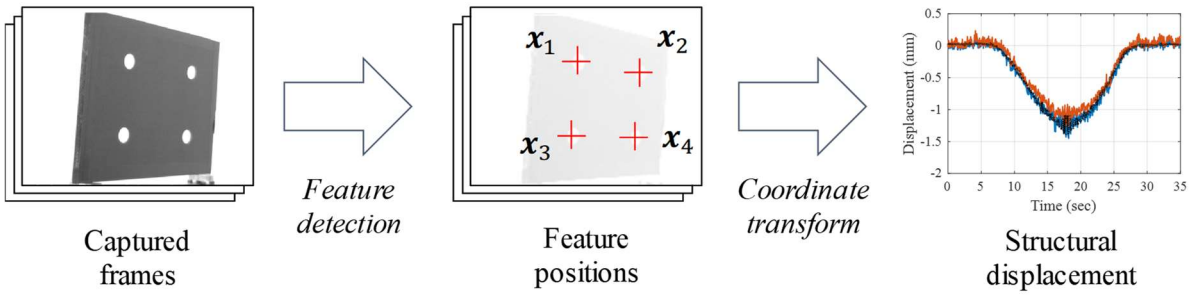

(b) Software procedure

Figure 13. Configuration of vision-based displacement measurement approaches.

Computer vision can be easily employed in displacement measurement of full-scale bridges. Attaching the target to the point at which displacement is required, structural displacement can be observed by placing the camera at a stationary point as shown in Figure 14. If natural pattern is used as the target, special feature tracking algorithms are required such as orientation code matching (OCM) [112, 113], Kanade–Lucas–Tomasi (KLT) [114], Eulerian-based algorithms [115, 116], and upsampled cross correlation (UCC) [117]. Whereas target-based approaches use a target marker with specially designed features, such as a circle [118-123], a checkerboard [124-128], or a random pattern [129]. For the target-based methods, feature detection algorithms are developed to robustly track the specific visual descriptor such as edge detector [130], blob detector [131], and corner detector [132]. After acquiring the position of feature points, displacement is transformed from image to physical domain via a coordinate transform algorithm such as simple scaling [113-119, 121, 124, 128], the affine transform [120, 121], the extrinsic parameters acquisition method [126, 127], and the homography transform [105, 133-137]. Previous research works validated the performance of the vision method in the field condition that sub-mm resolution can be achieved even under harsh field environment. Thus, computer vision is considered to be a practical solution for full-scale displacement measurement applications.

Figure 14. Field application of a computer vision-based method.

2.2. Limitation of the Displacement Measurement Methods in Long-Term Monitoring

Displacement acquisition methods introduced in Section 2.1 have pros and cons in their long-term applications as summarized in Table 7. Indirect method requires assumptions to avoid numerical integration error. Zero-mean process assumption is required if temporal derivative of the displacement is utilized for the indirect method, which makes difficult to detect pseudo-static long-term displacement. A consistent shape function needs to be assumed if spatial derivative of the displacement is employed; thus, long-term variation in structural behavior is hardly reflected. A consistent neutral axis is assumed for the strain-based method. Because structural degradation, such as tendon loss and section loss, shifts location of the neutral axis, strain-based method also has inherent problem in long-term application. As such, time-varying structural condition during long-term operation of the bridge can break assumptions on which indirect method depends. Direct method has potential in long-term application. Consider that the category 1 and 2 sensors are inappropriate for long-term measurement because permanent occupation of the monitoring system under the bridge is difficult in practice. For example, Cao et al. [138] measured the deflections of two pre-stressed concrete beams under sustained loads for 470 days by using dial gauge-type displacement transducers, whereas only the laboratory-scale test was implemented. On the other hand, the sensors in the category 3 and 4 can be adopted for the long-term monitoring applications without intervention of the traffic. Hence, this chapter discusses practical limitations on the category 3 and 4 sensors. Conventional field applications of the long-term displacement by using GNSS, Hydraulic level meter, and total station are reviewed in chapter 2.1.1. Potential limitations of the computer vision and LiDAR-based methods are followed in chapter 2.1.2.

Table 7. Displacement acquisition methods.

Classification		Pros and cons
Indirect method	Temporal derivative data-based method	Error due to invalid assumption
	Spatial derivative data-based method	
	Strain-based method	
Direct method	(Category 1) Contact-type with underpass occupation	Permanent underpass occupation
	(Category 2) Noncontact-type with underpass occupation	
	(Category 3) Contact-type without underpass occupation	Suitable for long-term application
	(Category 4) Noncontact-type without underpass occupation	

2.2.1. Existing field applications of the long-term displacement measurement

Studies on long-term displacement measurement of full-scale bridges have shown that two limitations on the existing method which are insufficient resolution and drift error from sensor movement. GNSS is often adopted for the monitoring of long-span bridges with structural responses larger than 20 mm. Xu et al. deployed GNSS on Tsing Ma bridge in Hong Kong to monitor long-term temperature effect on the suspension bridge, in which 800 mm of seasonal displacement were successfully measured as shown in Figure 15(a) [139]. However, this approach is applicable to the long-span bridges only due to the lack of displacement resolution. Hydraulic meter, a sensor in category 3, can be deployed over the bridge structure to measure displacement. Burdet [98] fabricated hydrostatic displacement meters for long-term monitoring and implemented on the Paudèze and Lutrive viaducts over 35 years as shown in Figure 15(b). Here, the liquid inside the vessel was prone to evaporation that can lead to large displacement measurement error. Total station is the category 4 sensor that displacement can be measured at the side of bridge. Beltempo et al. [140] reported the long-term deflection monitoring of the Colle Isarco viaduct over 30 years by permanently installing a total station at a stationary point as shown in Figure 15(c). Herein, 230 mm of slowly growing displacement was observed that can be either the actual displacement or the drift error from the sensor movement. The existing long-term displacement measurement approaches demonstrate practical implementation on full-scale civil structures; however, handling the sensor movement has not been rigorously considered such that drift-like error could be involved.

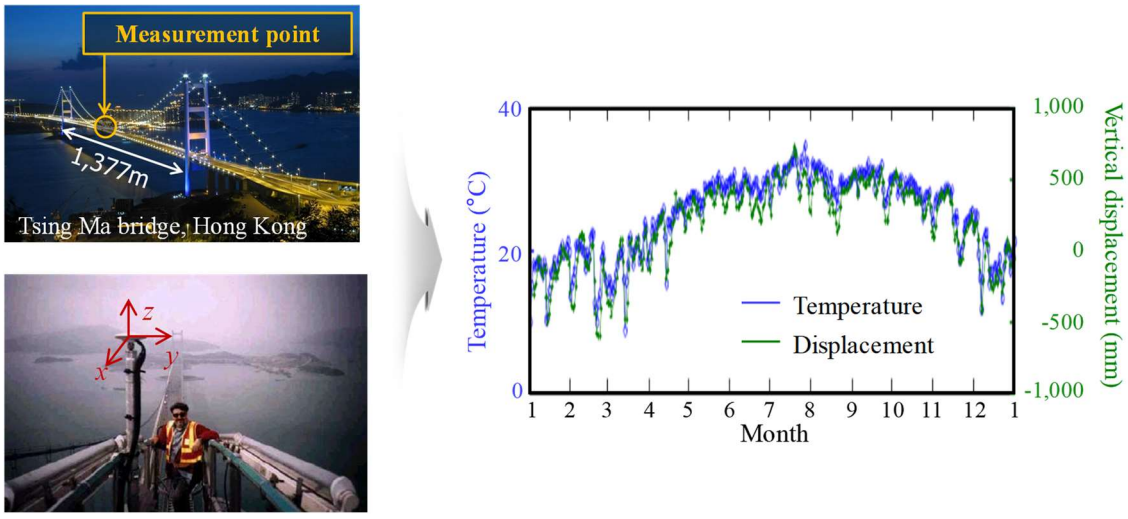

(a) GNSS-based long-term displacement measurement by Xu et al. [139]

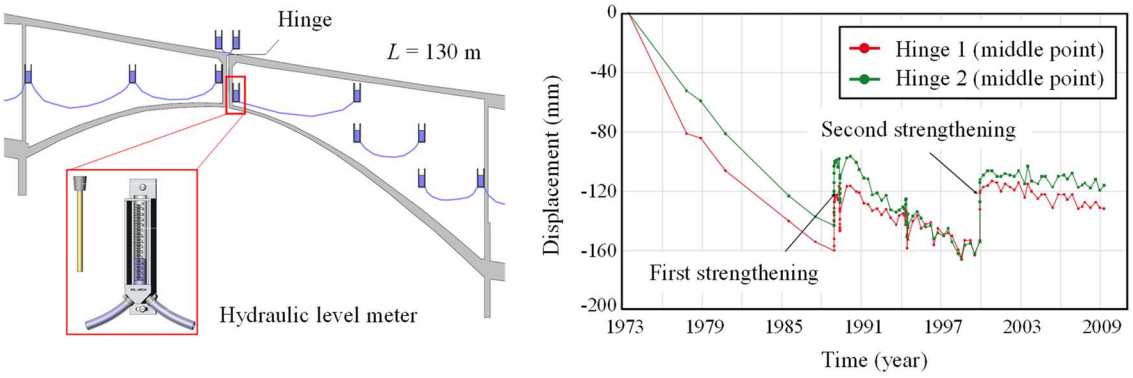

(b) Hydraulic meter-based long-term displacement measurement by Burdet [98]

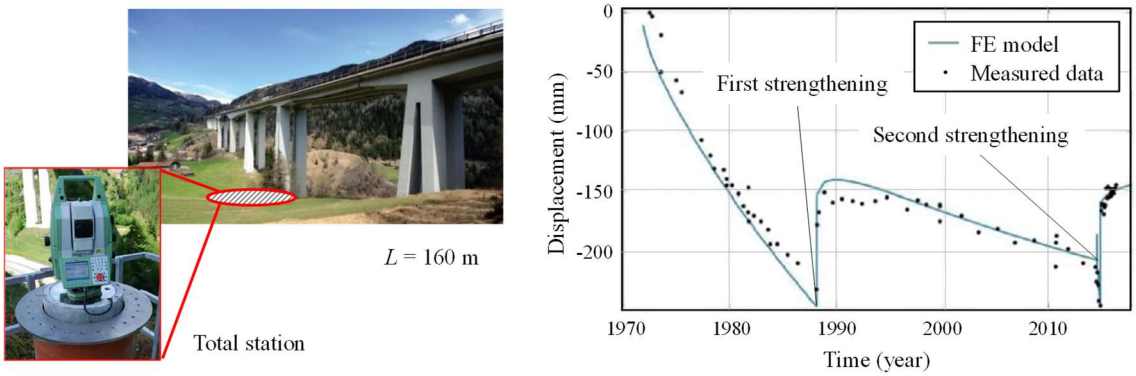

(c) Total station-based long-term displacement measurement by Beltemp et al. [140]

Figure 15. Field applications of the long-term displacement measurement methods.

2.2.2. Limitation of computer vision and LiDAR-based approaches in long-term application

When a camera is installed for long-term monitoring of a full-scale structure, unexpected camera motions are unavoidable. Even if a camera is firmly fixed at a stationary point, its self-weight and temperature fluctuations induce an inevitable and gradual movement of the entire system. In addition, the camera is prone to permanent relocation during long-term operation that can be caused by unexpected collisions. Thus, the complete fixation of the camera is difficult for long-term monitoring applications.

Camera motions can induce considerable false measurements, particularly when computer vision is utilized for monitoring the displacement of full-scale civil structures. Figure 16 shows a camera system where the target is fixed and the camera is displaced in the translational and rotational directions by $-\Delta y$ and $\Delta\theta$, respectively. The resulting false displacements along the vertical direction are Δy and $l \cdot \tan(\Delta\theta)$ for each camera motion. The false displacement from the translational motion become significant when the true target displacement is comparable to Δy. A considerable false displacement can be induced by the rotational motion if the camera is installed at a distance from the target (see Figure 16 (b)). In practice, the minute movement of the civil engineering structures and remotely installed camera for the full-scale applications mean that camera motions can produce significant false displacements that should be properly considered for accurate measurement. For example, 10 mm of false displacement can be induced by $\Delta\theta$ of approximately 1 mrad when the camera is positioned 10 m apart from the target, which can be greater than actual displacement of small- to medium-span bridges.

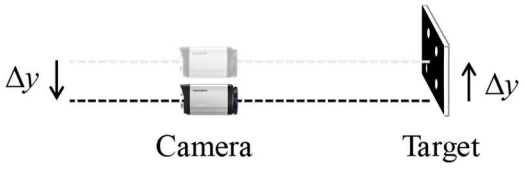

(a) A translational camera motion

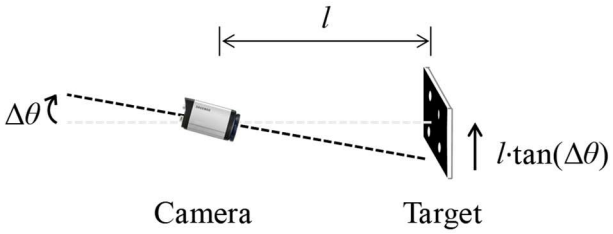

(b) A rotational camera motion

Figure 16. Examples of the camera motions and the resulting false displacements.

The false displacement induced by 6-DOF camera motions is difficult to remove through conventional methods that use a stationary background to compensate for the error [128, 141] or estimate the camera pose [142]. Kim et al. [128] and Chen et al. [141] utilized the background motion to compensate for the motion-induced error. As an example, Figure 17 shows a measurement case where the camera is translated and rotated by $-\Delta y$ and $\Delta\theta$, respectively, which induces the false displacement of $\Delta y + l_1 \cdot \tan(\Delta\theta)$. Here, the background appears to shift by $\Delta y + l_2 \cdot \tan(\Delta\theta)$ when the camera moves, which is subtracted from the original measurement. However, the false displacement cannot be fully removed by subtracting the background motion unless l_1 is close to l_2. Alternatively, Yoon et al. [142] estimated 6-DOF camera motions by using the stationary background to remove the false displacement. The precise measurement of the 6-DOF camera motions was challenging because a remotely installed camera becomes an affine camera [143] for which subtle out-of-plane motions are neglected. In Figure 17, if the camera motion is estimated by the background motion of $\Delta y + l_2 \cdot \tan(\Delta\theta)$ with a large l_2 and small $\Delta\theta$, it will be estimated as a pure translation of $-\Delta y - l_2 \cdot \tan(\Delta\theta)$ because the out-of-plane rotation $\Delta\theta$ is neglected. Conventional methods can compensate for false displacement in the limited situation that l_2 is equal to l_1.

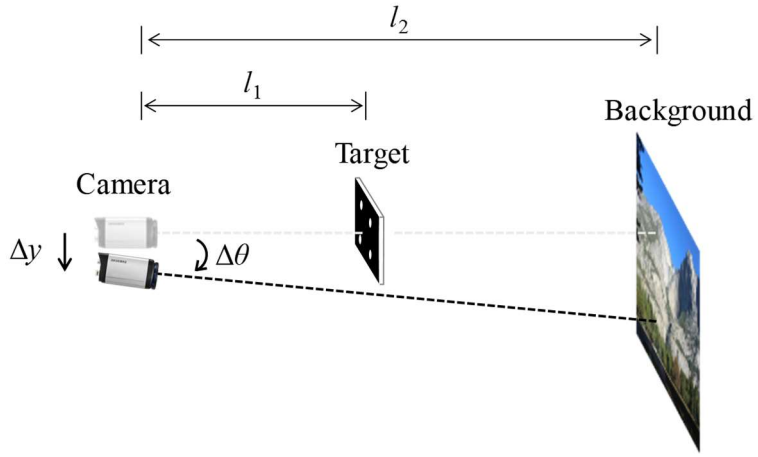

Figure 17. Camera motion error compensation by the background.

Conventional computer vision-based displacement measurement has issues with applicability to the long-term measurement of full-scale civil structures. Regardless of whether a strong fixture is used, a slight camera motion is unavoidable. Thus, the error induced by camera motions should be considered for long-term applications. However, errors are difficult to compensate for by using a stationary background and remotely installed camera. Thus, a better approach of compensating for the false displacement is necessary for the long-term operation of computer vision-based displacement measurement methods.

When a LiDAR system is employed for long-term bridge deflection measurements, the following issues need to be considered. First, the coordinate system of the LiDAR changes over time, which can potentially produce large measurement errors. When the LiDAR is permanently deployed at a fixed location in the field, LiDAR hardware and the supporting structure can be deformed in relation to environmental effects, such as temperature changes, and even a small deformation can result in large errors for distant objects. Practical issues (such as ensuring the security of the expensive LiDAR equipment, and the difficulty in finding available fixed locations for LiDAR installations) also prevent permanent deployment. In the case of temporary installation, i.e. the LiDAR is brought to the field whenever deflection measurements are required, a new coordinate system is produced whenever the equipment is repositioned; it is thus not possible to directly obtain the current displacement relative to the previous measurement. Second, the target objects need to be highly reflective to enable high-precision measurements, and a preferred target object needs to be made of highly reflective materials and placed perpendicular to the emitted light for maximum reflectance. As common construction materials (such as concrete and steel) are not highly reflective, the accuracy of the LiDAR system is degraded [103]. Furthermore, the LiDAR needs to be placed close to the target bridge to obtain a high spatial resolution [144]. As the laser from the LiDAR is emitted radially at certain spatial intervals, the measurement resolution depends on the distance between the LiDAR and the target bridge. In this respect, a small spatial interval, which is required to obtain a high measurement resolution, results in a dramatic increase in the time required to conduct measurements and perform computations [103, 104]. Therefore, to obtain a feasible LiDAR system for measuring long-term bridge displacement, following issues need to be properly addressed.

- Permanent sensor installation without any motion
- Entire bridge scanning (long scanning time)
- Coarse scanning to save time (low displacement resolution)
- Manual processing of the 3D point cloud

2.3. Summary and Discussion

This section introduces conventional displacement measurement systems. Indirect estimation method converts other physical quantities such as acceleration and strain to displacement. Due to the assumptions involved in the indirect methods, direct measurement method is considered for long-term displacement measurement. Direct measurement method employs a displacement sensor. Depending on the difficulty in preparing the reference point, the direct method is categorized into four groups. The fourth category, which is noncontact-type without need for underpass occupation, is considered to be the most practical approaches for full-scale applications. Limited research endeavored to develop a long-term displacement measurement method by using GNSS, hydraulic level meter, and total station, computer vision and LiDAR. Such methods, however, have practical issues regarding not enough precision and drift error due to the sensor movement which needs to be revolved for long-term monitoring of full-scale bridges.

3. Vision-Based Long-Term Displacement Measurement System

3.1. Introduction of dual-camera system

The identified limitation in vision-based displacement measurement method for long-term application is camera motion. As discussed in Section 2.1.2, single camera cannot be used to compensate the camera motion-induced error because of ambiguity between self-motion and structural displacement. Other than single camera-based system needs to be employed for long-term displacement measurement.

The hardware configuration of the dual-camera system consists of two targets and two cameras that are tightly attached to each other, as shown in Figure 18. When the main target is deployed at a measurement point on a structure, the main camera records the movements of the target. The recorded video is generally used to calculate the structural displacement; however, the measured displacement can include an error from the camera motion. The sub-camera measures its 6-DOF motion relative to the sub-target, which is placed at a stationary reference point (e.g., bridge pier). Because the two cameras are fixed to each other, the false displacement can be compensated by the identified motions of the sub-camera.

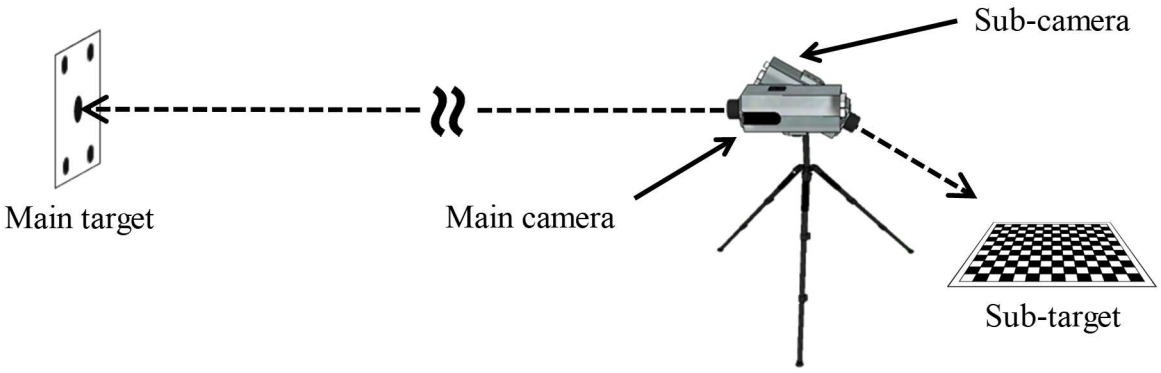

Figure 18. Hardware configuration of the dual-camera system.

3.2. Long-Term Displacement Measurement based on Dual-Camera System

3.2.1. Basic camera geometry involved in the proposed method

The dual-camera system has three different types of coordinate systems, as shown in Figure 19: world, camera, and image. The world coordinate system is introduced to express the position of either the main or sub-target. Once an arbitrary point is selected on the target as the origin of the world coordinate system, two basis vectors are defined by two orthogonal unit vectors within the target plane, which can be specified by user-defined patterns on the target. The cross-product of the two basis vectors yields the third basis vector, which is used to complete building the three-dimensional world coordinate system. The world coordinate system remains at the initial position even when the target plane moves. The camera coordinate system is provided by the camera. The optical axis of the camera is assigned as the *z*-axis, and unit vectors orthogonal to the *z*-axis are defined as *x*- and *y*-axes. The camera coordinate system varies as the camera moves in space, in contrast to the world coordinate system. The image coordinate system is two-dimensional and is used for captured images. The image coordinates are in units of pixels, and the origin is at the upper left of an image. The three coordinate systems can fully represent the physical and image spaces associated with a camera.

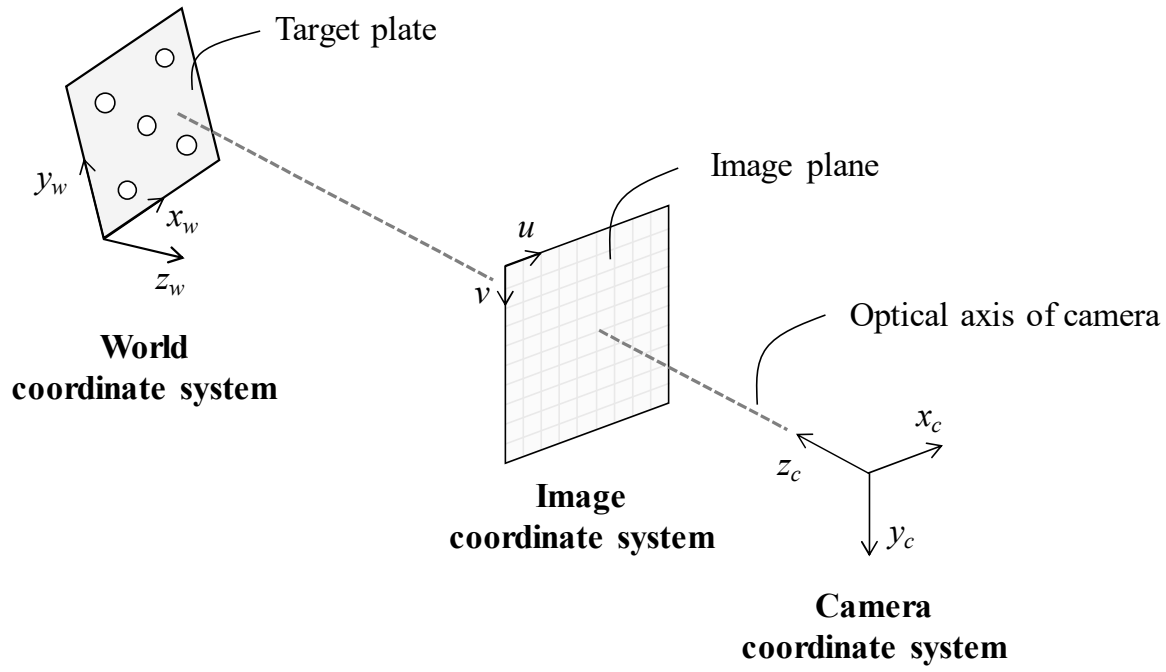

Figure 19. Basic camera geometry.

The dual-camera system has six coordinate systems in total as listed in Table 8 because the main and sub-cameras each have their own world, image, and camera coordinates, as shown in Figure 20. Herein, the prefixes *W*, *C*, and *I* represent the world, camera, and image coordinate systems, respectively, while the suffixes *M* and *S* denote the main and sub-camera systems respectively. *WM* and *WS* are the world coordinate systems defined by the initial positions of the main and sub-targets, respectively. *CM* and *CS* are the camera coordinate systems respectively defined by the positions of the main and sub-cameras. *IM* and *IS* are the image coordinate systems of the main and sub-cameras, respectively.

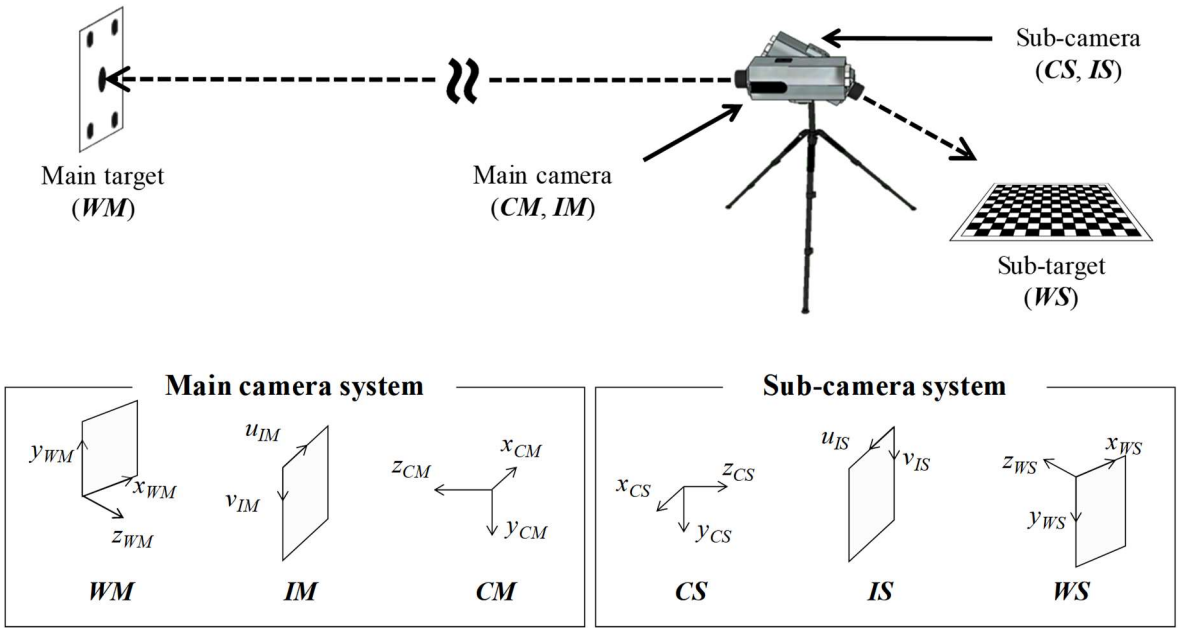

Figure 20. Illustration of the coordinate systems in the dual-camera system.

Table 8. Coordinate systems in the dual-camera system.

Notation	Coordinate system type	Reference object
WM	World coordinate system	Initial position of the main target
WS	World coordinate system	Initial position of the sub-target
CM	Camera coordinate system	Position of the main camera
CS	Camera coordinate system	Position of the sub-camera
IM	Image coordinate system	Image captured by the main camera
IS	Image coordinate system	Image captured by the sub-camera

Two different time indices, j and k, are introduced to distinguish between the structural displacement (main target motion) and the camera motion. Time index for the structural displacement is denoted by j. Given that the main target contains N number of feature point, the position of the i-th feature point in the main target at j-th time sequence can be expressed in terms of WM, WS, CM, CS, IM, and IS as:

$$\begin{Bmatrix} x_i(j) \\ y_i(j) \\ z_i(j) \end{Bmatrix}_{WM}, \begin{Bmatrix} x_i(j) \\ y_i(j) \\ z_i(j) \end{Bmatrix}_{WS}, \begin{Bmatrix} x_i(j) \\ y_i(j) \\ z_i(j) \end{Bmatrix}_{CM}, \begin{Bmatrix} x_i(j) \\ y_i(j) \\ z_i(j) \end{Bmatrix}_{CS}, \begin{Bmatrix} u_i(j) \\ v_i(j) \end{Bmatrix}_{IM}, \text{ and } \begin{Bmatrix} u_i(j) \\ v_i(j) \end{Bmatrix}_{IS}. \tag{3.1}$$

Index k is employed to denote camera position at k-th time sequence, by which coordinate systems are expressed as $CM(k)$, $CS(k)$, $IM(k)$, and $IS(k)$ at time k. The notation WM and WS will be used as it is instead of $WM(k)$ and $WS(k)$ because the world coordinate systems are defined in terms of initial position of the targets. Using the time indices j and k, position of the i-th feature point in the main target at j-th time sequence can be expressed in terms of WM, WS, $CM(k)$, $CS(k)$, $IM(k)$, and $IS(k)$ as:

$$\begin{Bmatrix} x_i(j) \\ y_i(j) \\ z_i(j) \end{Bmatrix}_{WM}, \begin{Bmatrix} x_i(j) \\ y_i(j) \\ z_i(j) \end{Bmatrix}_{WS}, \begin{Bmatrix} x_i(j) \\ y_i(j) \\ z_i(j) \end{Bmatrix}_{CM(k)}, \begin{Bmatrix} x_i(j) \\ y_i(j) \\ z_i(j) \end{Bmatrix}_{CS(k)}, \begin{Bmatrix} u_i(j) \\ v_i(j) \end{Bmatrix}_{IM(k)}, \text{ and } \begin{Bmatrix} u_i(j) \\ v_i(j) \end{Bmatrix}_{IS(k)}. \tag{3.2}$$

Indeed, position of a feature point at time j can be captured by the camera at time k only if $j = k$. However, this study involves any combination of j and k to express position of the main target in terms of constant camera position. For example, consider a main camera and a main target at time t that is deviated from their original position. The position of the captured feature point is

$$\begin{Bmatrix} u_i(j=t) \\ v_i(j=t) \end{Bmatrix}_{IM(k=t)} \tag{3.3}$$

which implies position of the main target but simultaneously disturbed by the camera movement. The position of the same point in terms of initial camera position can be expressed as:

$$\begin{Bmatrix} u_i(j=t) \\ v_i(j=t) \end{Bmatrix}_{IM(k=1)} \tag{3.4}$$

where index 1 is used to indicate the initial measurement time. As can be seen in this example, two different time indices effectively denote position of the main target in arbitrary camera position.

The notation $\mathbf{B}_{\Omega(q)\to\Psi(r)}$ is introduced to express coordinate transforms from $\Omega(q)$ to $\Psi(r)$, which are two coordinate systems selected from *WM*, *WS*, *CM*, *CS*, *IM*, and *IS*. For example, $\mathbf{B}_{CS(1)\to IM(2)}$ is the coordinate transform from *CS*(1) to *IM*(2). If the inverse transform is allowed, $\mathbf{B}^{-1}{}_{\Omega(q)\to\Psi(r)}$ is the same expression for the $\mathbf{B}_{\Psi(r)\to\Omega(q)}$ switching the basis coordinate systems. To include translation, rotation, shearing, scaling, and perspective transforms in $\mathbf{B}_{\Omega(q)\to\Psi(r)}$, a homogeneous coordinate representation is adopted where an additional 1 is attached to the end of the coordinate vector. Hence, the coordinate transform $\mathbf{B}_{\Omega(q)\to\Psi(r)}$ is either a 4 × 4, 3 × 4, or 3 × 3 matrix depending on the source and destination coordinates to be transformed.

Three types of coordinate transformation matrices are involved in the dual-camera system. $\mathbf{B}_{\Omega(q)\to\Psi(r)}$ becomes a 4 × 4 nonreflective similarity transformation matrix when both Ω and Ψ are the spatial coordinate systems such as *WM*, *WS*, *CM*, and *CS*. $\mathbf{B}_{\Omega(q)\to\Psi(r)}$ becomes a 3 × 4 projective transformation matrix when transforms from a spatial coordinate system Ω to an image coordinate system Ψ (one of *IM* and *IS*). $\mathbf{B}_{\Omega(q)\to\Psi(r)}$ becomes a 3 × 3 homography transform matrix when both Ω and Ψ are the planar coordinate system in which the planar coordinate systems can be either an image coordinate system or a two-dimensional spatial coordinate system (projection of three-dimensional spatial coordinate systems. These transformation matrices will be used to change the basis coordinate systems.

Dual-camera system involves time-invariant coordinate transforms although coordinate systems to be transformed move over time. The intrinsic camera parameters, $\mathbf{B}_{CM(k)\to IM(k)}$ and $\mathbf{B}_{CS(k)\to IS(k)}$, are time-invariant because focal length, principal points, and skewness are constant values defined by the camera specification. $\mathbf{B}_{CM(k)\to CS(k)}$ and $\mathbf{B}_{CS(k)\to CM(k)}$ are constant in disregard of the time index *j* because relative position between the main and sub-cameras are assumed to be fixed over time. $\mathbf{B}_{CM(k)\to IS(k)}$ and $\mathbf{B}_{CS(k)\to IM(k)}$ become time-invariant matrices due to the following equalities:

$$\mathbf{B}_{CM(k)\to IS(k)} = \mathbf{B}_{CS(k)\to IS(k)}\mathbf{B}_{CM(k)\to CS(k)} \tag{3.5}$$

$$\mathbf{B}_{CS(k)\to IM(k)} = \mathbf{B}_{CM(k)\to IM(k)}\mathbf{B}_{CS(k)\to CM(k)} \tag{3.6}$$

These time-invariant properties in the dual-camera system will be employed in Section 3.2.2–3.2.4 to derive long-term displacement measurement by compensating for the camera motion-induced error.

3.2.2. Formulation for true displacement

The proposed displacement calculation algorithm determines the true structural displacement by compensating for the false displacement caused by the camera motion. Let $\{x_i(j) \quad y_i(j) \quad z_i(j) \quad 1\}^T_{WM}$ be the position of the i-th feature point at the k-th frame in WM. The image coordinate of the feature point at the j-th frame in $IM(k)$, which is denoted by $\{u_i(j) \quad v_i(j) \quad 1\}^T_{IM(k)}$, can be expressed by using the coordinate transform of $\{x_i(j) \quad y_i(j) \quad z_i(j) \quad 1\}^T_{WM}$ as follows:

$$\begin{Bmatrix} u_i(j) \\ v_i(j) \\ 1 \end{Bmatrix}_{IM(k)} = \mathbf{B}_{WM \to IM(k)} \begin{Bmatrix} x_i(j) \\ y_i(j) \\ 0 \\ 1 \end{Bmatrix}_{WM} \quad (i = 1,2,\cdots,N) \tag{3.7}$$

where $\mathbf{B}_{WM \to IM(k)}$ is a projective transform from WM to $IM(k)$. Note that $z_i(j) = 0$ because the origin of WM is on the main target, which is assumed to undergo in-plane motions only. Even though the different frame indices j and k appear in $\{u_i(j) \quad v_i(j) \quad 1\}^T_{IM(k)}$, the image coordinate can only be obtained when $j = k$, which is the actual measurement of the main camera. On the other hand, image coordinates with different j and k can be used to represent the false displacement induced by the camera motion. The false displacement is viewed as the initial coordinates of a feature point in the k-th image coordinate system $IM(k)$, which reflects the camera motion. Thus, the false displacement $\{u_i(1) \quad v_i(1) \quad 1\}^T_{IM(k)}$ can be formulated by using Eq. (3.7) with $j = 1$:

$$\begin{Bmatrix} u_i(1) \\ v_i(1) \\ 1 \end{Bmatrix}_{IM(k)} = \mathbf{B}_{WM \to IM(k)} \begin{Bmatrix} x_i(1) \\ y_i(1) \\ 0 \\ 1 \end{Bmatrix}_{WM} . \tag{3.8}$$

The true displacement can be obtained by compensating for the false displacement in Eq. (3.8) from the current measurement at the k-th frame from the main camera (i.e., $\{u_i(k) \quad v_i(k) \quad 1\}^T_{IM(k)}$). Subtracting Eq. (3.8) from Eq. (3.7) with $k = j$ leads to

$$\begin{Bmatrix} u_i(k) - u_i(1) \\ v_i(k) - v_i(1) \\ 0 \end{Bmatrix}_{IM(k)} = \mathbf{B}_{WM \to IM(k)} \begin{Bmatrix} x_i(k) - x_i(1) \\ y_i(k) - y_i(1) \\ 0 \\ 0 \end{Bmatrix}_{WM} \tag{3.9}$$

where $\{u_i(k) - u_i(1) \quad v_i(k) - v_i(1) \quad 0\}^T_{IM(k)}$ and $\{x_i(k) - x_i(1) \quad y_i(k) - y_i(1) \quad 0 \quad 0\}^T_{WM}$ are the true displacement expressed in $IM(k)$ and WM, respectively. Note that the desired displacement is the change

in positions relative to the initial frame. Eq. (3.9) can be simplified by considering the first two rows only:

$$\begin{Bmatrix} u_i(k)-u_i(1) \\ v_i(k)-v_i(1) \end{Bmatrix}_{IM(k)} = \tilde{\mathbf{B}}_{WM\rightarrow IM(k)} \begin{Bmatrix} x_i(k)-x_i(1) \\ y_i(k)-y_i(1) \end{Bmatrix}_{WM} \tag{3.10}$$

where $\tilde{\mathbf{B}}_{WM\rightarrow IM(k)}$ is the 2 × 2 submatrix of $\mathbf{B}_{WM\rightarrow IM(k)}$ obtained by deleting the third and fourth columns and the third row. Knowing that $\{u_i(k) \quad v_i(k)\}^{\mathrm{T}}_{IM(k)}$ can be directly obtained from the main camera, $\tilde{\mathbf{B}}_{WM\rightarrow IM(k)}$ and $\{u_i(1) \quad v_i(1)\}^{\mathrm{T}}_{IM(k)}$ need to be determined to calculate the true displacement expressed in WM (i.e., $\{x_i(k) - x_i(1) \quad y_i(k) - y_i(1)\}^{\mathrm{T}}_{WM}$).

The rest of this subsection describes the details of the proposed displacement calculation algorithm. Section 3.2.3 describes how to calculate $\tilde{\mathbf{B}}_{WM\rightarrow IM(k)}$ for the initial frame, Section 3.2.4 describes how to compute $\{u_i(1) \quad v_i(1)\}^{\mathrm{T}}_{IM(k)}$ with the 6-DOF sub-camera motion, and Section 3.2.5 summarizes the formulation for the true displacement by combining the main and sub-camera systems.

3.2.3. Formulation of frame-invariance transform matrix with main camera

The main camera can be assumed to be an affine camera; this generally holds when the image coordinates with and without the affine camera assumption are effectively the same [143]. Let x be the image coordinate and x_{affine} be the image coordinate with the affine camera assumption. When the difference between x and x_{affine} is less than the minimum achievable pixel resolution (e.g., 1 pixel without a subpixel algorithm), an affine camera can be assumed. The difference is formulated based on the camera geometry [143]:

$$\left\| x - x_{affine} \right\|_2 = \left\| \frac{\Delta z}{d_0}(x - x_0) \right\|_2 \tag{3.11}$$

where $\| \|_2$ denotes the 2-norm, Δz is the depth motion (i.e., translational motion parallel to the optical axis), d_0 is the initial distance between the target and focal point, and x_0 is the camera's principal point which is generally near the center of the image. $\|x - x_{affine}\|_2$ can be less than 1 pixel when both $\Delta z/d_0$ and $x - x_0$ are small. Hence, for the affine camera assumption to hold, the depth motion Δz should be small compared to the initial target distance d_0, and the image coordinate of the feature should be near the center of the image. Knowing that displacement of the full-scale bridges along the longitudinal direction is significantly less than their span length, it is reasonable to assume that $\Delta z/d_0$ is nearly zero [145]. The main camera has a negligible $\|x - x_{affine}\|_2$ and thus can be considered to be an affine camera.

$\widetilde{\mathbf{B}}_{WM\rightarrow IM(k)}$ can be obtained with the main camera under the affine camera assumption. If the main camera is affine, the third row of the transform matrix $\mathbf{B}_{WM\rightarrow IM(k)}$ in Eq. (3.9) is constrained to [0 0 0 1]. Furthermore, if a small camera rotation is assumed, the first three columns related to rotation [143] are independent of the image frame. Thus, $\mathbf{B}_{WM\rightarrow IM(k)}$ can be expressed as

$$\mathbf{B}_{WM\rightarrow IM(k)} = \begin{bmatrix} b_{11} & b_{12} & b_{13} & b_{14}(k) \\ b_{21} & b_{22} & b_{23} & b_{24}(k) \\ 0 & 0 & 0 & 1 \end{bmatrix}_{WM\rightarrow IM(k)} \tag{3.12}$$

where b_{qr} is an entry in the first and second rows of $\mathbf{B}_{WM\rightarrow IM(k)}$ (q = 1, 2; r = 1, ⋯, 4). Because the third column in $\mathbf{B}_{WM\rightarrow IM(k)}$ has no contribution due to the 0 in $\{x_i(k) \quad y_i(k) \quad 0 \quad 1\}^{\mathrm{T}}_{WM}$, Eq. (3.7) can be rewritten in a simplified form:

$$\begin{Bmatrix} u_i(j) \\ v_i(j) \\ 1 \end{Bmatrix}_{IM(k)} = \begin{bmatrix} b_{11} & b_{12} & b_{14}(k) \\ b_{21} & b_{22} & b_{24}(k) \\ 0 & 0 & 1 \end{bmatrix}_{WM\rightarrow IM(k)} \begin{Bmatrix} x_i(j) \\ y_i(j) \\ 1 \end{Bmatrix}_{WM} . \tag{3.13}$$

The positions of all feature points in the main target can be used to arrange Eq. (3.13) as

$$\begin{Bmatrix} b_{11} \\ b_{12} \\ b_{14}(k) \\ b_{21} \\ b_{22} \\ b_{24}(k) \end{Bmatrix} = \begin{bmatrix} x_1(j) & y_1(j) & 1 & 0 & 0 & 0 \\ 0 & 0 & 0 & x_1(j) & y_1(j) & 1 \\ & \vdots & & & \vdots & \\ x_N(j) & y_N(j) & 1 & 0 & 0 & 0 \\ 0 & 0 & 0 & x_N(j) & y_N(j) & 1 \end{bmatrix}_{WM}^{+} \begin{Bmatrix} u_1(j) \\ v_1(j) \\ \vdots \\ u_N(j) \\ v_N(j) \end{Bmatrix}_{IM(k)} \tag{3.14}$$

where + denotes the Penrose–Moore pseudo inverse [146]. Because the initial positions of the features in *WM* are prior information, the pseudo inversed matrix in Eq. (3.14) can be built with the known initial coordinates $\{x_i(1) \quad y_i(1) \quad 1\}^T_{WM}$. In addition, $\{u_i(1) \quad v_i(1) \quad 1\}^T_{IM(1)}$ can be obtained as a measurement from the main camera in the initial frame, as discussed in Section 4.2.1. The known coordinates of the feature points at the initial frame (i.e., $\{x_i(1) \quad y_i(1) \quad 1\}^T_{WM}$ and $\{u_i(1) \quad v_i(1) \quad 1\}^T_{IM(1)}$) can be used to determine the transform matrix in Eq. (3.13) with $j = 1$, which also includes $\widetilde{\mathbf{B}}_{WM \to IM(j)}$ in Eq. (3.10). The main target needs to have at least three features to solve for the six unknown parameters (i.e., b_{11}, b_{12}, b_{21}, b_{22}, $b_{14}(1)$, and $b_{24}(1)$) in the transform matrix.

3.2.4. Formulation of camera motion-induced error with sub-camera

The sub-camera measures its 6-DOF camera motions with respect to the initial position $\mathbf{B}_{CS(1)\to CS(k)}$ by using the planar target-based calibration method proposed by Zhang [147]. Consider that the sub-camera is placed close to the fixed sub-target having M feature points. Contrary to the main camera that is assumed to be an affine camera, the sub-camera is assumed to conform the perspective camera model enabling sensitive measurement of 6-DOF motion. The position of the i-th feature point in $IS(k)$ (i.e., $\{\bar{u}_i \quad \bar{v}_i \quad 1\}^{\mathrm{T}}_{IS(k)}$) and in WS (i.e., $\{\bar{x}_i \quad \bar{y}_i \quad 0 \quad 1\}^{\mathrm{T}}_{WS}$) can be expressed as follows with the notation defined in Section 4.1:

$$\begin{Bmatrix} \bar{u}_i \\ \bar{v}_i \\ \bar{w}_i \end{Bmatrix}_{IS(k)} = \mathbf{B}_{CS(k)\to IS(k)}\mathbf{B}_{WS\to CS(k)} \begin{Bmatrix} \bar{x}_i \\ \bar{y}_i \\ 0 \\ 1 \end{Bmatrix}_{WS} \qquad (i = 1,2,\cdots,M) \tag{3.15}$$

where $\mathbf{B}_{CS(k)\to IS(k)}$ is a projective transform from $CS(k)$ to $IS(k)$ and $\mathbf{B}_{WS\to CS(k)}$ is a similarity transform from WS to $CS(k)$. $\mathbf{B}_{CS(k)\to IS(k)}$ consists of intrinsic camera parameters:

$$\mathbf{B}_{CS(k)\to IS(k)} = \begin{bmatrix} \alpha & \gamma & \mu & 0 \\ 0 & \beta & \nu & 0 \\ 0 & 0 & 1 & 0 \end{bmatrix}_{CS(k)\to IS(k)} . \tag{3.16}$$

$\mathbf{B}_{WS\to CS(k)}$ has the extrinsic camera parameters of the rotation matrix $\mathbf{R}_{3\times3}(k)$ and translation vector $\mathbf{T}_{3\times1}(k)$:

$$\mathbf{B}_{WS\to CS(k)} = \begin{bmatrix} \mathbf{R}_{3\times3}(k) & \mathbf{T}_{3\times1}(k) \\ \mathbf{0}_{1\times3} & 1 \end{bmatrix}_{WS\to CS(k)} . \tag{3.17}$$

Eqs. (3.16) and (3.17) can be computed from the image of the sub-target with the calibration method. Once $\mathbf{B}_{WS\to CS(k)}$ is obtained for every frame, the 6-DOF sub-camera motion with respect to its initial position is computed as follows:

$$\mathbf{B}_{CS(1)\to CS(k)} = \mathbf{B}_{WS\to CS(k)}\mathbf{B}^{-1}_{WS\to CS(1)} . \tag{3.18}$$

Thus, the 6-DOF motion of the sub-camera with respect to the initial position expressed as $\mathbf{B}_{CS(1)\to CS(k)}$ can be determined in every measurement frame.

The 6-DOF sub-camera motion $\mathbf{B}_{CS(1)\to CS(k)}$ is employed to formulate the false displacement. First, Eq. (3.7) is expanded with $\mathbf{B}_{CS(1)\to CS(j)}$ as follows:

$$\begin{aligned}\begin{Bmatrix} u_i(j) \\ v_i(j) \\ 1 \end{Bmatrix}_{IM(k)} &= \mathbf{B}_{CS(k)\to IM(k)}\mathbf{B}_{CS(1)\to CS(k)}\mathbf{B}_{WM\to CS(1)}\begin{Bmatrix} x_i(j) \\ y_i(j) \\ 0 \\ 1 \end{Bmatrix}_{WM} \\ &= \mathbf{B}_{CS(k)\to IM(k)}\mathbf{B}_{CS(1)\to CS(k)}\begin{Bmatrix} x_i(j) \\ y_i(j) \\ z_i(j) \\ 1 \end{Bmatrix}_{CS(1)} .\end{aligned} \tag{3.19}$$

Note that the z-coordinate is generally nonzero in $CS(1)$. $\mathbf{B}_{CS(1)\to CS(k)}$ is a rigid transformation that can be expressed as the rotation $\overline{\mathbf{R}}_{3\times3}(k)$ and translation $\overline{\mathbf{T}}_{3\times1}(k)$. Thus, Eq. (3.19) can be further expanded as follows:

$$\begin{Bmatrix} u_i(j) \\ v_i(j) \\ 1 \end{Bmatrix}_{IM(k)} = \begin{bmatrix} \bar{b}_{11} & \bar{b}_{12} & \bar{b}_{13} & \bar{b}_{14} \\ \bar{b}_{21} & \bar{b}_{22} & \bar{b}_{23} & \bar{b}_{24} \\ 0 & 0 & 0 & 1 \end{bmatrix}_{CS(k)\to IM(k)} \begin{bmatrix} \overline{\mathbf{R}}_{3\times3}(k) & \overline{\mathbf{T}}_{3\times1}(k) \\ \mathbf{0}_{1\times3} & 1 \end{bmatrix}_{CS(1)\to CS(k)} \begin{Bmatrix} x_i(j) \\ y_i(j) \\ z_i(j) \\ 1 \end{Bmatrix}_{CS(1)} . \tag{3.20}$$

As discussed for Eq.(3.8), the false displacement at the k-th frame is the initial position of the main target represented in $IM(k)$, which is Eq. (3.20) with $j = 1$:

$$\begin{Bmatrix} u_i(1) \\ v_i(1) \\ 1 \end{Bmatrix}_{IM(k)} = \begin{bmatrix} \bar{b}_{11} & \bar{b}_{12} & \bar{b}_{13} & \bar{b}_{14} \\ \bar{b}_{21} & \bar{b}_{22} & \bar{b}_{23} & \bar{b}_{24} \\ 0 & 0 & 0 & 1 \end{bmatrix}_{CS(k)\to IM(k)} \begin{bmatrix} \overline{\mathbf{R}}_{3\times3}(k) & \overline{\mathbf{T}}_{3\times1}(k) \\ \mathbf{0}_{1\times3} & 1 \end{bmatrix}_{CS(1)\to CS(k)} \begin{Bmatrix} x_i(1) \\ y_i(1) \\ z_i(1) \\ 1 \end{Bmatrix}_{CS(1)} . \tag{3.21}$$

The unknown constants $\bar{b}_{11}$, $\bar{b}_{12}$, $\bar{b}_{13}$, $\bar{b}_{14}$, $\bar{b}_{21}$, $\bar{b}_{22}$, $\bar{b}_{23}$, $\bar{b}_{24}$, and $\{x_i(1) \quad y_i(1) \quad z_i(1)\}^{\mathrm{T}}_{CS(1)}$ need to be determined to calculate the false displacement at the k-th frame $\{u_i(1) \quad v_i(1) \quad 1\}^{\mathrm{T}}_{IM(k)}$.

The dual-camera system requires another initial calibration process to find the unknown constants in Eq. (3.21) before the actual measurement. The calibration process comprises artificially moving the cameras H times assuming that both targets do not move from their original positions. Thus, $\{x_i(j) \quad y_i(j) \quad z_i(j) \quad 1\}^{\mathrm{T}}_{CS(k)}$ is the same as $\{x_i(1) \quad y_i(1) \quad z_i(1)\}^{\mathrm{T}}_{CS(k)}$ during the calibration process. The false displacement with respect to the initial frame can be obtained as the difference between the positions

$\{u_i(1) \quad v_i(1) \quad 1\}^{\mathrm{T}}_{IM(k)}$ and $\{u_i(1) \quad v_i(1) \quad 1\}^{\mathrm{T}}_{IM(1)}$:

$$\begin{aligned}&\begin{Bmatrix} u_i(1) \\ v_i(1) \end{Bmatrix}_{IM(k)} - \begin{Bmatrix} u_i(1) \\ v_i(1) \end{Bmatrix}_{IM(1)} \\ &= \begin{bmatrix} \bar{b}_{11} & \bar{b}_{12} & \bar{b}_{13} & \bar{b}_{14} \\ \bar{b}_{21} & \bar{b}_{22} & \bar{b}_{23} & \bar{b}_{24} \end{bmatrix}_{CS(k)\rightarrow IM(k)} \left(\begin{bmatrix} \bar{\mathbf{R}}_{3\times3}(k) & \bar{\mathbf{T}}_{3\times1}(k) \\ \mathbf{0}_{1\times3} & 1 \end{bmatrix}_{CS(1)\rightarrow CS(k)} - \begin{bmatrix} \bar{\mathbf{R}}_{3\times3}(1) & \bar{\mathbf{T}}_{3\times1}(1) \\ \mathbf{0}_{1\times3} & 1 \end{bmatrix}_{CS(1)\rightarrow CS(1)} \right) \begin{Bmatrix} x_i(1) \\ y_i(1) \\ z_i(1) \\ 1 \end{Bmatrix}_{CS(1)} .\end{aligned} \tag{3.22}$$

Because the transform from $CS(1)$ to $CS(1)$ exhibits an identity matrix (i.e., $\bar{\mathbf{R}}_{3\times3}(1)$ is an identity matrix and $\bar{\mathbf{T}}_{3\times1}(1)$ is a zero vector), Eq. (3.22) can be simplified as:

$$\begin{Bmatrix} u_i(1) \\ v_i(1) \end{Bmatrix}_{IM(k)} - \begin{Bmatrix} u_i(1) \\ v_i(1) \end{Bmatrix}_{IM(1)} = \begin{bmatrix} \bar{b}_{11} & \bar{b}_{12} & \bar{b}_{13} \\ \bar{b}_{21} & \bar{b}_{22} & \bar{b}_{23} \end{bmatrix}_{CS(k)\rightarrow IM(k)} \begin{bmatrix} \bar{\mathbf{R}}_{3\times3}(k) - \mathbf{I}_{3\times3} & \bar{\mathbf{T}}_{3\times1}(k) \end{bmatrix} \begin{Bmatrix} x_i(1) \\ y_i(1) \\ z_i(1) \\ 1 \end{Bmatrix}_{CS(1)} \tag{3.23}$$

The nine unknown parameters $\bar{b}_{11}$, $\bar{b}_{12}$, $\bar{b}_{13}$, $\bar{b}_{21}$, $\bar{b}_{22}$, $\bar{b}_{23}$, and $\{x_i(1) \quad y_i(1) \quad z_i(1)\}^{\mathrm{T}}_{CS(1)}$ are determined by solving the minimization problem in Eq. (3.24).

$$\begin{aligned}&\underset{\substack{\bar{b}_{11},\bar{b}_{12},\bar{b}_{13} \\ \bar{b}_{21},\bar{b}_{22},\bar{b}_{23} \\ \{x_i(1) \quad y_i(1) \quad z_i(1)\}^{\mathrm{T}}_{CS(1)}}}{\arg\min} \quad F\left(\begin{Bmatrix} u_i(1) \\ v_i(1) \end{Bmatrix}_{IM(k)}, \begin{Bmatrix} u_i(1) \\ v_i(1) \end{Bmatrix}_{IM(1)}, \bar{\mathbf{R}}_{3\times3}(k), \bar{\mathbf{T}}_{3\times1}(k) \right) \\ &F(\square) = \sum_{k=1,\cdots,H} \left\| \begin{Bmatrix} u_i(1) \\ v_i(1) \end{Bmatrix}_{IM(k)} - \begin{Bmatrix} u_i(1) \\ v_i(1) \end{Bmatrix}_{IM(1)} - \begin{bmatrix} \bar{b}_{11} & \bar{b}_{12} & \bar{b}_{13} \\ \bar{b}_{21} & \bar{b}_{22} & \bar{b}_{23} \end{bmatrix}_{CS(k)\rightarrow IM(k)} \begin{bmatrix} \bar{\mathbf{R}}_{3\times3}(k) - \mathbf{I}_{3\times3} & \bar{\mathbf{T}}_{3\times1}(k) \end{bmatrix} \begin{Bmatrix} x_i(1) \\ y_i(1) \\ z_i(1) \\ 1 \end{Bmatrix}_{CS(1)} \right\|_2 \end{aligned} \tag{3.24}$$

The nine parameters determined in Eq. (3.24) can be used to calculate the unknown parameters $\bar{b}_{14}$ and $\bar{b}_{24}$ in Eq. (3.21):

$$\begin{Bmatrix} \bar{b}_{14} \\ \bar{b}_{24} \end{Bmatrix} = \begin{Bmatrix} u_i(1) \\ v_i(1) \end{Bmatrix}_{IM(1)} - \begin{bmatrix} \bar{b}_{11} & \bar{b}_{12} & \bar{b}_{13} \\ \bar{b}_{21} & \bar{b}_{22} & \bar{b}_{23} \end{bmatrix}_{CS(1)\rightarrow IM(1)} \begin{Bmatrix} x_i(1) \\ y_i(1) \\ z_i(1) \end{Bmatrix}_{CS(1)} . \tag{3.25}$$

Thus, the false displacement in Eq. (3.21) can be calculated at each frame by using both the camera motions $\bar{\mathbf{R}}_{3\times3}(k)$ and $\bar{\mathbf{T}}_{3\times1}(k)$ as determined by Eq. (3.18) and the parameters $\bar{b}_{11}$, $\bar{b}_{12}$, $\bar{b}_{13}$, $\bar{b}_{14}$, $\bar{b}_{21}$, $\bar{b}_{22}$, $\bar{b}_{23}$, $\bar{b}_{24}$, and $\{x_i(1) \quad y_i(1) \quad z_i(1)\}^{\mathrm{T}}_{CS(1)}$ as determined by Eqs. (3.24) and (3.25).

3.2.5. Displacement calculation with the error compensation

The true displacement with respect to the initial frame is given by $\{x_i(j) - x_i(1) \quad y_i(j) - y_i(1)\}^T_{WM}$ and can be obtained in every measurement frame with the dual cameras. If the inverse of $\widetilde{\mathbf{B}}_{WM \to IM(k)}$ is premultiplied with Eq. (3.10), the true displacement is expressed as:

$$\begin{Bmatrix} x_i(k) - x_i(1) \\ y_i(k) - y_i(1) \end{Bmatrix}_{WM} = \tilde{\mathbf{B}}^{-1}_{WM \to IM(k)} \begin{Bmatrix} u_i(k) - u_i(1) \\ v_i(k) - v_i(1) \end{Bmatrix}_{IM(k)} \tag{3.26}$$

Each term on the right side of Eq. (3.26) can be obtained as discussed in previous sections. The main camera measures $\{u_i(k) \quad v_i(k)\}^T_{IM(k)}$ for each frame, as discussed in Section 4.2.1. $\widetilde{\mathbf{B}}_{WM \to IM(k)}$ can be obtained in the initial measurement, as discussed in Section 4.2.2. The sub-camera helps calculate $\{u_i(1) \quad v_i(1)\}^T_{IM(k)}$ for each frame by using the 6-DOF camera motion, as discussed in Section 4.2.3. By combining the information from the main and sub-cameras, the true displacement $\{x_i(k) - x_i(1) \quad y_i(k) - y_i(1)\}^T_{WM}$ can be calculated to offer a camera motion-independent measurement.

The proposed method consists of two stages: calibration and measurement. The tasks in the calibration and measurement stages are as follows:

Calibration stage

1. $\widetilde{\mathbf{B}}_{WM \to IM(k)}$ is computed through the direct linear transform shown in Eq. (3.14) by using at least three features.
2. The sub-camera is calibrated with the camera calibration method proposed by Zhang [147] to determine the intrinsic camera parameters α, β, γ, μ, and v in Eq. (3.16).
3. The dual cameras are calibrated with Eqs. (3.24) and (3.25) to determine the unknown parameters $\bar{b}_{11}$, $\bar{b}_{12}$, $\bar{b}_{13}$, $\bar{b}_{14}$, $\bar{b}_{21}$, $\bar{b}_{22}$, $\bar{b}_{23}$, $\bar{b}_{24}$, and $\{x_i(1) \quad y_i(1) \quad z_i(1)\}^T_{CS(1)}$.

Measurement stage

1. The main camera measures $\{u_i(k) \quad v_i(k)\}^T_{IM(k)}$ for each feature point in the k-th image of the main target.
2. The sub-camera motion at the k-th frame (i.e., $\bar{\mathbf{R}}_{3\times3}(k)$ and $\bar{\mathbf{T}}_{3\times1}(k)$ in Eq.(3.18)) is calculated by using the camera calibration method [147] with α, β, γ, μ, and v. Then, $\bar{\mathbf{R}}_{3\times3}(k)$ and $\bar{\mathbf{T}}_{3\times1}(k)$ are employed in the false displacement computation in Eq. (3.21) with $\bar{b}_{11}$, $\bar{b}_{12}$, $\bar{b}_{13}$, $\bar{b}_{14}$, $\bar{b}_{21}$, $\bar{b}_{22}$, $\bar{b}_{23}$, $\bar{b}_{24}$, and $\{x_i(1) \quad y_i(1) \quad z_i(1)\}^T_{CS(1)}$.
3. The true displacement $\{x_i(j) - x_i(1) \quad y_i(j) - y_i(1)\}^T_{WM}$ in Eq. (3.26) is calculated by using $\widetilde{\mathbf{B}}_{WM \to IM(j)}$, $\{u_i(1) \quad v_i(1)\}^T_{IM(j)}$, and $\{u_i(j) \quad v_i(j)\}^T_{IM(j)}$.

The parameters that need to be determined in each stage are summarized in Table 9.

Table 9. Summary of the parameters to be determined in the proposed system.

Stage	**Measurement provider**	**Parameter to be determined**
Calibration stage	Main camera	$\widetilde{\mathrm{B}}_{WM\rightarrow IM(k)}$
	Sub-camera	$\alpha,\ \beta,\ \gamma,\ \mu,\ \nu$
	Dual cameras	$\bar{b}_{11},\ \bar{b}_{12},\ \bar{b}_{13},\ \bar{b}_{14},\ \bar{b}_{21},\ \bar{b}_{22},\ \bar{b}_{23},\ \bar{b}_{24},$ $\{x_i(1)\quad y_i(1)\quad z_i(1)\}^{\mathrm{T}}_{CS(1)}$
Measurement stage	Main camera	$\{u_i(k)\quad v_i(k)\}^{\mathrm{T}}_{IM(k)}$
	Sub-camera	$\bar{\mathbf{R}}_{3\times3}(k),\ \bar{\mathbf{T}}_{3\times1}(k),\ \{u_i(1)\quad v_i(1)\}^{\mathrm{T}}_{IM(k)}$
	Dual cameras	$\{x_i(k)-x_i(1)\quad y_i(k)-y_i(1)\}^{\mathrm{T}}_{WM}$

3.3. Validation

The proposed long-term displacement measurement method was validated through a numerical simulation, laboratory-scale test, and field test. The numerical simulation was conducted to validate the proposed displacement calculation algorithm described in the previous section; various pixel resolutions were considered to identify the minimum requirements for camera hardware. A dual-camera system was fabricated to meet the requirements and used in the indoor testing. Artificial camera movements were introduced to generate errors that should be compensated for by the proposed algorithm. The proposed dual-camera system was then implemented on a full-scale railway bridge to monitor displacement at the midspan for 550 days which is discussed in section 5.

3.3.1. Numerical validation

The dual-camera system was numerically validated with the simulation setup shown in Figure 21. The displacement at the midspan of a 20 m long bridge is considered; thus, the main and sub-targets were positioned to have a distance of 10 m. The main and sub-cameras were assumed to be identical and attached to each other with parallel optical axes in the opposite directions and 80 mm distance between the origins of *CM* and *CS*. The positions of the dual cameras were carefully selected so that the feature points within the main and sub-targets would be properly captured by the cameras. The fields of view of the main and sub-cameras were controlled to be about 200 mm × 150 mm and 150 mm × 100 mm, respectively. The targets were captured by the cameras with five different camera resolutions of 1920 × 1200, 3840 × 2400, 7680 × 4800, 15360 × 9600, and ∞ × ∞ (no quantization error involved) pixels. Although ∞ × ∞ resolution is not realistic, this case is considered in the numerical simulation to show the validity of the proposed method at an extreme condition. Because the subpixel algorithm was not considered for this analysis, the image coordinates of the features were rounded to integers. To generate the false displacement, the dual cameras were moved with respect to the initial position of the sub-camera *CS*(1), as listed in Table 10. If the camera motion in the field measurement is assumed to mainly be induced by temperature changes and deformation of the camera system, only small camera motions should be considered, as given in Table 10. The last 100 frames were prepared with uniformly distributed random motions bounded in ±1 mrad rotations about $x_{CS(1)}$, $y_{CS(1)}$, and $z_{CS(1)}$ and ±10 mm translations along $x_{CS(1)}$, $y_{CS(1)}$, and $z_{CS(1)}$.

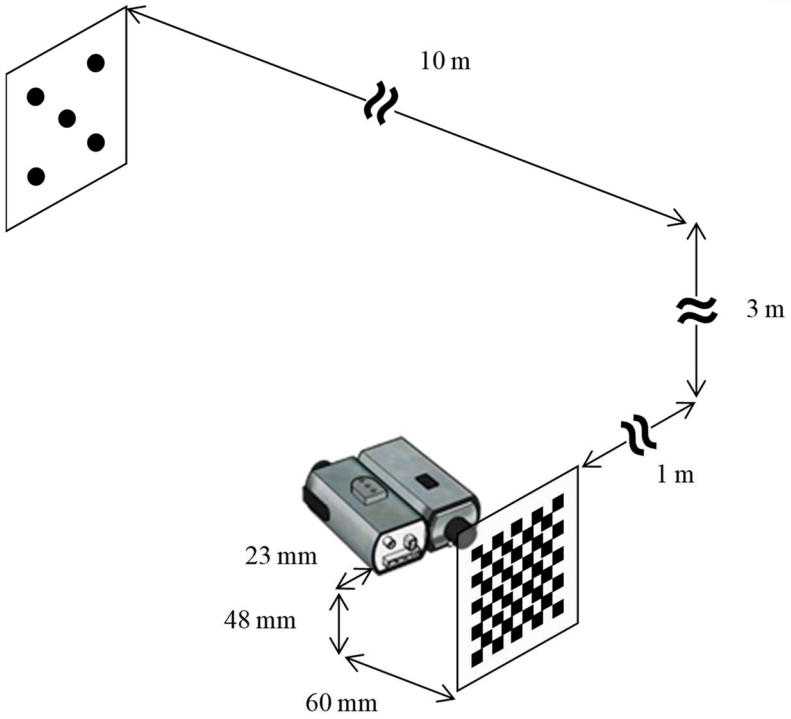

Figure 21. Simulation setup for cameras and targets.

Table 10. 6-DOF camera motions for numerical simulation.

Frame	**Camera motions**	
	Motion type	**Range**
1–100	Rotation about $x_{CS}(1)$	[−1 mrad, +1 mrad]
101–200	Rotation about $y_{CS}(1)$	
201–300	Rotation about $z_{CS}(1)$	
301–400	Translation along $x_{CS}(1)$	[−10 mm, +10 mm]
401–500	Translation along $y_{CS}(1)$	
501–600	Translation along $z_{CS}(1)$	
601–700	6-DOF random motions	

The resulting vertical displacements without and with the error compensation are shown in Figure 22(a) and Figure 22(b)–(f), respectively. Because the main target was fixed, the measured displacement by the main camera without the error compensation was the false displacement due to camera motion, as shown in Figure 22(a). The error could be suppressed by using the sub-camera, as shown in Figure 22 (b)–(f), which indicated that the performance improved for higher camera resolutions. The error levels can be further lowered by introducing the subpixel algorithm. Thus, the proposed algorithm was demonstrated to be capable of removing camera motion-induced errors.

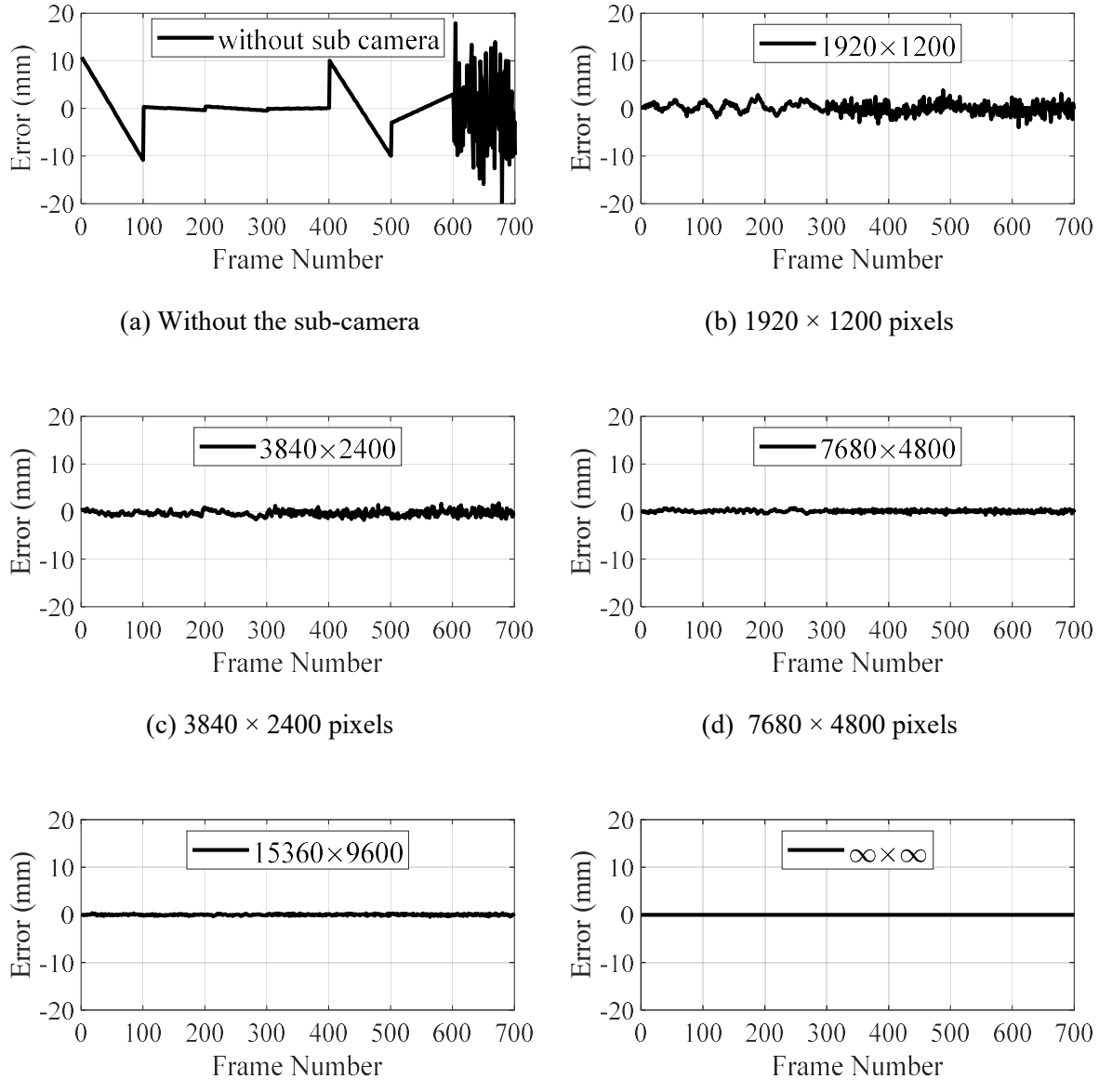

(a) Without the sub-camera

(b) 1920 × 1200 pixels

(c) 3840 × 2400 pixels

(d) 7680 × 4800 pixels

(e) 15360 × 9600 pixels

(f) ∞ × ∞ pixels

Figure 22. Effect of the sub-camera and its pixel resolution on the error compensation.

3.3.2. Laboratory-scale validation

The proposed method was validated in a laboratory environment with the dual-camera system. The experimental setup and hardware specifications are presented in Figure 23 and Table 11, respectively. The main target was designed to have five circular points on a black plate that was fixed 11 m apart from the camera system. A checkerboard was prepared for the sub-target, which was attached to a stationary wall. Two industrial-grade cameras were rigidly attached to each other by steel plates to build the dual cameras. The main and sub-cameras were equipped with a telescope lens and wide-angle lens for resolutions of 0.08 mm/pixel at a 11 m distance and 0.05 mm/pixel at a 50 mm distance, respectively. The pan-tilt was installed under the dual cameras (see Figure 23) and employed for camera calibration to determine the unknown parameters in Eqs. (3.24) and (3.25); this allowed for sensitive movement of the camera system. A total of 21 camera motions were generated for the camera calibration. After the calibration, the pan-tilt motor was manipulated to generate gradual three-dimensional rotations and translations of the dual cameras to simulate long-term camera movements.

Table 11. Hardware specifications.

Hardware	**Specification**
Main camera	Model: GS3-U3-23S6C-C 1920 × 1200 pixel resolution Telescope lens (focal length: 800 mm) 1/1.2″ image sensor 0.08 mm/pixel at 11 m distance
Sub-camera	Model: GS3-U3-23S6M-C 1920 × 1200 pixel resolution Wide angle lens (focal length: 6 mm) 1/1.2″ image sensor 0.05 mm/pixel at 50 mm distance
Main target	Five white circles on a black background Horizontal interval: 15 mm Vertical interval: 11 mm
Sub-target	32 × 31 checkerboard 2 mm interval

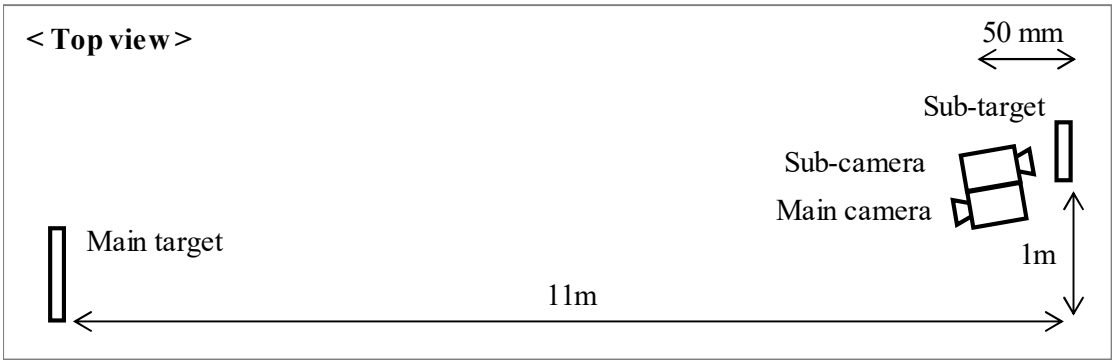

(a) Schematic view

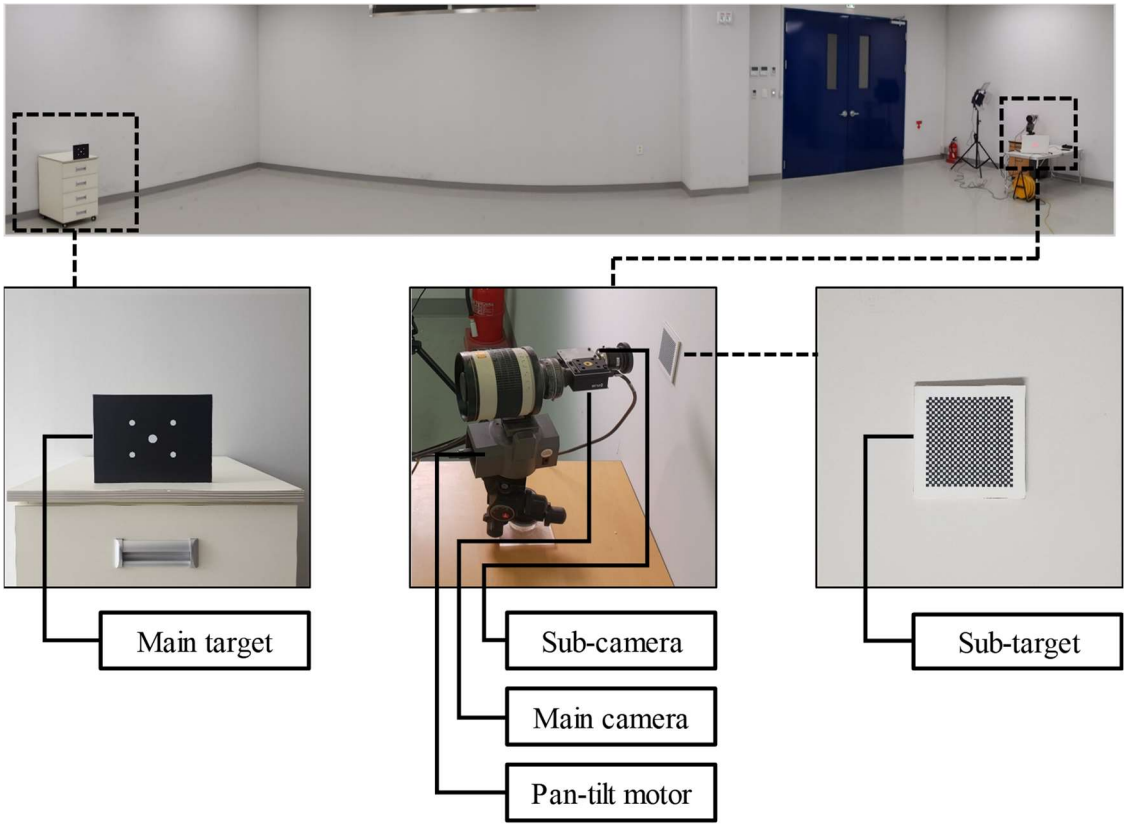

(b) Hardware configuration

Figure 23. Laboratory test setup.

The dual-camera system was carefully designed to conform the assumptions for long-term displacement measurement postulated in Section 3.2. The affine camera assumption was valid for the main camera because $||x - x_{affine}||_2$ was less than 1 pixel, which was calculated based on the working distance (d_0 was 11 m), the depth motion (Δz was less than 5 mm), and position of the feature point near the center ($x - x_0$ was less than 100 pixels). The sub-camera was a perspective camera as the magnification due to the sub-mm of depth motion was visible in the captured images. The relative position between the main and sub cameras was successfully constrained through the stainless-steel plates as shown in Figure 24. This steel only deformed 12 μrad of rotation per 1 N·m of twist and 90 μm per °C of thermal expansion, which is negligibly small. The sub-target was prepared with foamex polyvinyl chloride as light as 11 g such that permanent fixation of the target to the wall was feasible by Loctite 401. Hence, assumptions that the movements other than the dual-camera body are fixed were valid for the laboratory-scale experiment.

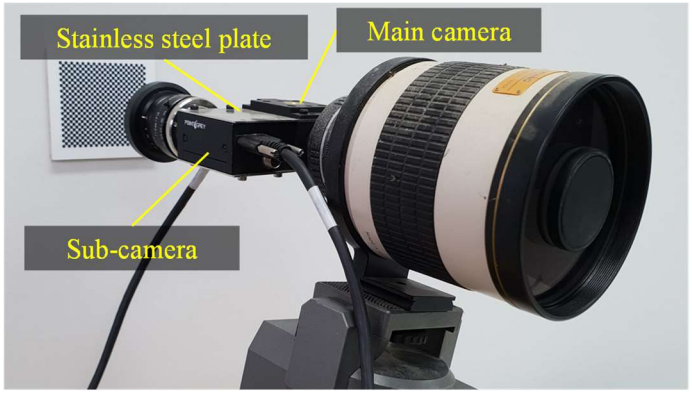

(a) Composition of the dual camera

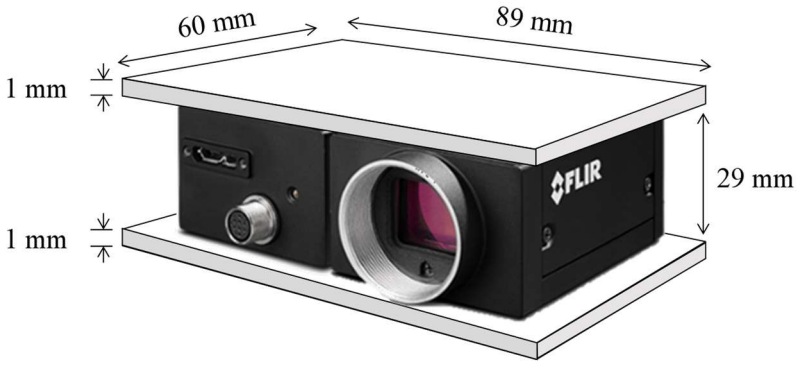

(b) Dimension of the steel plates

Figure 24. Preparation of the dual camera.

The displacement measured by the main camera without the error compensation (denoted as "single camera" hereafter) was compared with that corrected by the dual-camera system. In the calibration stage, 21 sets of images were taken by the main and sub-cameras upon each intentional movement by the pan-tilt. Once the unknown parameters were all determined in the calibration process, 6-DOF camera motions are applied to the camera using the pan-tilt as shown in Figure 25, which produced a maximum false displacement of 44.1 mm for the main camera, as shown in Figure 26(a). Stepwise camera motions were observed because of the limited performance of the pan-tilt. The false displacement was compensated for with the dual-camera system, which resulted in a false displacement of 1.1 mm as shown in Figure 26(b). Thus, the feasibility of the dual-camera system was demonstrated; it reduced the motion-induced error from 44.1 mm to 1.1 mm.

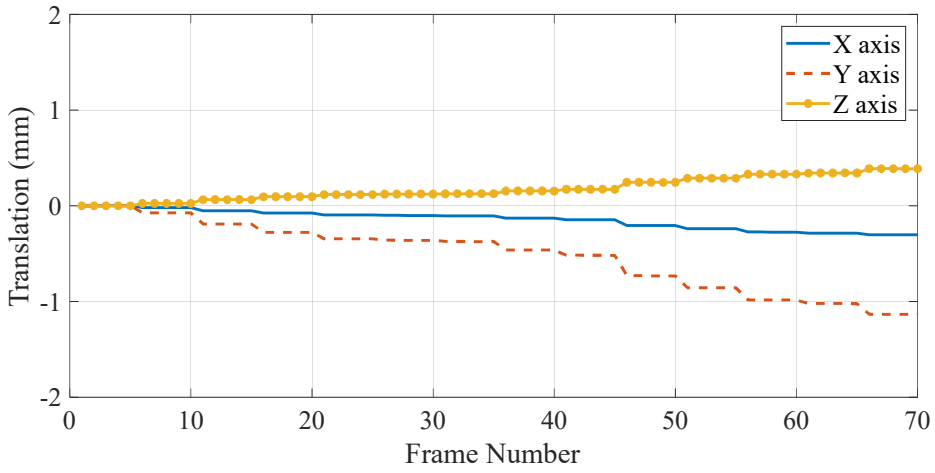

(a) Translation

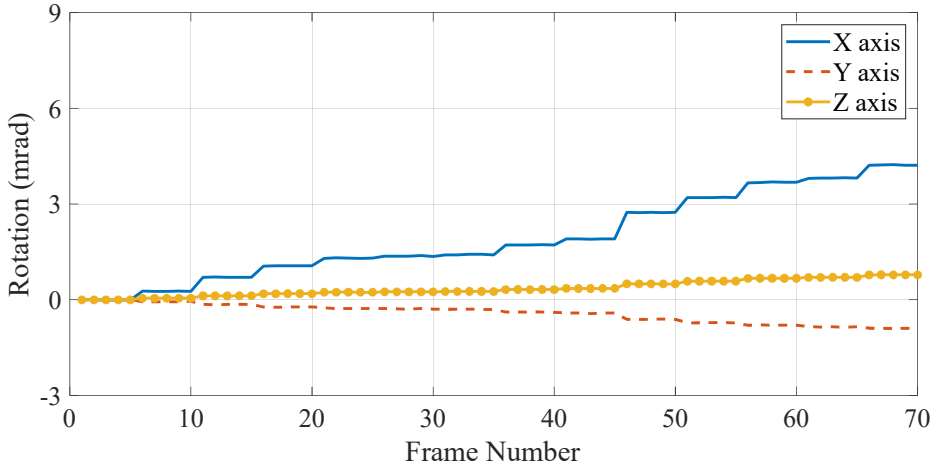

(b) Rotation

Figure 25. 6-DOF camera motions for the laboratory-scale test.

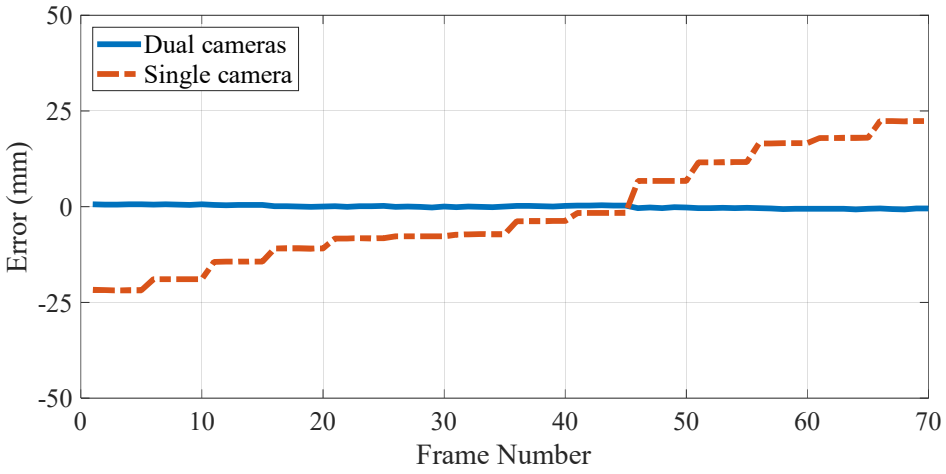

(a) Comparison between the dual-camera and single-camera methods

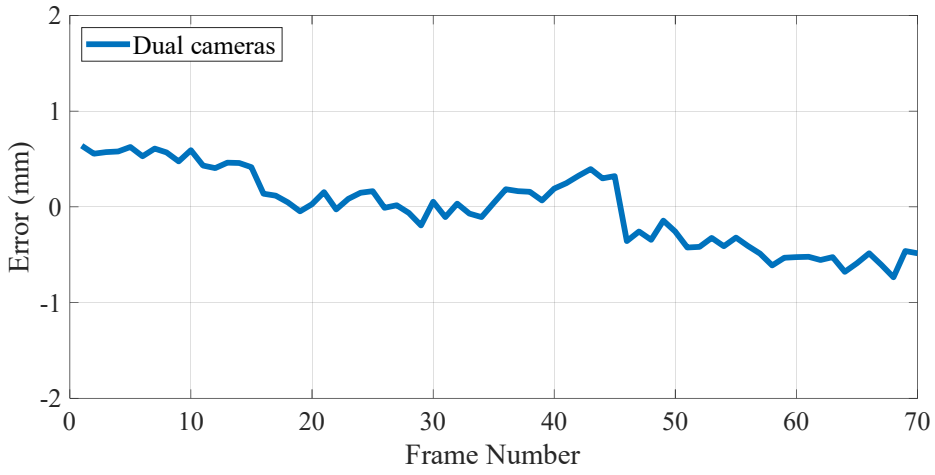

(b) Magnification of the dual-camera method

Figure 26. Results of laboratory tests.

3.4. Summary and Discussion

A long-term displacement measurement method is proposed by using dual-camera system. Main camera measures structural displacement as conventional method does; thus, camera motion is directly reflected as the false displacement. Sub-camera is attached to the main camera to detect camera body motion. A physical relationship between the sub-camera motion and the false displacement is derived. The false displacement computed by using the sub-camera motion is subtracted from the displacement measured by main camera to extract true structural displacement. The proposed method is numerically validated that reliable measurement was enabled even with the arbitrary camera motion. The dual-camera system is fabricated to conduct laboratory-scale experiment by which false displacement from the camera motion was also successfully compensated. The proposed method will be further validated through field test on a full-scale railway bridge in Section 5.

4. LiDAR-Based Long-Term Displacement Measurement System

4.1. Introduction of the LiDAR-based displacement measurement system

The limitation in long-term application of the LiDAR-based approach was identified to be the permanent installation. As discussed in Section 2.2.2, LiDAR is an expensive device that permanent installation should be avoided. Thus, a long-term monitoring method is proposed by using temporary installation scheme, which can trace displacement since initial measurement.

The proposed method employs strategic reflector topology offering continuous monitoring without permanent installation. The reflectors are attached over the full-scale structure to include essential displacement information such that displacement compared to initial measurement can be measured regardless of the LiDAR position. In addition, rather than scanning entire bridge, the reflectors are intensively scanned to reduce scanning time for higher resolution. An image processing method is employed in processing the three-dimensional scan data offering reduced processing time and automized displacement calculation. In summary, the proposed method provides intermittent measurement of the LiDAR enabling long-term tracking of the bridge displacement, quick and precise scanning, and efficient data processing and displacement calculation as listed in Table 12.

Table 12. Comparison between the conventional and the proposed methods.

Conventional approaches	**Proposed method**
Permanent installation − Short-term measurement	Intermittent installation − Long-term measurement
Entire scanning − Long scanning time − Coarse scan − Big data size	Intensive scanning on reflectors − Short scanning time − Dense/focused scan − Small data size
3D data-based algorithm − Long processing time − Unreliable point matching − Manual displacement computation	Image processing-based algorithm − Short processing time − Reliable point matching − Automized displacement computation

4.2. Long-Term Measurement based on Strategic Reflector Topology

The proposed approach uses the LiDAR system to obtain long-term displacement measurements of bridges. To efficiently address the issues described in the previous section, this study employs a reflector-based high-precision measurement and a novel displacement calculation algorithm that allows LiDAR to be arbitrarily positioned. This section describes the proposed displacement measurement strategy using LiDAR, focusing on (1) reflector topology, (2) measurements of reflector position, and (3) algorithm for long-term displacement.

4.2.1. Reflector topology

The proposed method employs reflectors attached to specific locations on the exterior of the bridge to be measured. The LiDAR system then scans small areas (including the reflectors) to enable calculations of reflector locations. Compared to previous studies that measure displacement by scanning the entire bridge [103, 144, 148], the reflector-based measurements are highly accurate and entail considerably shorter measurement and computation times by decreasing the amount of displacement information provided. Thus, the reflector-based scheme offers efficient and accurate measurement if displacements are required at only several specific locations.

The proposed approach requires a reflector topology that is tailored to building the LiDAR position-independent displacement calculation. To avoid the need for a permanent installation, we assume that the LiDAR hardware is placed in the field only when bridge displacement measurements are required. The reflector topology consists of two reflector groups as shown in Figure 27: (1) a reference group that provides a reference vector and (2) a measurement group, where displacement relative to the reference vector is calculated. The reference vector, $\{s\}_k$, at the k^{th} measurement is defined as a mean of the 3D coordinates for each reflector in the reference group as

$$\{s\}_k = \frac{1}{N}\sum_{i=1}^{N}\{s_i\}_k \tag{4.1}$$

where N is the number of reflectors in the reference group and $\{s_i\}_k$ is the 3D coordinate of the i^{th} reflector at the k^{th} measurement. Deformation measurements of the bridge girder relative to the bridge piers are often sought, and thus the reference reflector group on the piers can be used to produce girder displacement relative to the piers. In a case where pier displacement needs to be also considered, a fixed location that is not on the bridge should be used for the reference group. LiDAR measures the varying positions of the reflectors in the measurement group over time, and these measurements are then used to calculate displacements relative to the reference vector.

As the vertical displacement is often of interest, the reflectors need to be prepared such that a unit vector normal to the deck plane can be clearly obtained. Multiple reflectors (more than three) in the measurement group can be used to arrange a plane for the bridge girder. The vector normal to the measurement group coincides with the gravity vector for uninclined bridges. Even if a bending or a torsional deformation of the deck lead deviation of the normal vector to the gravity vector, the error induced by the improper normal vector is negligibly small (0.02% error for 1° rotation of the normal vector). To reduce the normal vector error, the reflectors should be symmetrically deployed to the midspan. Once the normal vector is computed, vertical displacement can be obtained by projecting the displacement relative to the reference vector onto the gravity vector. An example of reflector topology is shown in Figure 27, where multiple reflectors in the reference and measurement reflector groups are attached to the bridge girders and piers. The measurement group under the girder is symmetrically placed around the midspan and can be used to find the gravity vector. The reference group is used to calculate a reference vector starting at the piers and ending with the measurement group. This reflector configuration enables the LiDAR position-independent displacement calculation that offers a practical solution for long-term measurement.

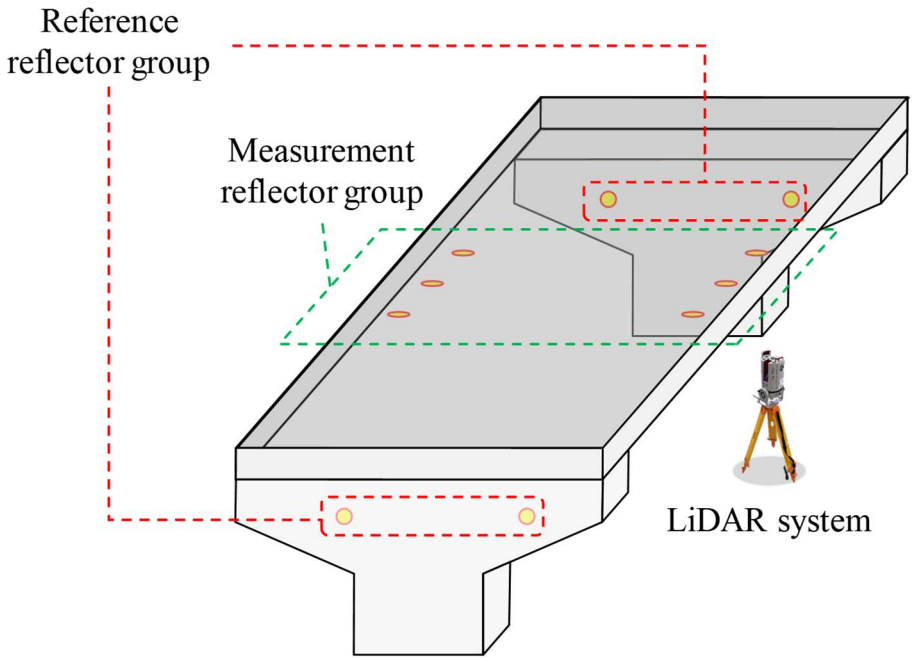

Figure 27. Reflector topology showing the reference and measurement reflector groups.

4.2.2. Binarization-based segmentation for extraction of reflector position

The proposed method provides a scanning scheme that determines the reflector positions efficiently with minimal manual handling of the point cloud. LiDAR performs high-resolution scanning only for the regions of interest (ROIs) containing each reflector rather than the entire structural body. The reflector-based scanning scheme allows the reflector positions to be accurately identified with considerably reduced measurement and computation time. In this subsection, the procedure for the scanning scheme is described in detail.

For efficient measurement, the point cloud measurement using LiDAR consists of two steps with global and local scanning as shown in Figure 28. Initially, the entire bridge is quickly scanned with a low spatial resolution to identify the approximate location of each reflector. The point cloud data containing the 3D coordinates and reflectance is converted into a reflectance map that shows the reflectance with respect to the polar and azimuthal angles. Due to the high reflectance, the reflectors can be clearly recognized, allowing ROIs to be assigned around each reflector. Subsequently, LiDAR automatically scans each ROI with a high spatial resolution. Note that scanning the reflectors takes much less time than scanning the entire structure. The densely scanned point clouds for each ROI is used in the following segmentation process that separates the reflectors from the backgrounds.

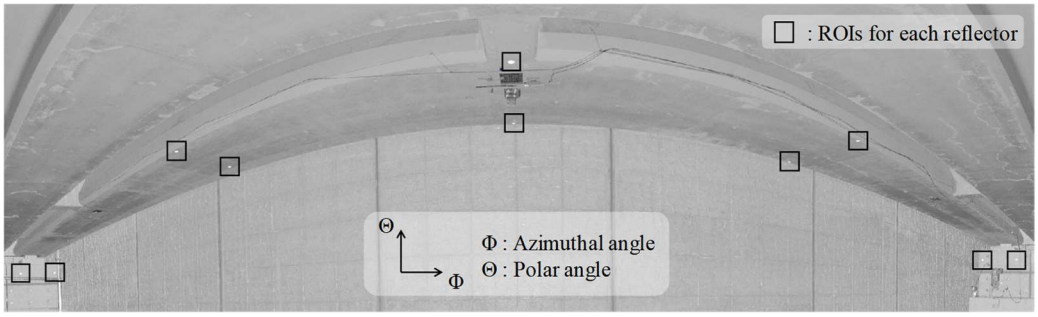

(a) Reflectance map after global coarse scanning

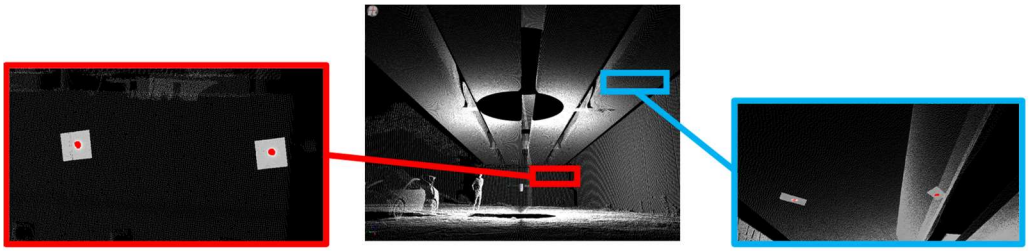

(b) Global and local scanning

Figure 28. LiDAR canning scheme.

A binarization-based segmentation method is employed to accurately determine the 3D coordinates of the reflector position from the 3D point clouds for each reflector. The reflector is distinguished from the surrounding background by its reflectance at each scanning ROI, because the reflectance level of the reflectors is higher than that of the surrounding background as shown in Figure 29(a). Otsu's binarization method [149] is applied to select the threshold reflectance level that separates the reflector points from the background. Figure 29(b) shows the results of segmentation using Otsu's threshold, where the black points have higher reflectance than the Otsu's threshold and the grey points have lower reflectance. The centroid of the selected reflector points is calculated and used as the representative location of the reflector.

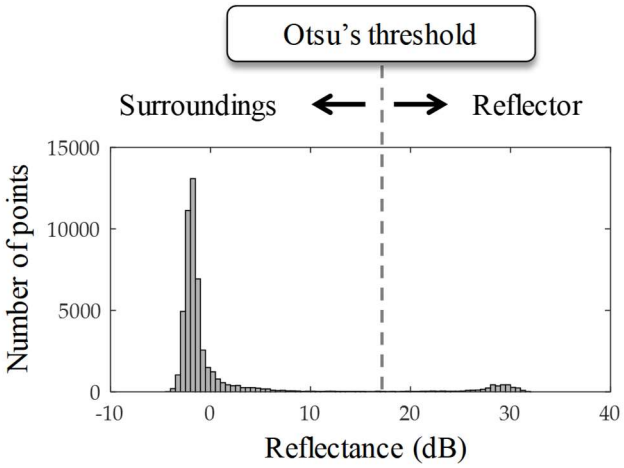

(a) Reflectance histogram

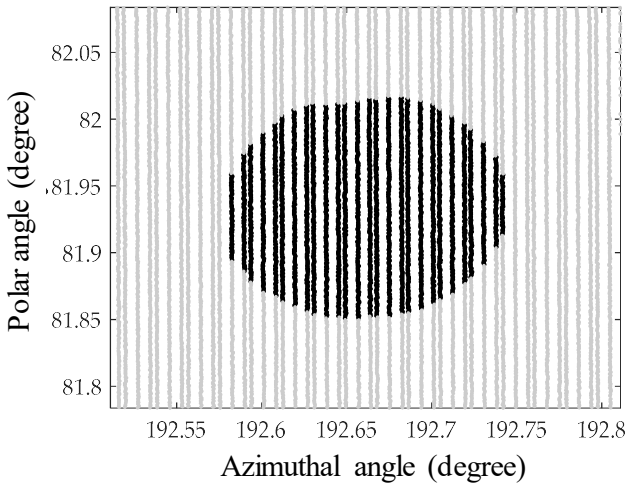

(b) A segmented reflector in the reflectance map

Figure 29. Reflector segmentation.

4.2.3. LiDAR-based displacement computation algorithm for long-term monitoring

The measured reflector positions are used to calculate the bridge displacement. The algorithm is particularly designed to calculate the displacement regardless of the LiDAR positions. Let $\{b_i\}_k$ be the i^{th} reflector vector in the LiDAR coordinate system at the k^{th} measurement as shown in Figure 30. Position of $\{b_i\}_k$ relative to $\{s\}_k$, denoted as relative reflector vector $\{p_i\}_k$, is defined as

$$\{p_i\}_k = \{b_i\}_k - \{s\}_k . \tag{4.2}$$

Although LiDAR is repositioned for every measurement, the length of $\{p_i\}_k$ is constant over time unless the bridge deck and pier move, and only displacement along the vertical direction causes changes in the length. Thus, the vertical component of $\{p_i\}_k$ needs to be extracted for LiDAR position-independent measurement.

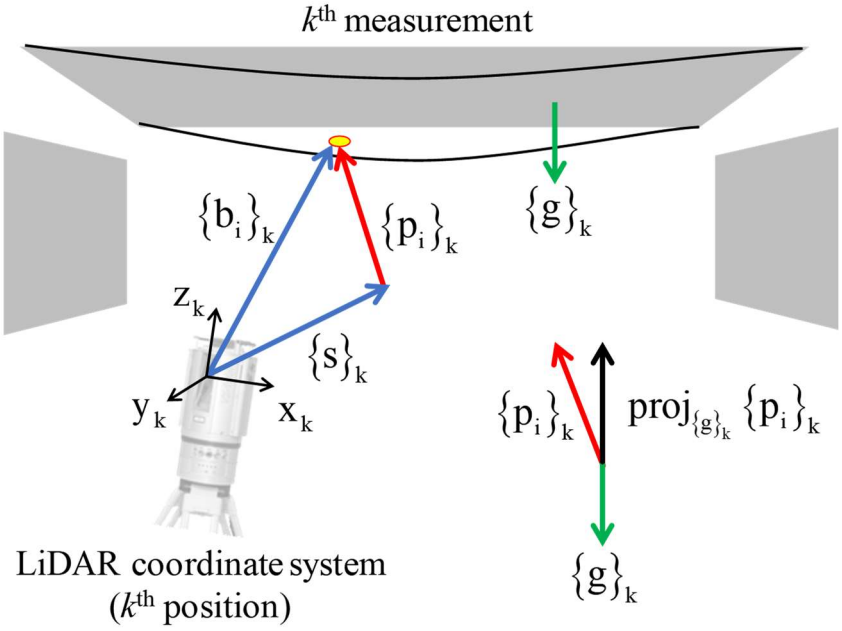

Figure 30. Schematic of position vectors during the k^{th} measurement.

The gravity vector needs to be obtained if vertical displacement is of interest. The measurement group can be used to approximately determine the gravity vector. Let $\mathbf{B}_k$ be a matrix containing all reflector vectors in the measurement group at the k^{th} measurement as

$$\mathbf{B}_k = \begin{bmatrix} \{b_1\}_k & \{b_2\}_k & \cdots & \{b_M\}_k \end{bmatrix} \tag{4.3}$$

where M is the number of reflectors in the measurement group. The covariance matrix of $\mathbf{B}_k$ can be written as

$$\mathbf{\Sigma}_k = \frac{1}{M}\mathbf{B}_k\mathbf{B}_k^{\mathrm{T}} - \{\mu\}_k\{\mu\}_k^{\mathrm{T}} \tag{4.4}$$

where $\{\mu\}_k$ is the mean of the reflector vectors in the measurement group at the k^{th} measurement. The eigen-decomposition of the covariance matrix $\mathbf{\Sigma}_k$ is

$$\mathbf{\Sigma}_k = \begin{bmatrix} v_1 & v_2 & v_3 \end{bmatrix} \begin{bmatrix} \lambda_1 & 0 & 0 \\ 0 & \lambda_2 & 0 \\ 0 & 0 & \lambda_3 \end{bmatrix} \begin{bmatrix} v_1 & v_2 & v_3 \end{bmatrix}^{\mathrm{T}} \tag{4.5}$$

where v_1, v_2, and v_3 are the normalized eigenvectors, and λ_1, λ_2, and λ_3 are the corresponding eigenvalues sorted in an ascending order (i.e., $\lambda_1 \leq \lambda_2 \leq \lambda_3$). The reflectors in the measurement group are attached to the bridge deck, hence their position vectors form an approximate plane. As a result, the column vectors of $\mathbf{\Sigma}_k$ are almost linearly dependent, which results in a zero eigenvalue (i.e., $\lambda_1 \cong 0$), and its corresponding eigenvector, v_1, is perpendicular to the plane. In conclusion, the gravity vector, $\{g\}_k$, coincides with v_1, which is the eigenvector of $\mathbf{\Sigma}_k$ with the smallest eigenvalue.

Vertical deflection of the bridge deck is calculated as the vertical component of the $\{p_i\}_k$ for the i^{th} point at the k^{th} measurement. The relative reflector vector is projected onto the gravity vector as shown in Figure 4 to extract the vertical component from $\{p_i\}_k$. Therefore, the vertical displacement of the i^{th} point at the k^{th} measurement with respect to the initial measurement can be written as

$$\{u_i\}_k = \{g\}_k^{\mathrm{T}}\{p_i\}_k - \{g\}_1^{\mathrm{T}}\{p_i\}_1. \tag{4.6}$$

The formulation for the vertical displacement is independent of all different LiDAR positions at each measurement. Thus, the series of measured $\{u_i\}_k$ becomes the long-term displacement. As such, long-term monitoring of bridge displacement can be acquired using the proposed method.

4.3. Validation

4.3.1. Laboratory-scale validation

A series of laboratory experiments were conducted to validate the proposed long-term displacement measurement strategy using LiDAR. The tests examined the ability to measure displacement independent of the LiDAR position, which is a key requirement for enabling long-term measurements to be conducted with the temporarily installed LiDAR at arbitrary locations. Displacements were measured using three different LiDAR positions to investigate the LiDAR position-independence of the proposed method.

A flexible desk (shown in Figure 31(a)) was placed on the ground floor to measure vertical displacement at the center relative to two pillars. Five reflectors were placed on the table and four on pillars for the measurement and reference groups, respectively. A stand-alone LiDAR system (which is described in detail in Table 13) was employed to conduct the laboratory validation. The LiDAR was positioned on a platform 6.4 m above the floor to ensure that the angles between the reflectors and the LiDAR were large enough to obtain high reflectance. The LiDAR was moved to three different positions, as shown in Figure 31(b). For each measurement location, static loads were increasingly applied to the center of the desk. In consideration of the LiDAR positions and loads, a total of 12 test cases were considered, and the experimental cases are summarized in Table 14. A laser displacement sensor (LDS) was placed under the desk (as shown in Figure 31(a)) and was used to acquire the reference displacement.

Table 13. LiDAR specifications.

Criteria	**Specification**
Model	VZ-1000 (Riegl)
Laser wavelength	Near infrared
Measurement speed	Up to 122,000 points/second
Distance scan	Standard deviation: 5 mm
Vertical scan	Minimum spatial interval: 0.001˚ (Equivalent spatial resolution: 0.35 mm for 20 m distance)
Horizontal scan	Minimum spatial interval: 0.006˚ (Equivalent spatial resolution: 2.09 mm for 20 m distance)

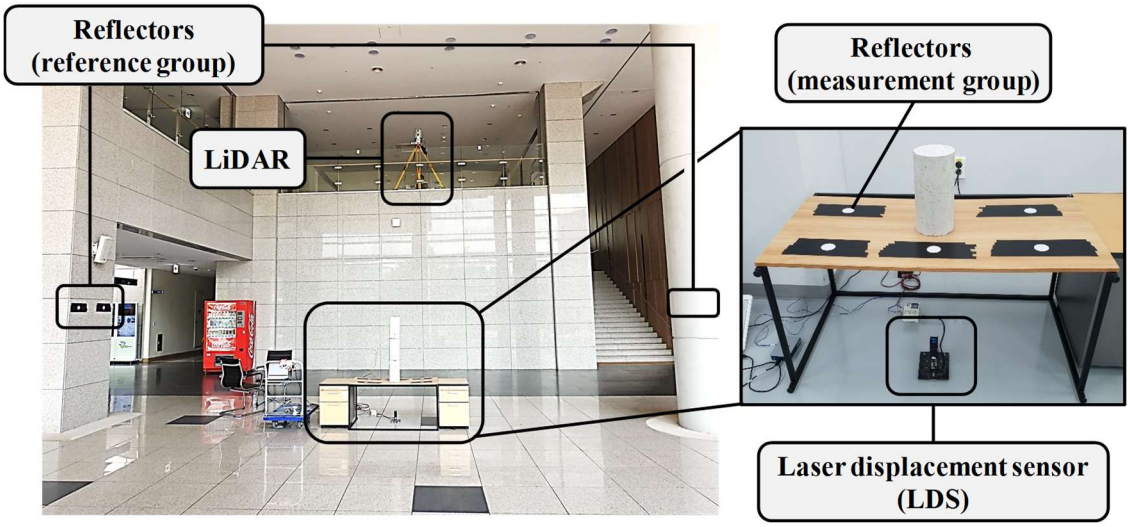

(a) Experimental setup

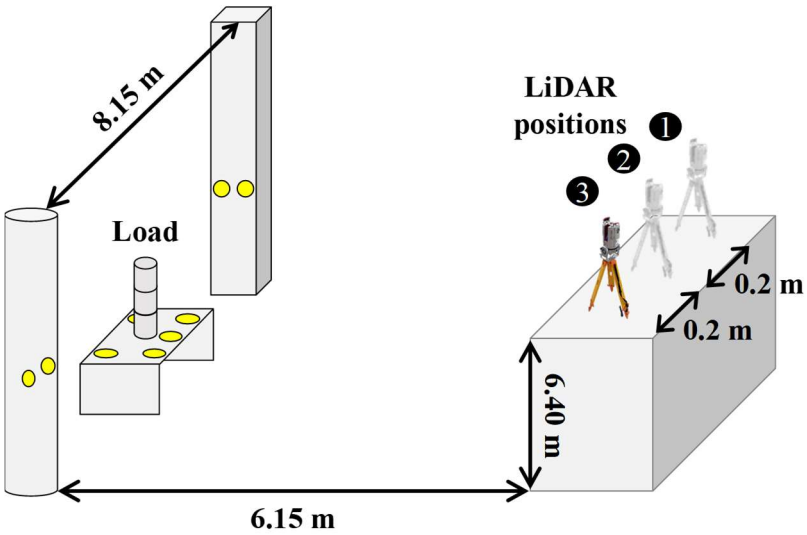

(b) Schematic view

Figure 31. Laboratory test.

Table 14. Experimental cases.

Test case	1	2	3	4	5	6	7	8	9	10	11	12
LiDAR position	1				2				3			
Number of loads	0	1	2	3	0	1	2	3	0	1	2	3

A comparison between displacements measured by LDS and LiDAR is shown in Figure 32, where it is evident that both sensors successfully measure displacements in each test case and show good agreement. Note that the displacements for each test case are compared with the initial measurement in case 1; thus, displacements in the 5th and 9th cases are non-zero. Measurement differences between LDS and LiDAR are mostly less than 0.5 mm, as shown in Figure 32(b), and are not related to the LiDAR position. These results show that the proposed method is viable for measuring the long-term displacement of civil engineering structures.

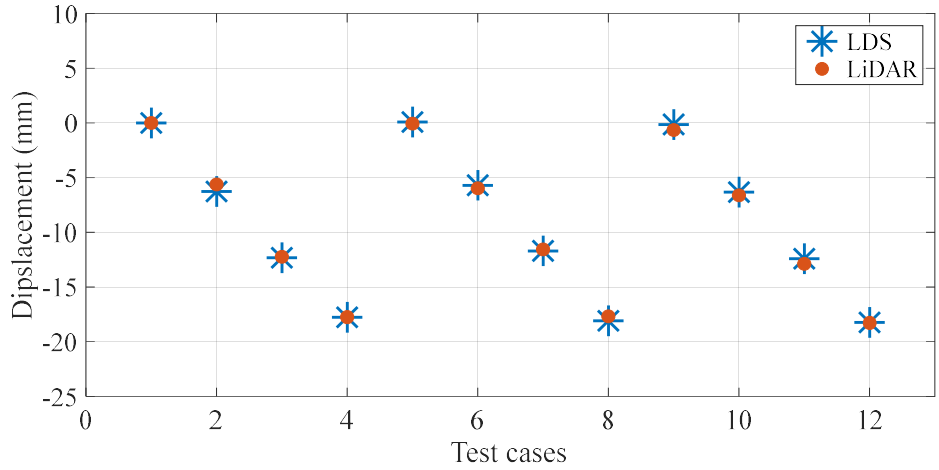

(a) Displacement comparison

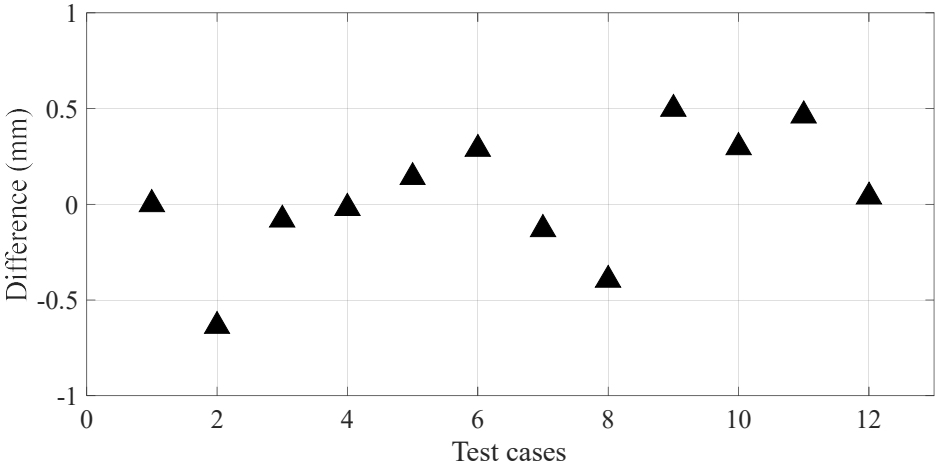

(b) Differnece between LDS and LiDAR

Figure 32. Lab-scale displacement measurement testing result.

4.4. Summary and Discussion

The LiDAR-based long-term displacement measurement method tailored to full-scale bridge was discussed. Reflectors are strategically deployed over the structure to offer displacement measurement in disregard of LiDAR position offering permanent installation-free monitoring. In addition, through focused scanning scheme data size and scanning time are noticeably reduced. Image processing method is adopted to automatically extract centroidal position of each reflector. The position of the reflectors is used to calculate long-term displacement that compares deviation from the initial measurement along the vertical direction. Laboratory scale test showed 0.5 mm of measurement error with a LiDAR positioned 6 m apart from the bridge model. Full-scale validation is shown in Section 5 with a railway bridge with 40 m span length.

5. Field Validation of Proposed Displacement Measurement Systems

5.1. Experimental Setup

5.1.1. Testbed information

The proposed long-term displacement measurement strategies were applied to a full-scale bridge. A prestressed concrete railway bridge on Osong railway test track, of which location is shown in Figure 33, was selected as a testbed. The target bridge was constructed in accordance with the schedule summarized in Table 15, during which precast girders were erected on piers, slab and barrier were cast-in-place, and track ballast was placed. In this experiment, the measurements began at age of 90th day (December 15, 2017) to monitor long-term displacement induced by the superimposed dead loads (slab, barrier walls, and ballast) and their long-term effects.

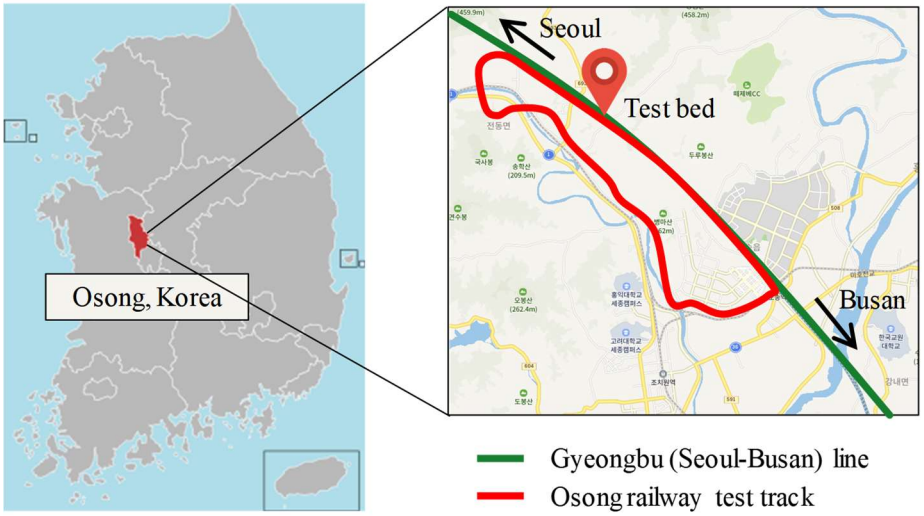

Figure 33. Location of the testbed.

Table 15. Initial construction schedule.

Date	Age (days)	Construction stage
2017.09.17	1	Concrete casting for girder and tendon in tension
2017.09.21	5	Detension of the prestressing tendon
2017.11.05	50	Girder erection & cross beams installation
2018.02.07	144	Concrete casting for the slab
2018.03.14	179	Concrete casting for the barrier walls
2018.08.13	331	Track ballast placement

The bridge comprises of four identical prestressed concrete girders, which are denoted as G1, G2, G3, and G4 in Figure 34(a). Each girder was designed to have trivet-shaped cross section as shown in Figure 34(b) with width of 1.8 m, height of 2.2 m, and length of 39.9 m. Because trains were supposed to pass over the girders G1 and G2 in the operation stage, displacement at the midspan of the girder G1 was monitored in this field experiment.

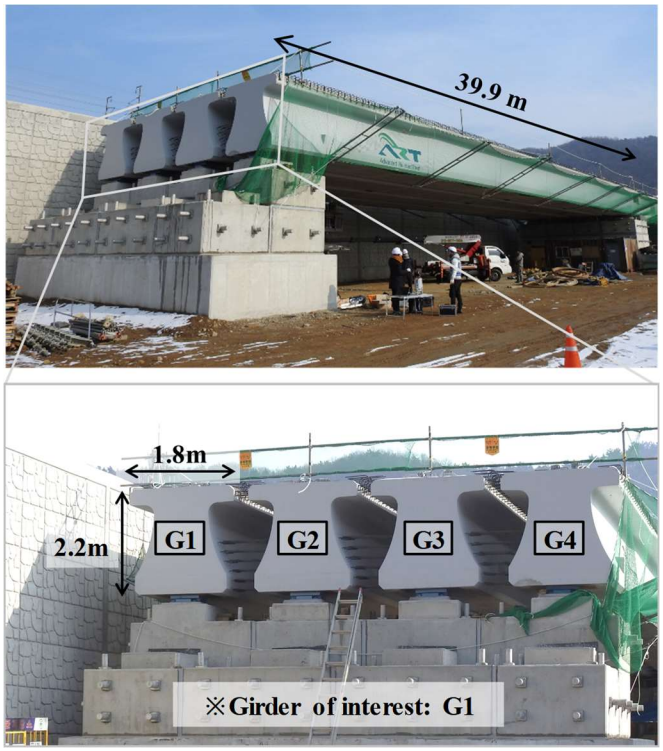

(a) Bridge under construction (December 19, 2017)

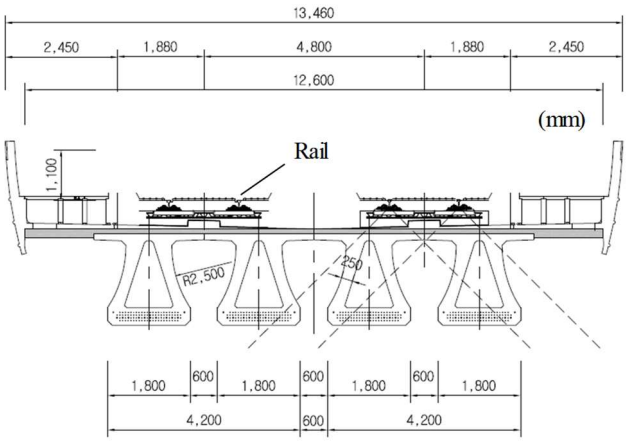

(b) Cross-section of the bridge

Figure 34. Testbed information.

A finite element model of the target bridge was implemented to simulate the long-term displacement. MIDAS Civil [150], which is a commercial software for implementing finite element methods, was employed to build the model as shown in Figure 35(a). Characteristic compressive strength of 30 MPa and 49 MPa at 28 days were adopted respectively for the concrete of the slab and the girder. Moisture curing was considered with notional size of 411 mm, 70% of relative humidity, 24.52 kN/m^3 of concrete density, and rapid hardening high strength cement. Using these information, immediate and time-dependent displacement responses were calculated as shown in Figure 35(b) in accordance with the loading history in Table 15 and the creep and shrinkage model in KCI 2012 [151]. Initially, upward displacement is observed due to the tendon prestressing and its creep effect. Subsequent dead loads applied by cross beams, slab, barrier walls, and track ballasts cause immediate downward deflection with the corresponding creep effect. This simulation result was compared with actual displacement measured by the proposed methods for the field validation.

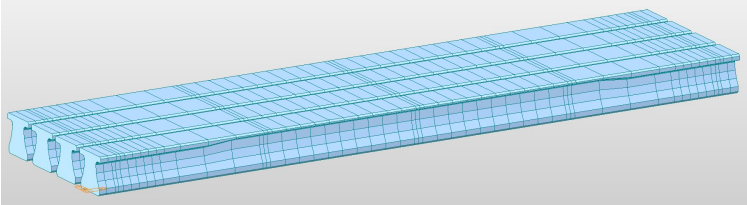

(a) Finite element model of the testbed using MIDAS

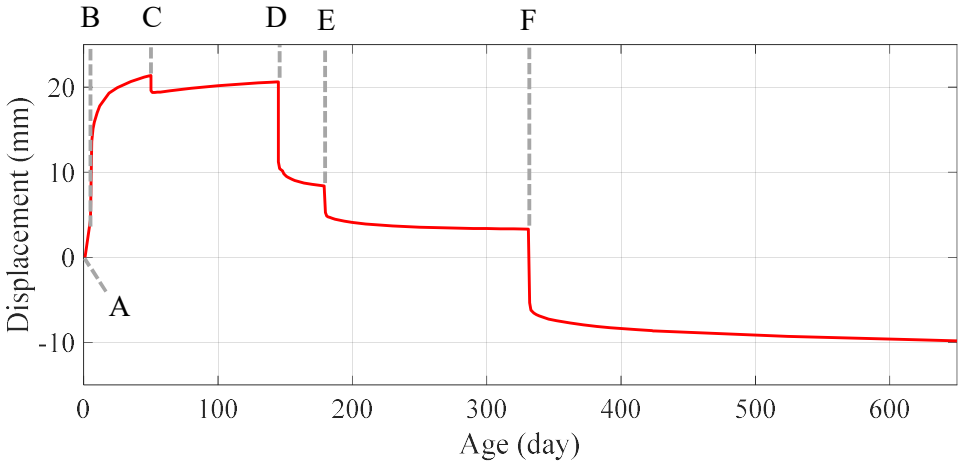

A	Concrete casting and tendon in tension	D	Concrete casting for the slab
B	Detension of the prestressing tendon	E	Concrete casting for the barrier walls
C	Girder erection & cross beams installation	F	Track ballast placement

(b) Dsplacment simulated for 650 days

Figure 35. Expected bridge displacement using the finite element model.

5.1.2. Sensor deployment scheme

Five different types of sensors were deployed over the structure to measure midspan vertical displacement. They are dual cameras, LiDAR, strain gauges, ring gauge (a strain-based displacement transducer), and LVDT, of which measurement schedule and schematic view are shown in Table 16 and Figure 36, respectively. Dual-camera system was installed at a pier to measure movement of the main target attached to the midspan for 548 days without occupying the space under the bridge. LiDAR system was regularly placed in the field to measure displacement on a weekly basis for 548 days. Note that LiDAR was retrieved after each measurement avoiding permanent installation of the sensor in the field. Strain gauges were attached to the bridge for indirect displacement estimation. However, the harsh field environment gradually weakened bonding attachment between the bridge and the gauges that the sensors were eventually detached after 184 days. Ring gauge and LVDT, which are the well-known conventional displacement transducers, were installed under the bridge to measure displacement during the ballast placement. Because of the pavement under the bridge in September 2018, these contact-type sensors stopped measurement 72 days after the installation.

Table 16. Sensor measurement schedule.

Sensor	Measurement period (duration in days)	Sampling period
Dual cameras	2017.12.15–2019.06.16 (548 days)	1 minutes
LiDAR	2017.12.15–2019.06.16 (548 days)	1 weeks
Strain gauges	2017.12.20–2018.11.30 (184 days)	10 minutes
Ring gauge	2018.06.25–2018.09.06 (72 days)	10 minutes
LVDT	2018.06.25–2018.09.06 (72 days)	10 minutes

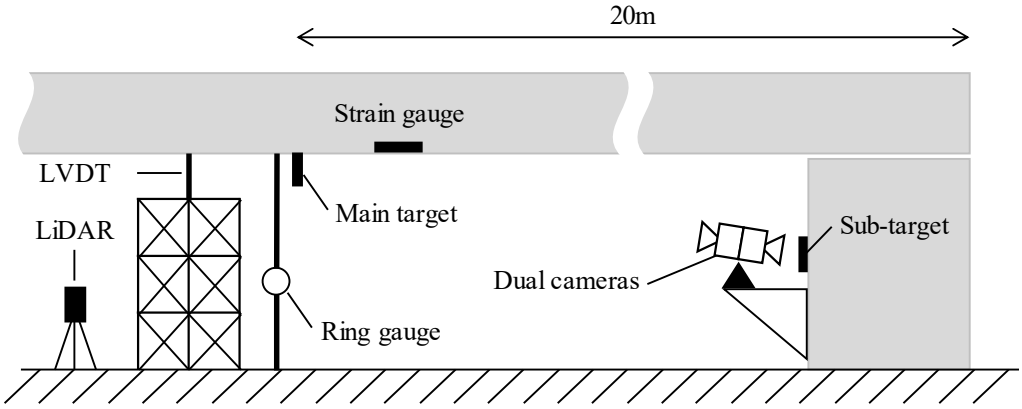

Figure 36. Schematic view of the experimental setup.

Dual-camera system was prepared to measure midspan displacement from the pier as shown in Figure 37. The main target, the sub-target, and the dual cameras used for the laboratory-scale validation in Chapter 3.3.2 (full list can be found in Table 11) were employed in the field test. The main target was attached to the midspan of the bridge with five white circles and black background. Here, the distance between the main target and the cameras was doubled compared to the laboratory test in Chapter 3.3.2. Therefore, the main target was designed to be twice as large as the one used for the laboratory test to keep the image size the same. The sub-target printed on a Foamex polyvinyl chloride was attached to the pier by Loctite 401. Due to the lightweight of the target and strong adhesiveness, the sub-target was assumed to be permanently fixed to the pier without movement. The dual cameras were prepared with two identical 1920 ×1200 resolution of cameras constrained by steel plates, as in the laboratory test, to assure complete fixation between the cameras. A pan-tilt motor, of which model name is Bescor MP-360, was positioned under the dual-camera to artificially generate motions during the calibration process as discussed in Section 3.2.5. Once the unknown parameters were determined with artificially generated random motions in the calibration procedure, displacement measurement commenced with one minutes of sampling rate that the drift errors induced by camera ego-motion were compensated for by using the proposed method demonstrated in Chapter 3.

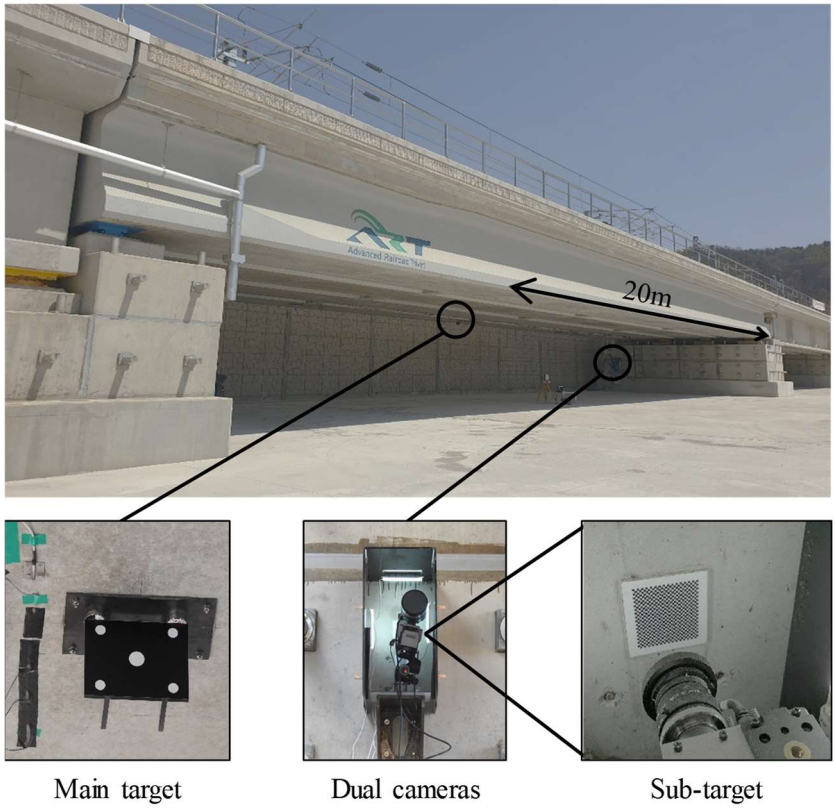

Figure 37. Experimental setup of the dual-camera system.

The LiDAR system was regularly installed in the field to measure long-term displacement at the midspan of the bridge with respect to the stationary piers. A total of ten reflectors were attached to the bridge deck and piers as shown in Figure 38(a). Six reflectors on the deck were gathered to build the measurement group discussed in Chapter 4.2, by which the normal vector of the deck plane was calculated for every measurement. Four reflectors in the piers formed stationary reference point which is a vector from the piers to the midspan. Location of the reflectors on the deck and piers were measured by the temporarily installed LiDAR as shown in Figure 38(b). Firstly, the entire bridge was quickly scanned at a low spatial resolution to determine region of interest (ROI) for each reflector. Then a focused scanning in high spatial resolution was followed to find their exact positions. This measurement scheme was repeatedly conducted on a weekly basis to obtain a long-term displacement.

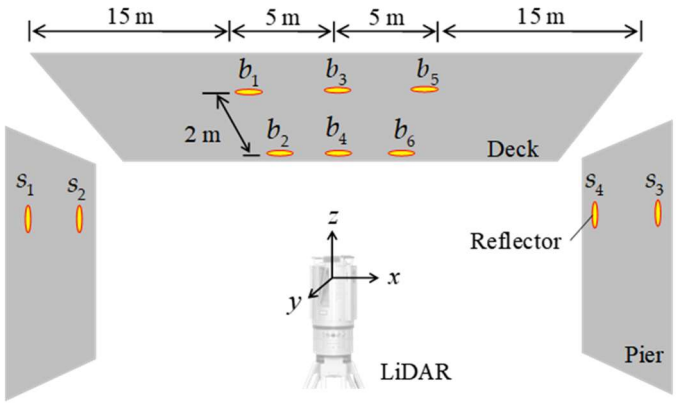

(a) Reflector deployment scheme

(b) LiDAR system configuration

Figure 38. Experimental setup of the LiDAR system.

Three concrete strain gauges were installed on the bridge as shown in Figure 39. The 120 Ω concrete strain gauges (PL-60-11-1LJC-F, Tokyo Sokki) were attached to the bottom of the girder with 10 m of interval as in Figure 39(b) by Loctite 401, a well-known adhesive. The gauge wires were connected to the data logger (CR10X, Campbell Scientific) installed at the pier shown in Figure 39(a). The logger recorded the strains for every 10 minutes, which were converted to displacement by using a mode shape-based indirect displacement computation method [152]. Herein, location of the neutral axis is a necessary constant to convert the strains into the structural displacement, which is generally unknown if the strains are solely employed. In this experiment, the immediate displacement during the slab placement as measured by the dual-camera system was employed to calculate the unknown constant. The displacement estimated by the strains was compared with the one measured by dual cameras and LiDAR.

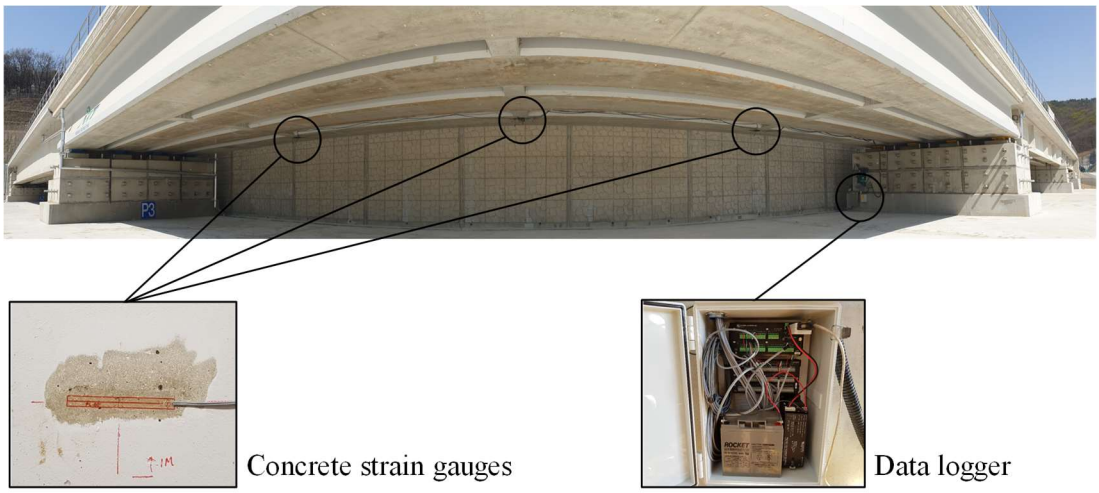

(a) Experimental view

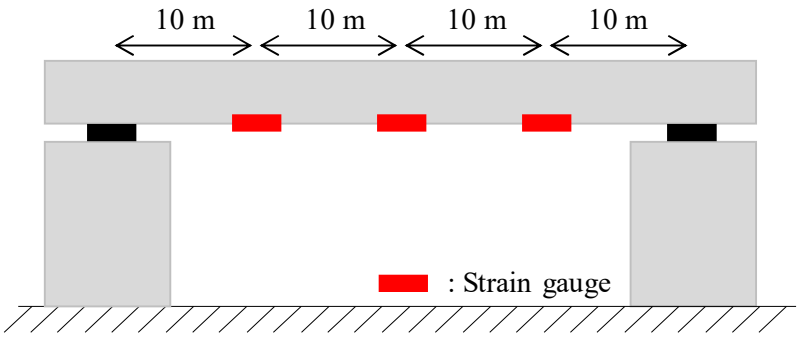

(b) Deployment scheme of the strain gauges

Figure 39. Experimental setup of the strain gauges.

Two contact-type displacement transducers were installed in the field to compare the conventional sensors with the proposed measurement strategies. LVDT was installed under the midspan of the bridge as shown in Figure 40. To contact the tip of the LVDT to the bridge, scaffold was placed under the bridge that allowed displacement measurement with respect to the ground. Ring-type displacement transducers, denoted as ring gauge in Figure 40, was installed on the ground. The gauge was connected to the measurement point on the bridge via steel wire. A wind shield was covered the wire to avoid noise from the vibration. Note that these contact-type sensors occupy the space under the bridge which limited measurement during the early construction stage until the age of 200 days. Data logger recorded displacements for every 10 minutes that is used to validate the performance of the proposed strategies in comparison to the conventional methods.

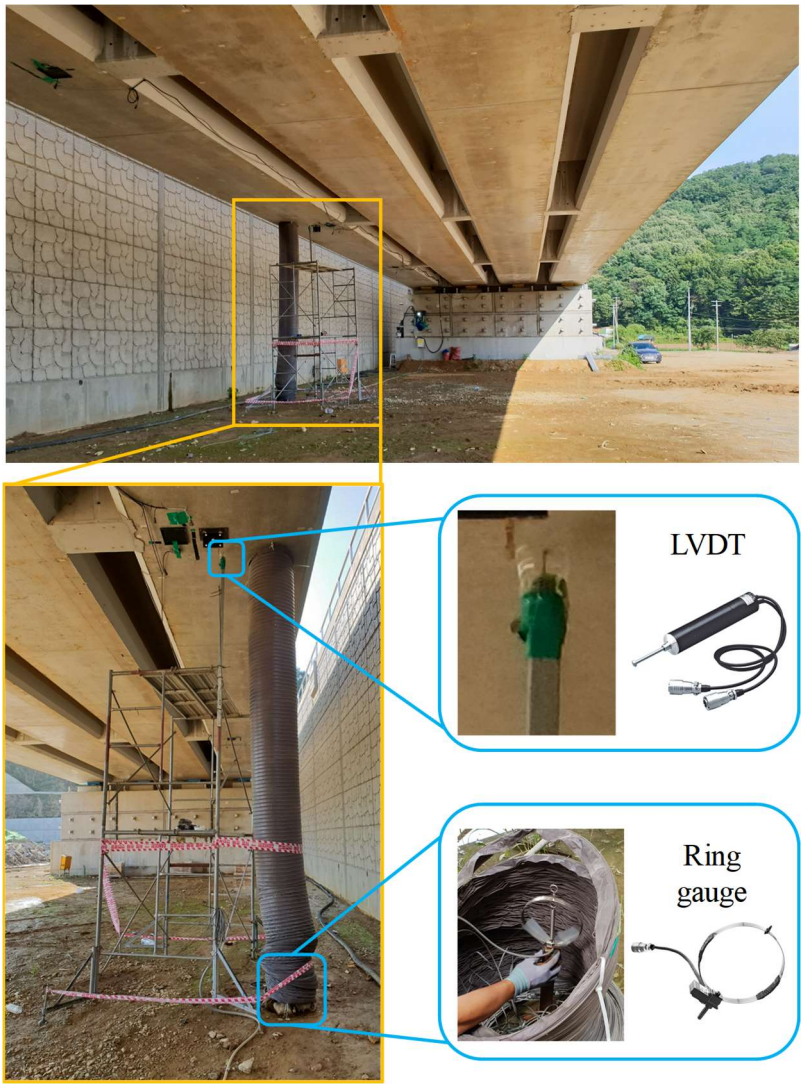

Figure 40. Experimental setup of the contact-type displacement transducers.

5.2. Field Test Result

5.2.1. Long-term displacement analysis

Bridge displacements measured by five different sensors were compared with the one computed by the finite element method in Figure 40. Initial measurement values were adjusted to the displacement computed by the finite element model for overall comparison. The displacements measured by dual cameras, LiDAR, and strain gauges were respectively increased by 21.59 mm, 22.66 mm, and 20.59 mm to align data at 144th day. LVDT and ring gauges commenced measurement at the age of 282 days, of which data were increased by 3.33 mm and 3.79 mm to coincide with the finite element model. Overall trend of the displacement measured by dual cameras, LiDAR, and LVDT agrees well with the FE model, whereas the one measured by the strains and ring gauge does not due to harsh field environment. Not only the immediate deflection induced by the slab and the ballasts, but also the slowly developing displacement due to the creep effect were observed. Based on the construction schedule in Figure 41 and weather condition collected from the Korea Meteorological Administration [153] as shown in Figure 42, this chapter provides detailed analysis on the long-term displacement to identify mechanical causes of displacement as well as the source of daily fluctuation.

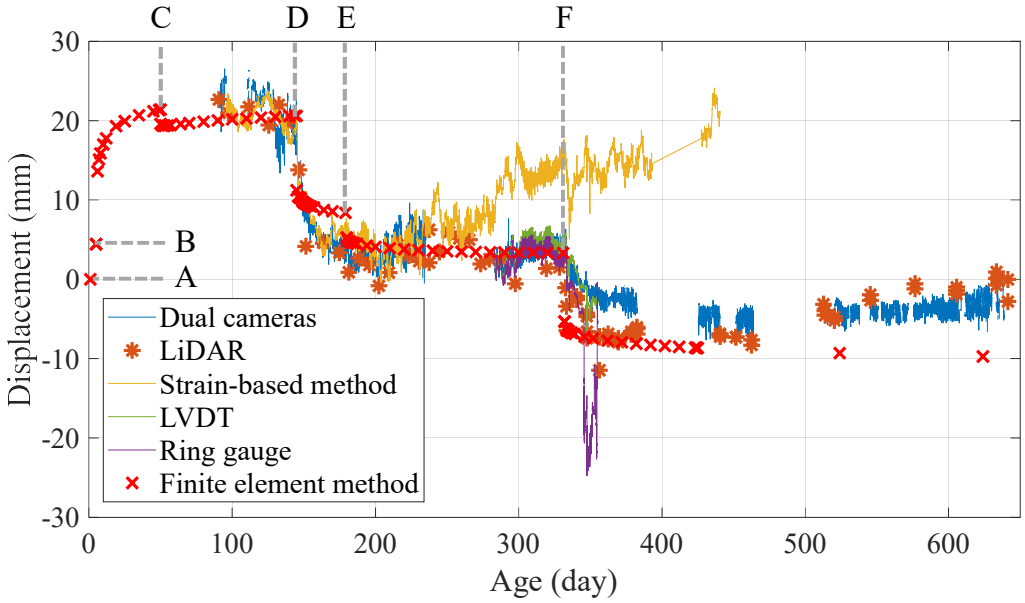

A	Concrete casting and tendon in tension	D	Concrete casting for the slab
B	Detension of the prestressing tendon	E	Concrete casting for the barrier walls
C	Girder erection & cross beams installation	F	Track ballast placement

Figure 41. Long-term displacement comparison (Age of 0–650 days).

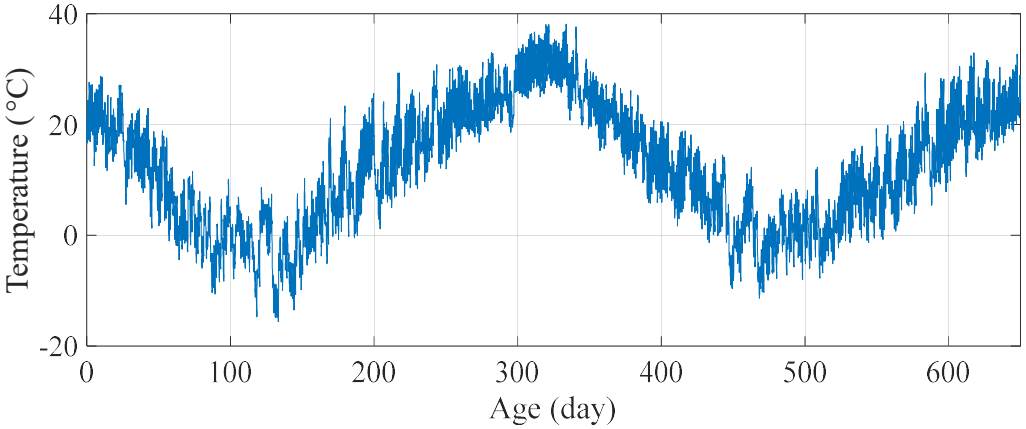

(a) Ambient temperature (Age of 0–650 days)

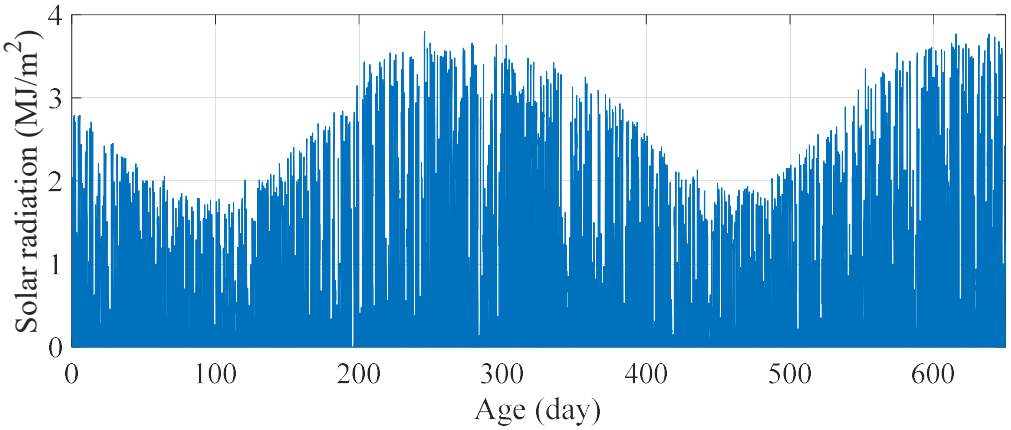

(b) Solar radiation (Age of 0–650 days)

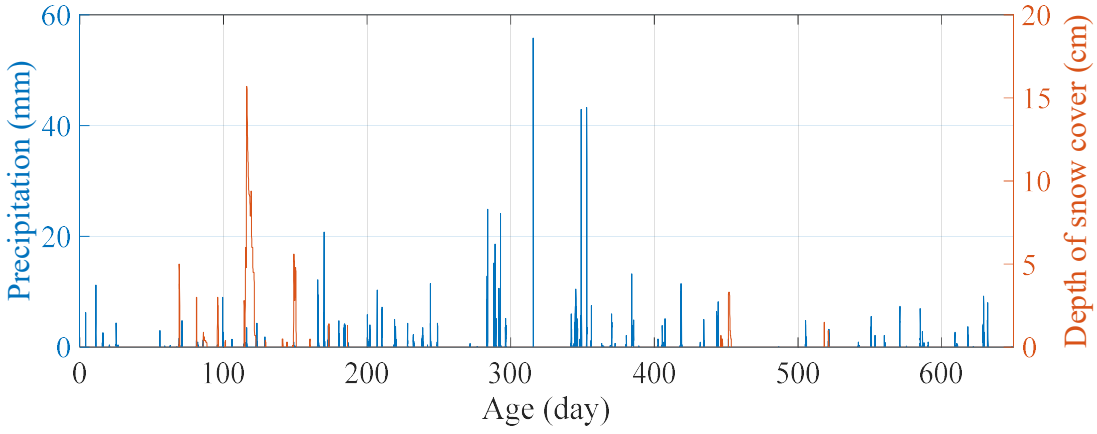

(c) Precipitation and depth of snow cover (Age of 0–650 days)

Figure 42. Weather conditions (Age of 0–650 days)

The bridge displacements during the first 55 days (December 15, 2017–February 08, 2018) of measurement are shown in Figure 43. Based on the finite element model, the displacement converged to 20 mm in upward direction due to the prestressing tendon, shrinkage, and creep. On the other hand, displacements measured by dual cameras, LiDAR, and strains fluctuated around 20 mm mainly because of sunlight and snow. For the first 5 days of the displacement measured by dual cameras, 5 mm of daily displacement was observed in daytime due to sunlight. Note that the girders were not covered by the slab, thereby sunlight easily induced temperature gradient resulting in the upward displacement. Due to power failure in the age of 95–110 days, measurement failed resulting in long discontinuity for the dual cameras result. Snow was stacked on the girder on the age of 114–128 days as shown in Figure 44 which reduced the daily fluctuation by blocking the direct sunlight. A lighting system was installed on 114th day so that the displacement could be measured all day and night. Cold wave during the age of 129–133 days affected downward bias around 17 mm that recovered after then. In case of LiDAR, displacement was measured every week. Even though LiDAR was positioned at different point for each measurement, displacement shows good agreement with other sensors and the finite element model. During the initial 55 days, up to 3 mm fluctuation was observed in the LiDAR results. Strain-based method also shows stationary displacement with 3 mm of daily fluctuation. Direct sunlight was also the main source of daily displacement for the strain-based method, thereby small fluctuation is observed for the days with little solar radiation.

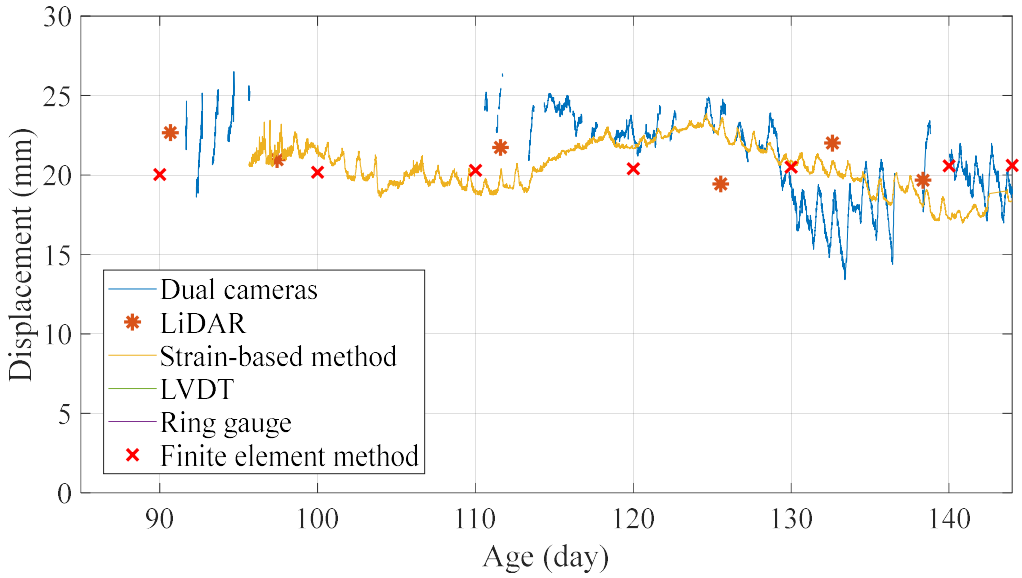

Figure 43. Long-term displacement comparison (Age of 85–145 days).

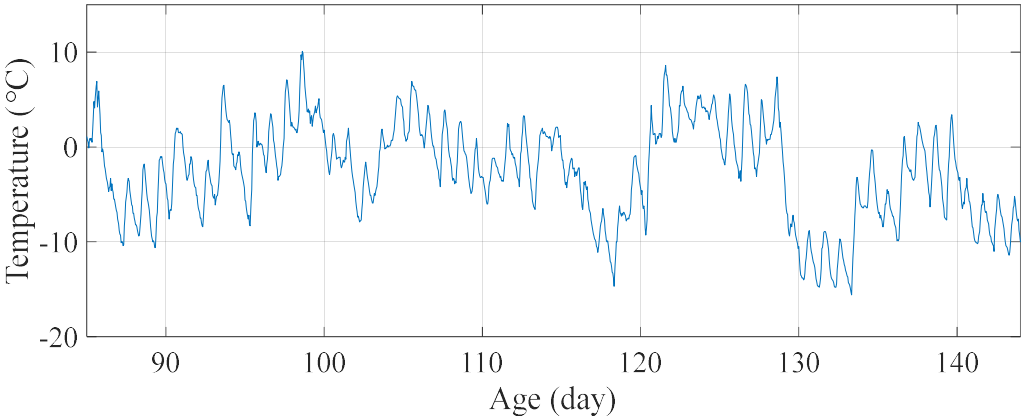

(a) Ambient temperature (Age of 85–145 days)

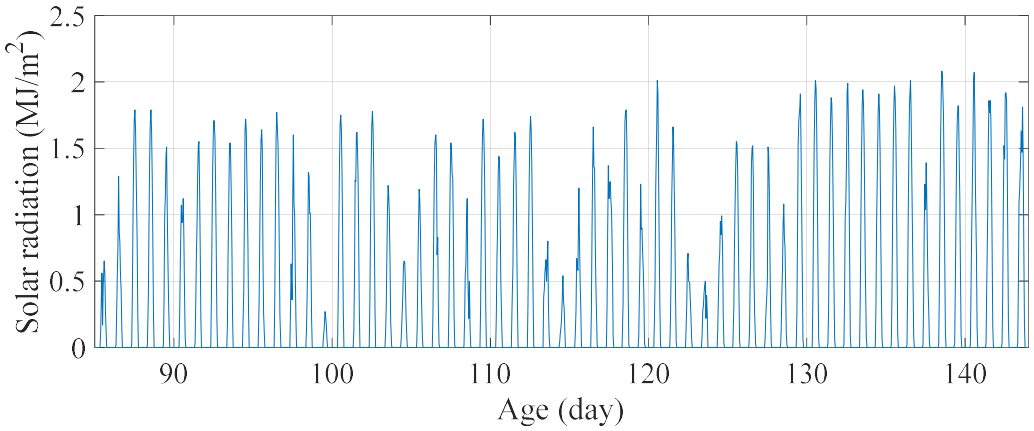

(b) Solar radiation (Age of 85–145 days)

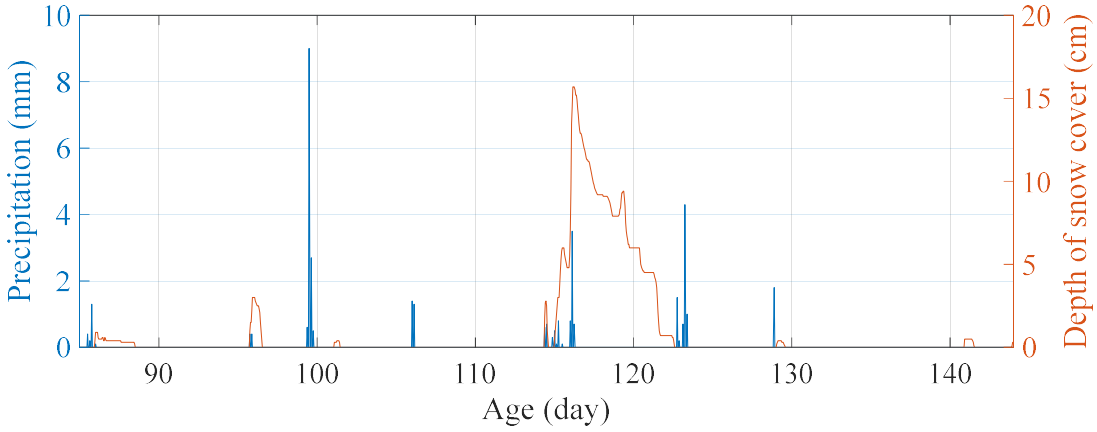

(c) Precipitation and depth of snow cover (Age of 85–145 days)

Figure 44. Weather conditions (Age of 85–145 days).

The bridge displacements during the age of 135–180 days (January 29, 2018–March 15, 2018) are shown in Figure 45. As the concrete for the slab was cast on the girder in 145th day, an instantaneous displacement of 6.5 mm, 6.0 mm, and 6.6 mm was measured respectively by the dual cameras, the LiDAR, and the strains. Steam curing was adopted after the concrete casting as shown in Figure 46, which caused upward displacement in 145th–148th days. Since then, displacement was gradually developed until 180th day mostly due to the creep effect. Total amount of creep was about 8mm; thereby creep coefficient was approximately calculated to be 1.3. In addition to the displacement induced by the self-weight and the creep effect, weather condition shown in Figure 47 was involved. Clouds blocked sunlight around 165th, 170th, and 173rd days which reduced daily fluctuation of the displacement. Snow was stacked on the slab in the age of 148–151 days, whereas the influence of the snow was negligibly small.

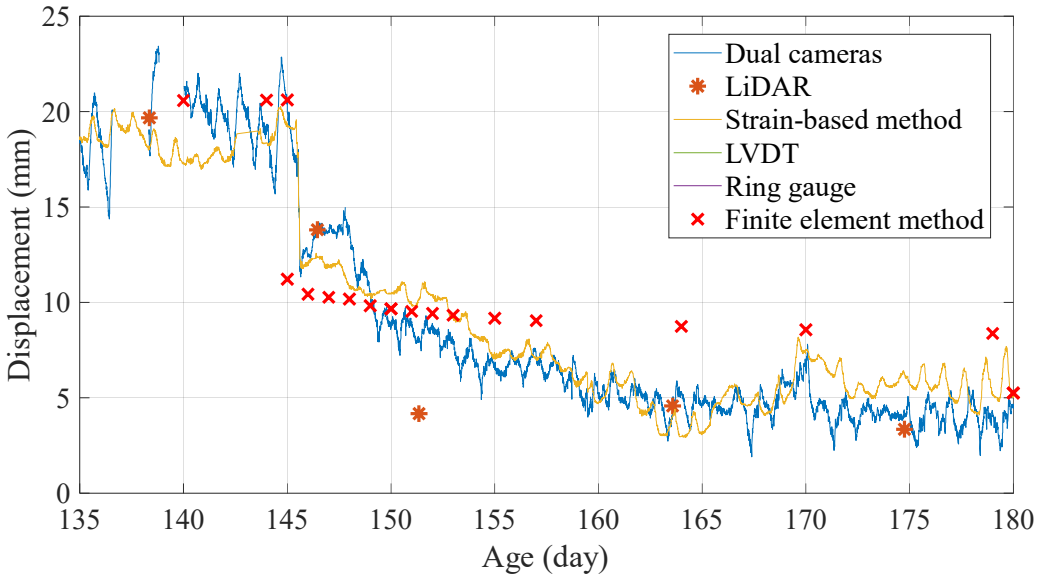

Figure 45. Long-term displacement comparison (Age of 135–180 days).

Figure 46. Construction site during and after the steam curing.

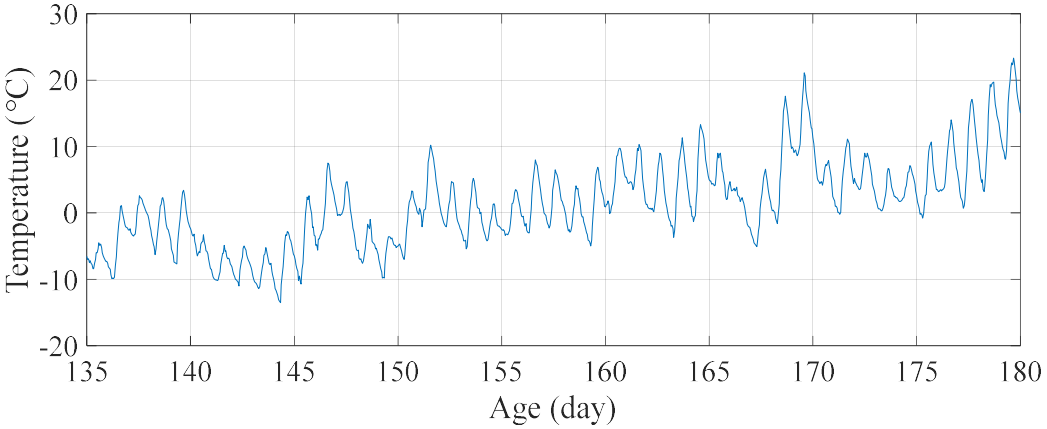

(a) Ambient temperature (Age of 135–180 days)

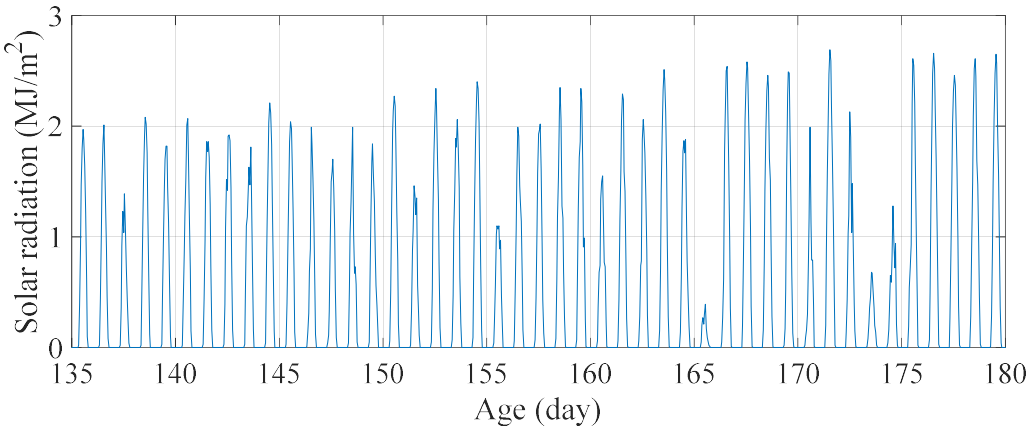

(b) Solar radiation (Age of 135–180 days)

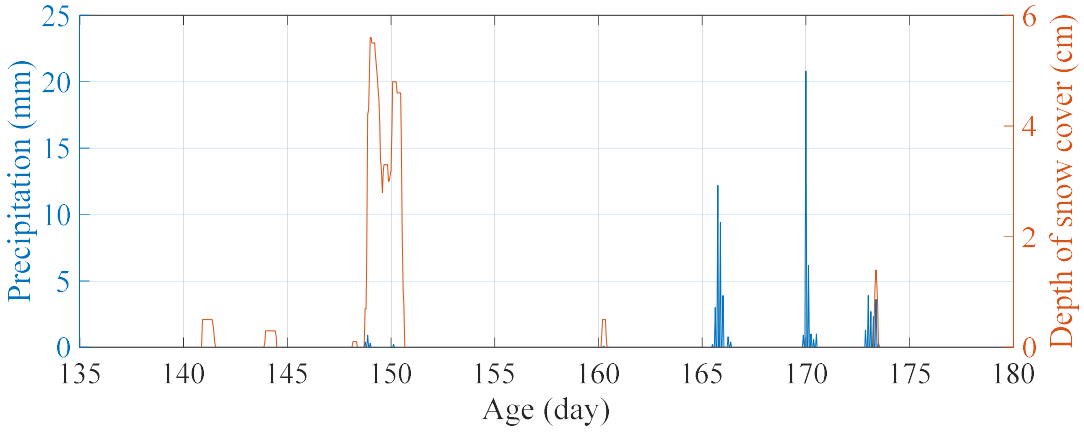

(c) Precipitation and depth of snow cover (Age of 135–180 days)

Figure 47. Weather conditions (Age of 135–180 days).

The bridge displacements after the slab placement are shown in Figure 48. Even though the barriers induced additional weight in 180th day, immediate displacement was limitedly observed. Other than the negligible weight, additional load was not applied during the age of 160–245 days (February 23, 2018–May 19, 2018); thereby displacement level converged to approximately 4 mm. Herein, the displacement at 160th and 230th days were nearly the same due to the convergence after 160th day. During this period, weather condition dominated the bridge behavior in absence of the mechanical deformations. Heavy rain in the age of 180–187, 200–203, and 218–221 days blocked direct sunlight resulting in small daily fluctuation. As can be seen in Figure 45, lower level of displacement was sustained during the rainy days because upward movement was not involved due to insufficient heat from the sunlight. In addition to the weather condition, insect swarm in front of the camera lens and target, as shown in Figure 60, resulted in the error for the dual cameras in the age of 223rd, 228th, 233rd, and 234th days. The dual cameras temporally stopped the measurement to solve the insect issue.

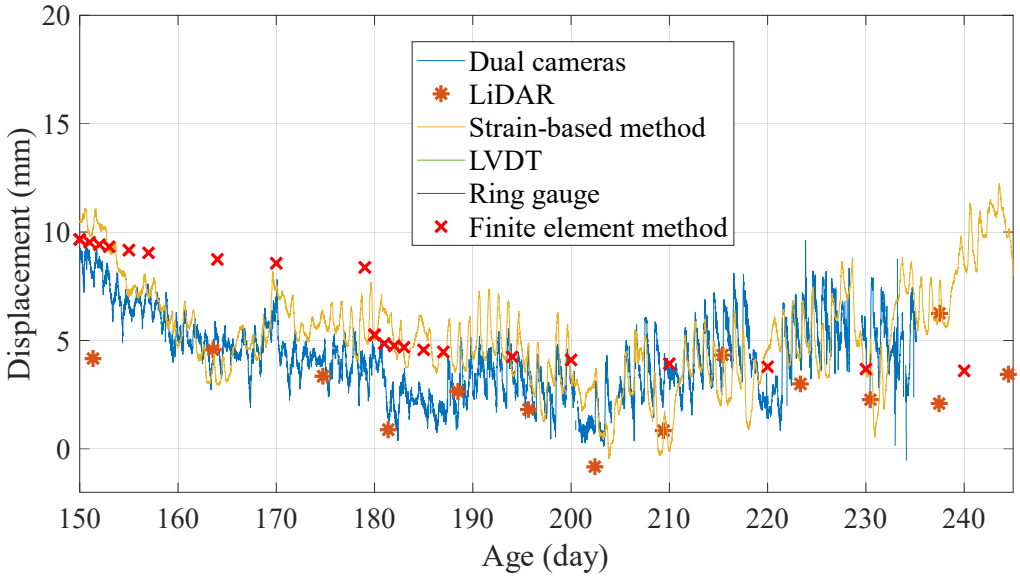

Figure 48. Long-term displacement comparison (Age of 150–245 days).

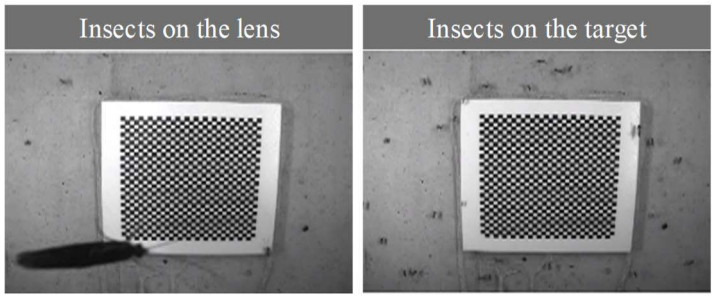

Figure 49. Images captured by the sub-camera.

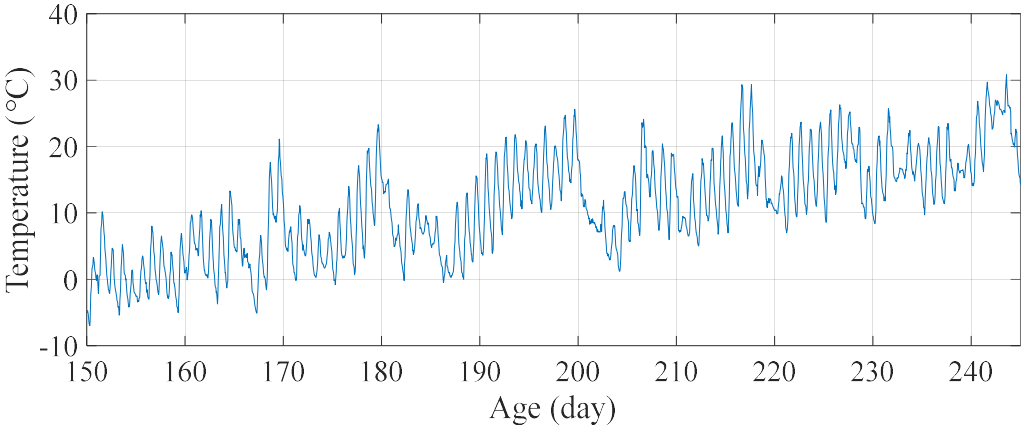

(a) Ambient temperature (Age of 150–245 days)

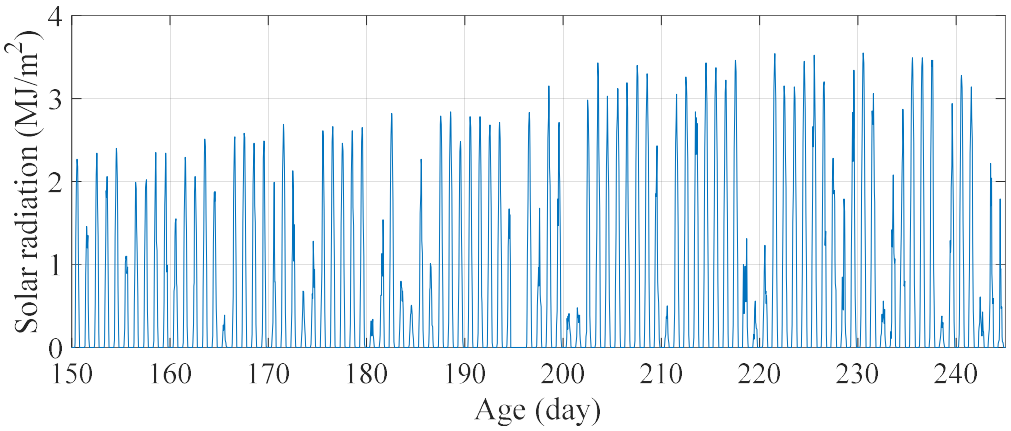

(b) Solar radiation (Age of 150–245 days)

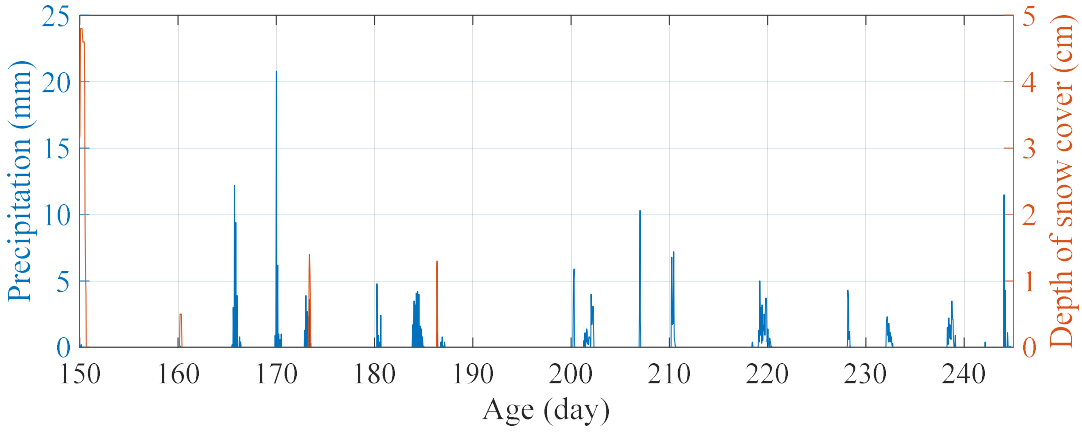

(c) Precipitation and depth of snow cover (Age of 150–245 days)

Figure 50. Weather conditions (Age of 150–245 days).

The bridge displacements during the ballast placement are shown in Figure 51. Dual cameras, of which measurement was paused due to the insect swarm, resumed at the age of 283 day. LVDT and ring gauge were installed at the age of 282 day for rigorous validation during the ballast placement. Until the age of 333 day when the ballast was placed, the displacement measured by dual cameras, LiDAR, LVDT, and ring gauge showed good agreement. On the other hand, the strain-based method was biased such that 10 mm higher displacement was measured. Herein, thermal expansion of the strain gauge, detachment of the gauge due to the expiry of the adhesive was the possible error source. No additional load was applied until the age of 333 day that weather condition shown in Figure 52 dominated daily fluctuation of the displacement. The ballast placement was followed on 333rd and 347th days. For the first phase of the ballast placement, 1.6 mm, 3.0 mm, 2.0 mm, 2.5 mm, and 2.4 mm of immediate displacement were measured via dual cameras, LiDAR, strain-based method, LVDT, and ring gauge, respectively. In the same order of the sensors, 0.9 mm, 2.0 mm, 1.6 mm, 1.6 mm, and 2.0 mm of the immediate displacement were respectively measured for the second phase of the ballast placement. The displacement development owing to the creep was observed during the age of 333–360 days, in which dual cameras and LVDT showed similar trend. In case of the LiDAR, a cable tie near a reflector, as shown in Figure 53(a) caused measurement error on 333rd and 356th day. The cable tie was removed on 356th day that stable level of displacement was observed after then. Heavy rain on 345th day drowned the ring gauge in a puddle as shown in Figure 53(b) , after which a large deviation was observed.

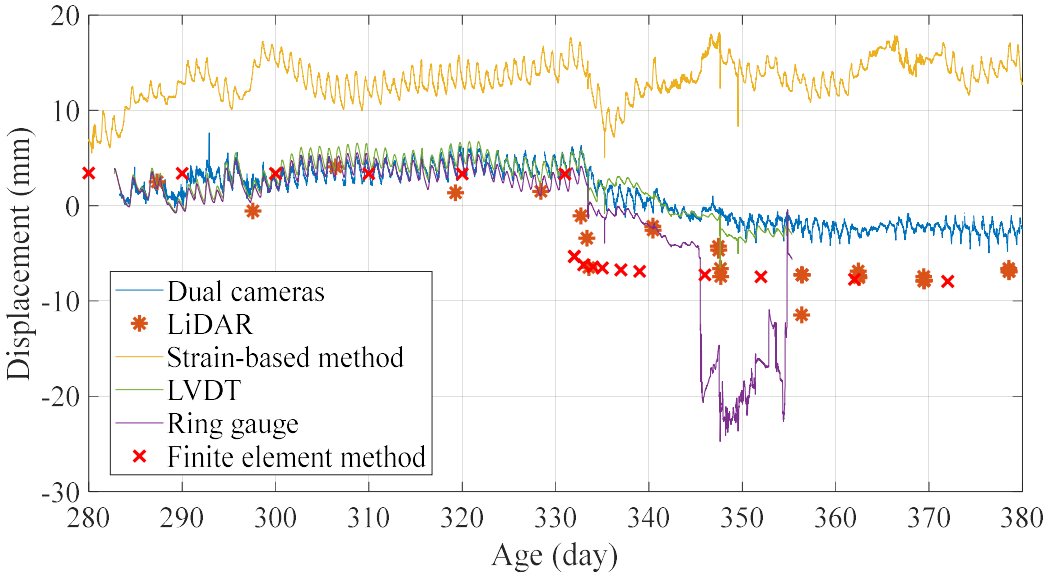

Figure 51. Long-term displacement comparison (Age of 280–380 days).

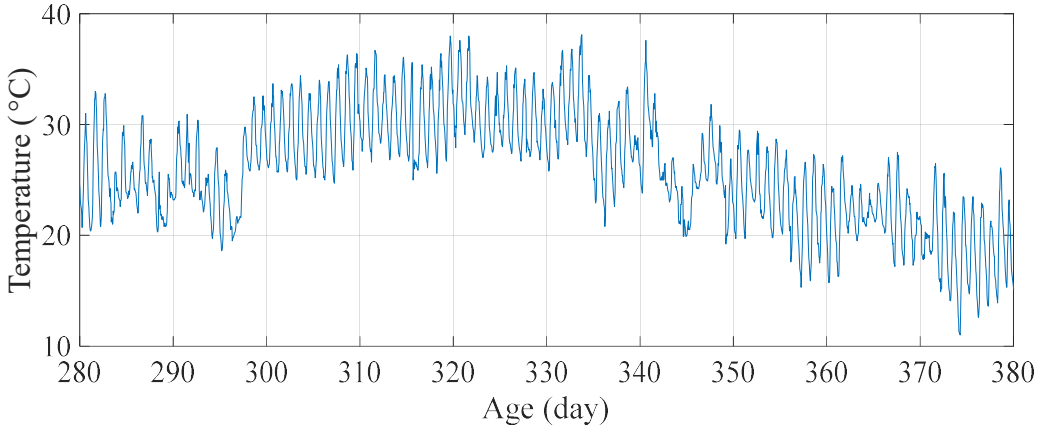

(a) Ambient temperature (Age of 280–380 days)

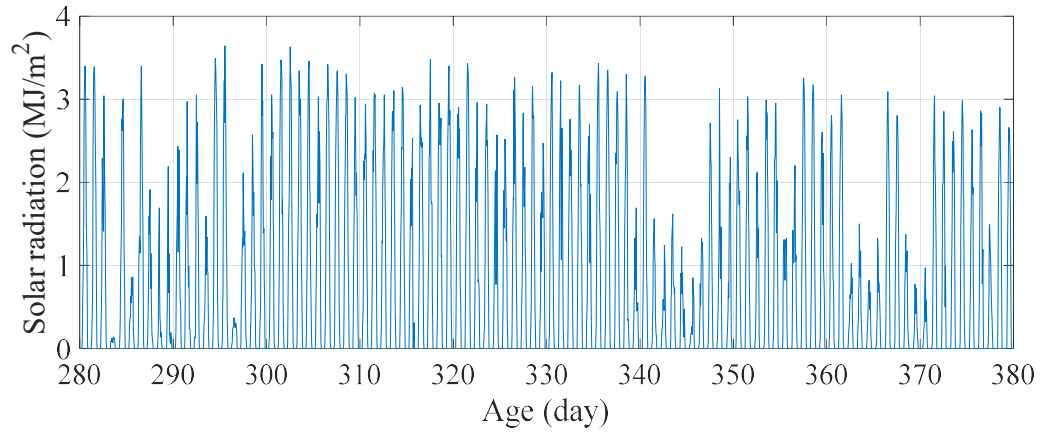

(b) Solar radiation (Age of 280–380 days)

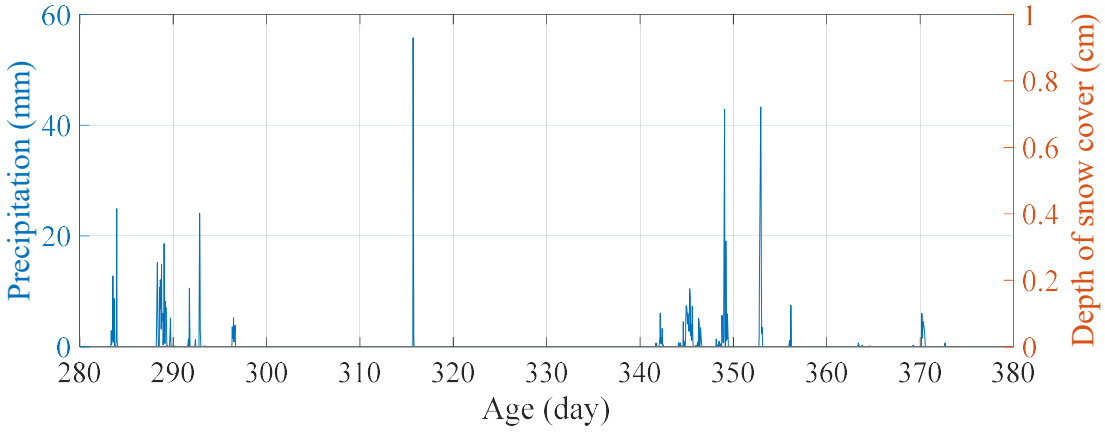

(c) Precipitation and depth of snow cover (Age of 280–380 days)

Figure 52. Weather conditions (Age of 280–380 days).

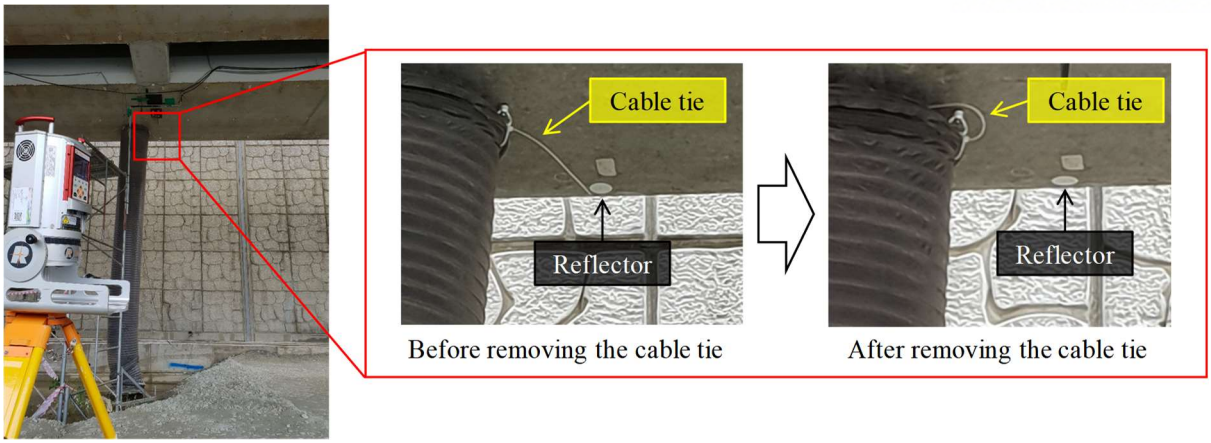

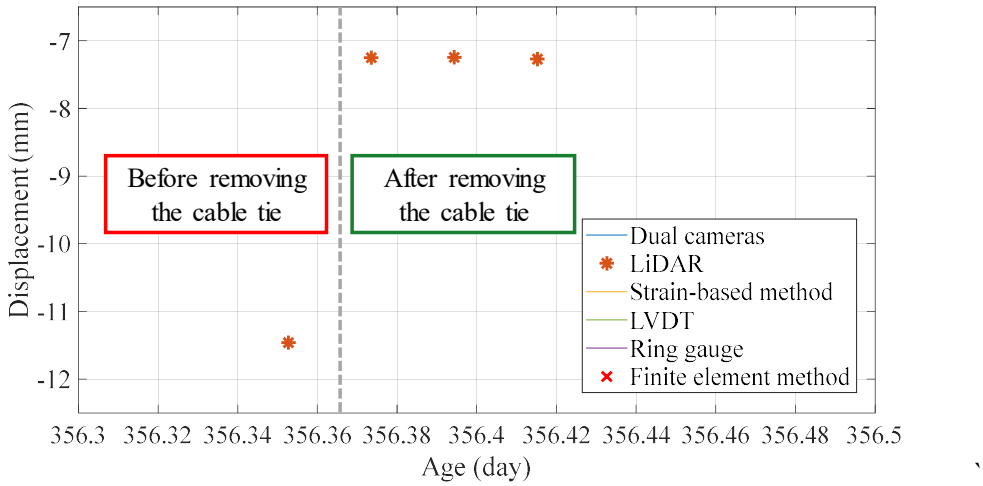

(a) LiDAR measurement error due to the cable tie in front of a reflector

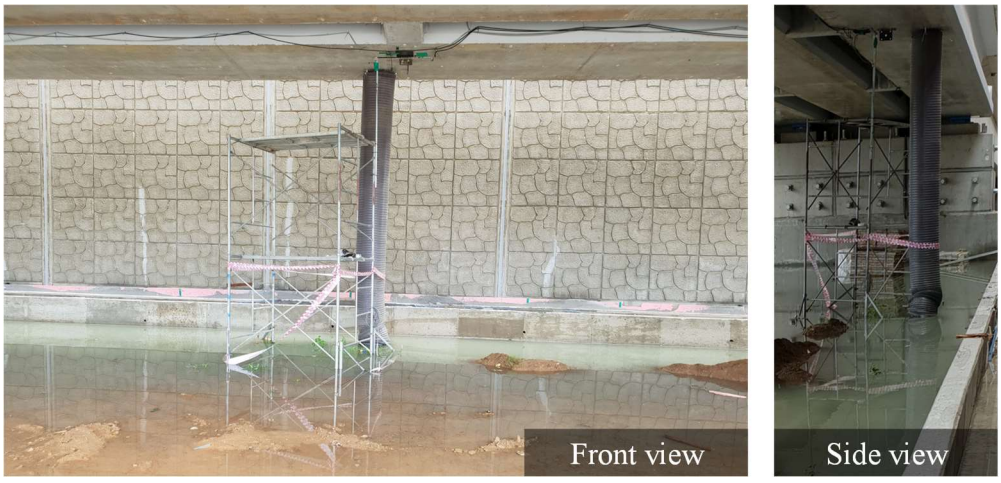

(b) Ring gauge measurement error due to a puddle

Figure 53. Displacement measurement error for LiDAR and ring gauge.

The bridge displacements during the age of 420–650 days are shown in Figure 54. Because the construction had been completed on 356th day, the measured displacement was mostly a response to weather conditions. The 462nd day was a winter solstice with low solar radiation and low temperature, as shown in Figure 56. The dual cameras and LiDAR measured low displacement of −6.7 mm and −8.3 mm, respectively, around the winter solstice. Similarly, −0.2 mm and 0.0 mm of high displacement were measured by the dual cameras and LiDAR around a summer solstice of the 644th day. The seasonal displacements in year 2019 were computed to be in the range of 6.5–8.3 mm. Even though dual cameras and LiDAR paused their operation for 50 days since 463rd day, displacement could be acquired without need for adjusting the starting point to the latest one. On the other hand, strain gauge stopped its operation due to the accumulation of the drift error. Pavement under the bridge as shown in Figure 55 caused two contact-type sensors, LVDT and ring gauge, to stop.

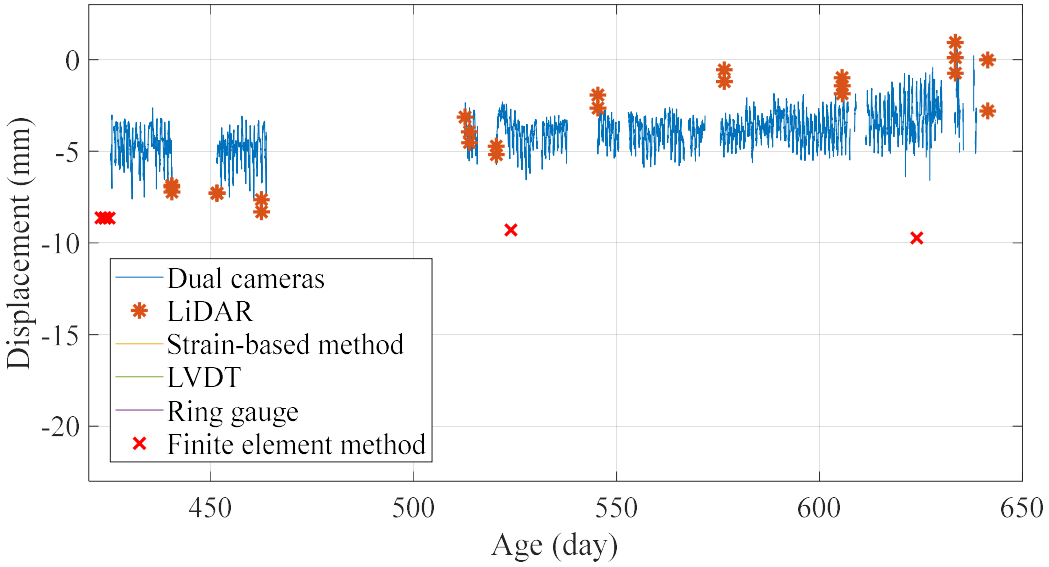

Figure 54. Long-term displacement comparison (Age of 420–650 days).

Figure 55. Preparation for the underpass pavement.

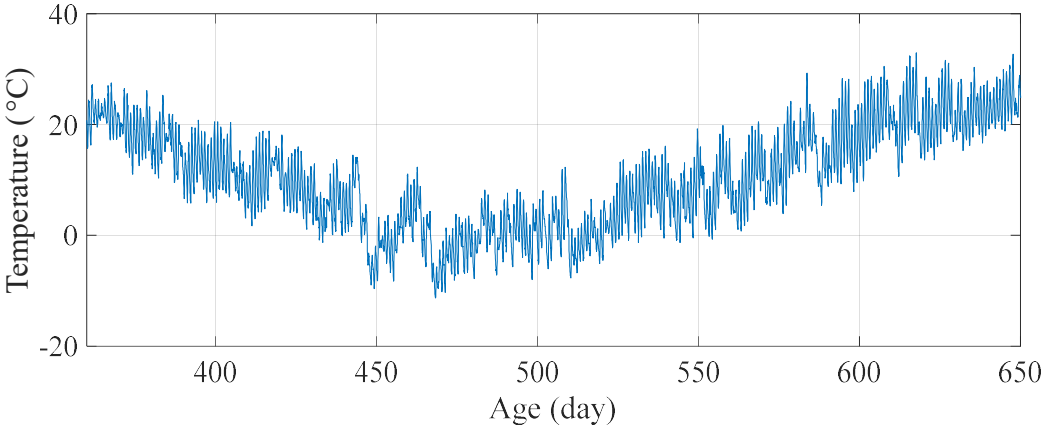

(a) Ambient temperature (Age of 420–650 days)

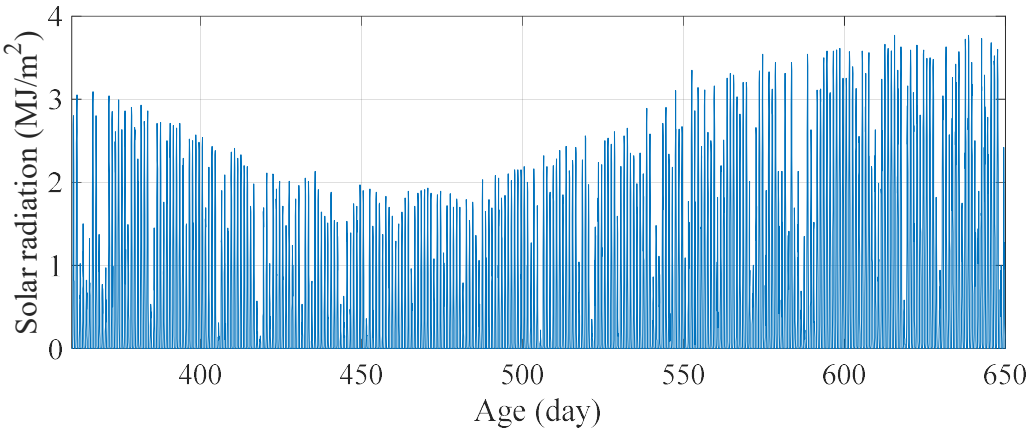

(b) Solar radiation (Age of 420–650 days)

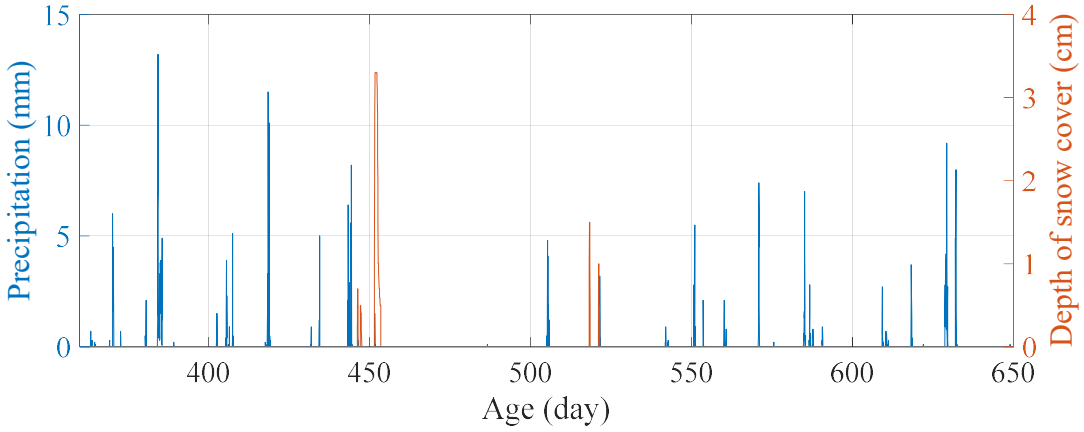

(c) Precipitation and depth of snow cover (Age of 420–650 days)

Figure 56. Weather conditions (Age of 420–650 days).

5.3. Performance of the proposed long-term displacement measurement methods

5.3.1. Discussion on vision-based long-term displacement measurement

The dual-camera system was designed to compensate for the false displacement induced by camera motion. Figure 57 shows the 6-DOF motions of the sub-camera with respect to *CS*(1). Even though the cameras were tightly fixed to the pier, the camera system was prone to move because of its self-weight and harsh weather conditions.

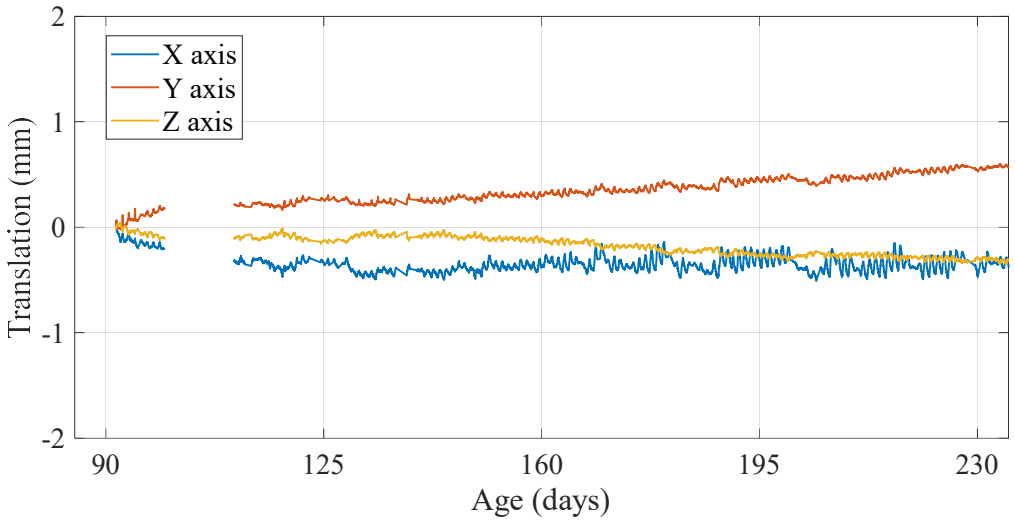

(a) Translational camera motion

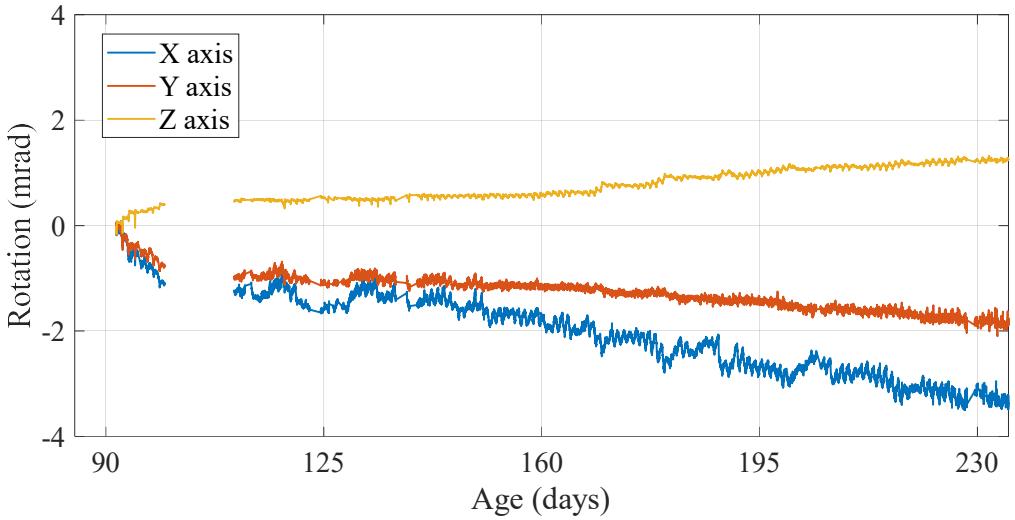

(b) Rotational camera motion

Figure 57. 6-DOF camera motions.

The camera motions resulted in the drift error shown in Figure 58, where the single camera (i.e., main camera only) measured a displacement 30 mm larger than that measured by the dual cameras. The false displacement was even greater than the true structural displacement, which clearly demonstrates why the camera motion-induced error must be removed for reliable long-term measurement. The dual-camera system was demonstrated to accurately measure the long-term structural displacement by compensating for the error due to camera motion.

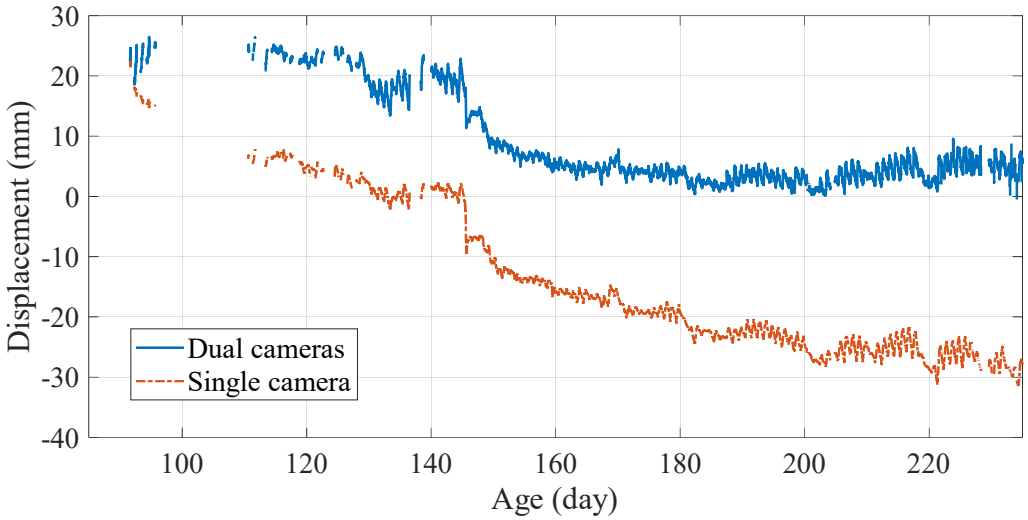

Figure 58. Comparison between the dual- and single-camera methods.

5.3.2. Discussion on LiDAR-based long-term displacement measurement

The 3D positions of the reflectors can be quickly and reliably estimated by focused scanning and binarization-based segmentation. Scanning a reflector with a diameter of 50 mm takes three minutes to produce 1,000 points at the pier and seven minutes to produce 25,000 points at the midspan; therefore, the total time taken to measure all points is less than one hour. Note that the large structural vibrations during the scanning can influence the resulting displacement; measurements need to be scheduled when the traffic is low. Given that the minimum number of points covering one reflector is 1,000, the standard deviation of the distance scan is expected to reduce from 5 mm for a single point to 0.16 mm for the centroid when considering central limit theorem [154]. In this respect, the centroid position provides a sufficient resolution and standard deviation to enable small displacement measurements to be made within one-hour scan.

Use of a 3D point cloud of the entire bridge was found to be inappropriate for measuring bridge displacement. The bridge was roughly scanned using an angular interval of 0.05 degrees (see Figure 59). Note that a detailed scan at a maximum resolution takes longer than 10 hours. The position data of the following two lines were manually extracted from the scanned point cloud: the southern line containing points b_1, b_3, and b_5 and the northern line containing points b_2, b_4, and b_6 as shown in Figure 38(a). Taking the average of the vertical components of the position data from the point cloud for every 2.5 m interval, the vertical positions along the longitudinal axis of the bridge were obtained, as shown in Figure 60. The resulting standard deviations of approximately 5 mm are shown as the I-shaped bars in Figure 60; this value is unacceptably large for measuring the displacement of short and medium span bridges.

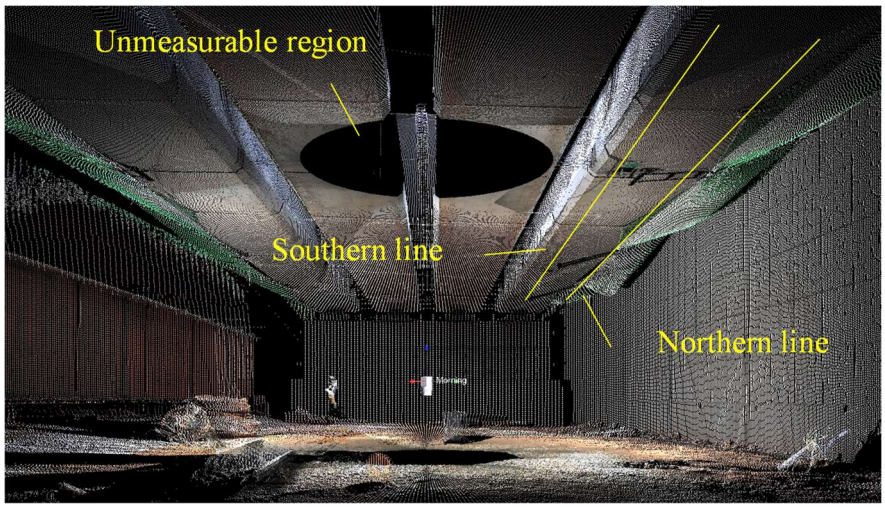

Figure 59. 3D point cloud of the bridge captured by LiDAR.

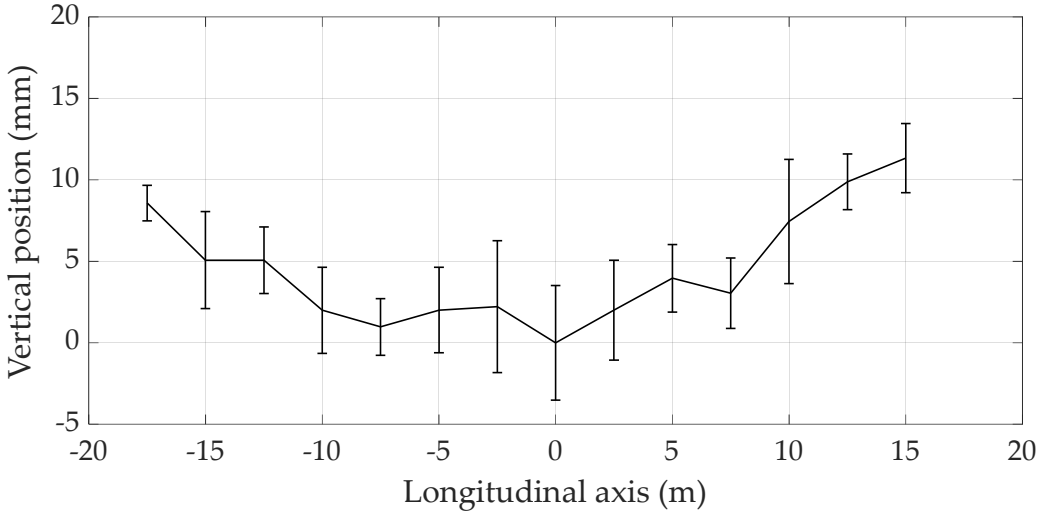

(a) Southern line

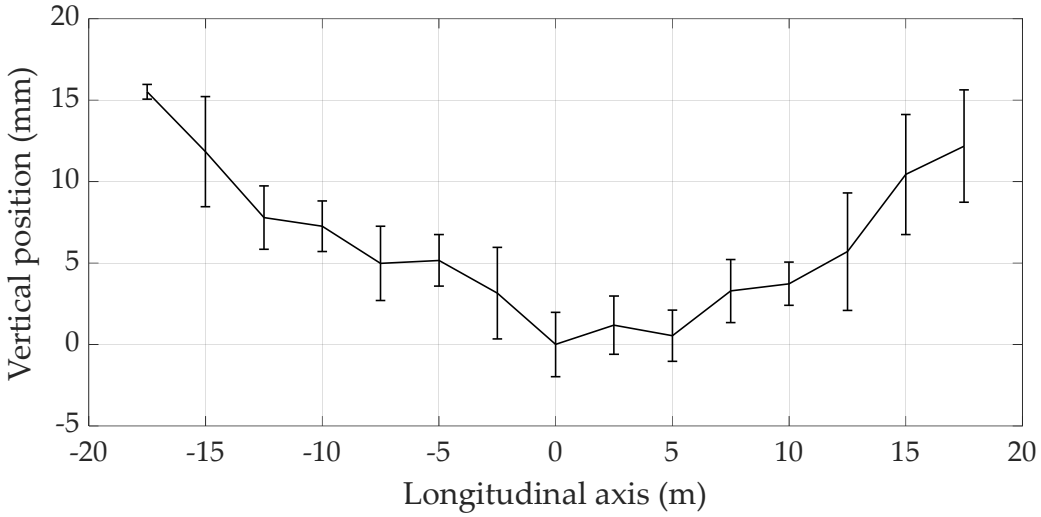

(b) Northern line

Figure 60. Vertical positions measured by scanning the entire bridge.

5.4. Summary and Discussion

The proposed long-term displacement measurement methods using dual camera and LiDAR are cross validated through a full-scale railway bridge in construction stage. For 650 days, both proposed methods show good agreement each other showing similar immediate displacement induced by slab and ballasts placement. Also, additional displacement induced by concrete creep was also observed. Dual camera system successfully compensated 30 mm of displacement error induced by the camera motion. LiDAR system with entire scanning method showed about 6 mm of variation within 2.5 m of span resulting in unreliable displacement measurement. Thus, the proposed methods are successfully cross validated that both systems can be employed for long-term displacement measurement of full-scale bridges.

6. Conclusions

Displacement is regarded as an important safety indicator that can be used to maintain bridge structures. The design codes typically regulate the maximum allowable displacement to assure passenger comfort during a bridge's designed lifetime. To accommodate the design codes in bridge management, numerous displacement measurement methods are developed for full-scale bridges, including contact-type sensors, non-contact type sensors, and indirect estimation. However, the conventional approaches have limitations in long-term monitoring, such as permanent underpass occupation, drift error induced by the sensor motion, and numerical integration error. For this reason, the long-term displacement has not been widely used. Hence, this study focused on developing a long-term displacement measurement method tailored to full-scale bridge structures by using computer vision and LiDAR.

First, a long-term displacement measurement system based on computer vision was proposed. Because the conventional vision-based approaches are adequate for measuring dynamic displacements with a fixed camera, an unexpected camera motion during the measurement may result in significant errors. The proposed system introduces main and sub-cameras to compensate for the motion-induced error during the displacement measurement. The main camera measures the structural displacement based on a conventional method and therefore, the camera motion-induced error is included in the measurement results. The sub-camera is rigidly attached to the main camera and measures its 6-DOF camera motions. The physical relationship between the 6-DOF camera motions and the motion-induced error is identified. This requires nine unknown parameters to be determined before the measurement. The unknown parameters are determined through the proposed calibration process, which allows the motion-induced error to be estimated for each frame. Removing the measurement error from the main camera allows to measure the true structural displacement. Thus, the proposed dual-camera system is designed to measure the long-term displacements.

Second, a LiDAR-based long-term displacement measurement method is proposed for full-scale bridge structures. Reflectors are strategically placed (instead of scanning the entire structure by the LiDAR) not only to reduce the time needed to take measurements, but also to achieve higher accuracy. A reflector deployment scheme is developed to provide the necessary information for the long-term displacement measurement. Each reflector position is calculated during the binarization-based post-processing, using the raw reflectance data measured by the LiDAR. The gravity vector is then determined using the reflectors in the measurement group to obtain the vertical displacement. The relative reflector vector is projected onto the gravity vector, thus yielding the vertical position of the reflector in the measurement group. Tracking the changes of the length along the vertical direction enables the determination of long-term displacement at the reflector location.

The proposed long-term displacement measurement methods are cross-validated using a full-scale railway bridge under construction. Over 650 days, both the long-term measurement approaches show good agreement each other showing similar immediate displacement induced by the dead load during construction. In addition to the immediate displacement, creep effect for each dead load are measured by the proposed systems. The measured long-term displacement was analyzed based on the environmental conditions, such as ambient temperature, solar radiation, snow, and rain affected long-term displacement. Thus, the proposed methods are successfully cross validated in the field test, presenting a strong potential for the long-term displacement data in the bridge SHM.

Long-term displacement provides essential information about the structural condition which can be useful for structural health monitoring of full-scale bridges. Bridge structures are continuously exposed to harsh field environment including traffics, winds, natural disaster, cracking, weather conditions, and so forth. In the meantime, bridge structures are gradually degraded without noticeable changes in structural behaviors. A continuous monitoring of bridge displacement can provide essential information about the structural integrity such as section loss, material degradation, change in boundary condition problem, prestress loss in tendon, and so forth. As such, the proposed long-term displacement measurement methods can be employed in condition monitoring of full-scale bridges.

REFERENCES

1. KICT, *A Study on Code System for Design Standards and Construction Specifications*, M.o.L.I.a. Transport, Editor. 2013.

2. AASHTO, *AASHTO LRFD Bridge design specifications*, A.A.o.S.H.a.T. Officials, Editor. 2017: Washington, DC.

3. Eurocode2, *Basis of structural design*, E.C.f. Standardization, Editor. 2002.

4. Wardhana, K. and F.C. Hadipriono, *Analysis of recent bridge failures in the United States.* Journal of Performance of Constructed Facilities, 2003. **17**(3): p. 144-150.

5. Imam, B. and M. Chryssanthopoulos. *A review of metallic bridge failure statistics*. in *Bridge Maintenance, Safety and Management: Proceedings of the Fifth International IABMAS Conference*. 2010.

6. Cau, B.T., N.H. Thap, and P.V. Khoi, *An overview of bridge failures in Vietnam*, in *Forensic Engineering*. 2003. p. 415-422.

7. Åkesson, B., *Understanding bridge collapses*. 2014: CRC press.

8. Jang, S., et al., *Structural health monitoring of a cable-stayed bridge using smart sensor technology: deployment and evaluation.* Smart Structures and Systems, 2010. **6**(5-6): p. 439-459.

9. Sohn, H., et al., *A review of structural health monitoring literature: 1996–2001.* Los Alamos National Laboratory, USA, 2003.

10. Nagayama, T. and B.F. Spencer Jr, *Structural health monitoring using smart sensors*. 2007, Newmark Structural Engineering Laboratory. University of Illinois at Urbana Champaign.

11. Ren, W.-X., T. Zhao, and I.E. Harik, *Experimental and analytical modal analysis of steel arch bridge.* Journal of Structural Engineering, 2004. **130**(7): p. 1022-1031.

12. Cho, S., et al., *Structural health monitoring of a cable-stayed bridge using wireless smart sensor technology: data analyses.* Smart Structures and Systems, 2010. **6**(5-6): p. 461-480.

13. Bocca, M., et al., *A synchronized wireless sensor network for experimental modal analysis in structural health monitoring.* Computer-Aided Civil and Infrastructure Engineering, 2011. **26**(7): p. 483-499.

14. Sabato, A., C. Niezrecki, and G. Fortino, *Wireless MEMS-based accelerometer sensor boards for structural vibration monitoring: a review.* IEEE Sensors Journal, 2016. **17**(2): p. 226-235.

15. Kim, D.-H. and M.Q. Feng, *Real-time structural health monitoring using a novel fiber-optic accelerometer system.* IEEE Sensors Journal, 2007. **7**(4): p. 536-543.

16. Shi, Z., S. Law, and L. Zhang, *Structural damage detection from modal strain energy change.* Journal of Engineering Mechanics, 2000. **126**(12): p. 1216-1223.

17. Yam, L., et al., *Theoretical and experimental study of modal strain analysis.* Journal of Sound and Vibration, 1996. **191**(2): p. 251-260.

18. Zhang, J., et al., *Structural identification and damage detection through long-gauge strain measurements.* Engineering Structures, 2015. **99**: p. 173-183.

19. Cui, H., et al., *A damage detection method based on strain modes for structures under ambient excitation.* Measurement, 2018. **125**: p. 438-446.

20. Esfandiari, A., et al., *Finite element model updating using frequency response function of incomplete strain data.* AIAA journal, 2010. **48**(7): p. 1420-1433.

21. Chan, T.H., et al., *Fiber Bragg grating sensors for structural health monitoring of Tsing Ma bridge: Background and experimental observation.* Engineering Structures, 2006. **28**(5): p. 648-659.

22. Catbas, F.N., M. Susoy, and D.M. Frangopol, *Structural health monitoring and reliability estimation: Long span truss bridge application with environmental monitoring data.* Engineering Structures, 2008. **30**(9): p. 2347-2359.

23. Tennyson, R., et al., *Structural health monitoring of innovative bridges in Canada with fiber optic sensors.* Smart Materials and Structures, 2001. **10**(3): p. 560.

24. Matta, F., et al., *Distributed strain measurement in steel bridge with fiber optic sensors: Validation through diagnostic load test.* Journal of performance of constructed facilities, 2008. **22**(4): p. 264-273.

25. Moschas, F. and S. Stiros, *Measurement of the dynamic displacements and of the modal frequencies of a short-span pedestrian bridge using GPS and an accelerometer.* Engineering Structures, 2011. **33**(1): p. 10-17.

26. Feng, D. and M.Q. Feng, *Vision-based multipoint displacement measurement for structural health monitoring.* Structural Control and Health Monitoring, 2016. **23**(5): p. 876-890.

27. Hoskere, V., et al., *Vision-Based Modal Survey of Civil Infrastructure Using Unmanned Aerial Vehicles.* Journal of Structural Engineering, 2019. **145**(7): p. 04019062.

28. Kim, S.-W. and N.-S. Kim, *Multi-point displacement response measurement of civil infrastructures using digital image processing.* Procedia Engineering, 2011. **14**: p. 195-203.

29. Lee, J.J., et al., *Development and application of a vision-based displacement measurement system for structural health monitoring of civil structures.* Smart Structures and Systems, 2007. **3**(3): p. 373-384.

30. Fu, T.S., et al., *Energy-efficient deployment strategies in structural health monitoring using wireless sensor networks.* Structural Control and Health Monitoring, 2013. **20**(6): p. 971-986.

31. He, C., et al., *A combined optimal sensor placement strategy for the structural health monitoring of bridge structures.* International Journal of Distributed Sensor Networks, 2013. **9**(11): p. 820694.

32. Cho, S., et al. *Structural health monitoring system of a cable-stayed bridge using a dense array*

of scalable smart sensor network. in *Sensors and Smart Structures Technologies for Civil, Mechanical, and Aerospace Systems 2010*. 2010. International Society for Optics and Photonics.

33. Kurata, M., et al. *Long-term assessment of an autonomous wireless structural health monitoring system at the new Carquinez Suspension Bridge*. in *Nondestructive Characterization for Composite Materials, Aerospace Engineering, Civil Infrastructure, and Homeland Security 2011*. 2011. International Society for Optics and Photonics.

34. Sazonov, E., K. Janoyan, and R. Jha. *Wireless intelligent sensor network for autonomous structural health monitoring*. in *Smart Structures and Materials 2004: Smart Sensor Technology and Measurement Systems*. 2004. International Society for Optics and Photonics.

35. Chae, M., et al., *Development of a wireless sensor network system for suspension bridge health monitoring.* Automation in Construction, 2012. **21**: p. 237-252.

36. Pakzad, S.N. and G.L. Fenves, *Statistical analysis of vibration modes of a suspension bridge using spatially dense wireless sensor network.* Journal of Structural Engineering, 2009. **135**(7): p. 863-872.

37. Sim, S.-H., et al., *Decentralized random decrement technique for efficient data aggregation and system identification in wireless smart sensor networks.* Probabilistic Engineering Mechanics, 2011. **26**(1): p. 81-91.

38. Ni, Y., et al., *Correlating modal properties with temperature using long-term monitoring data and support vector machine technique.* Engineering Structures, 2005. **27**(12): p. 1762-1773.

39. Carden, E.P. and P. Fanning, *Vibration based condition monitoring: a review.* Structural Health Monitoring, 2004. **3**(4): p. 355-377.

40. Peeters, B. and C. Ventura, *Comparative study of modal analysis techniques for bridge dynamic characteristics.* Mechanical Systems and Signal Processing, 2003. **17**(5): p. 965-988.

41. Rainieri, C. and G. Fabbrocino, *Automated output-only dynamic identification of civil engineering structures.* Mechanical Systems and Signal Processing, 2010. **24**(3): p. 678-695.

42. Ye, X.-W., Y.-H. Su, and P.-S. Xi, *Statistical analysis of stress signals from bridge monitoring by FBG system.* Sensors, 2018. **18**(2): p. 491.

43. Cardini, A. and J.T. DeWolf, *Long-term structural health monitoring of a multi-girder steel composite bridge using strain data.* Structural Health Monitoring, 2009. **8**(1): p. 47-58.

44. Garber, D.B., et al., *Experimental investigation of prestress losses in full-scale bridge girders.* ACI Structural Journal, 2015. **112**(5): p. 553.

45. Kim, J.-T. and N. Stubbs, *Crack detection in beam-type structures using frequency data.* Journal of Sound and Vibration, 2003. **259**(1): p. 145-160.

46. Park, S., et al., *Multiple crack detection of concrete structures using impedance-based structural health monitoring techniques.* Experimental mechanics, 2006. **46**(5): p. 609-618.

47. Nishikawa, T., et al., *Concrete crack detection by multiple sequential image filtering.* Computer-Aided Civil and Infrastructure Engineering, 2012. **27**(1): p. 29-47.

48. Abdel-Qader, I., O. Abudayyeh, and M.E. Kelly, *Analysis of edge-detection techniques for crack identification in bridges.* Journal of Computing in Civil Engineering, 2003. **17**(4): p. 255-263.

49. McCann, D. and M. Forde, *Review of NDT methods in the assessment of concrete and masonry structures.* Ndt & E International, 2001. **34**(2): p. 71-84.

50. Kim, H., et al., *Crack and noncrack classification from concrete surface images using machine learning.* Structural Health Monitoring, 2019. **18**(3): p. 725-738.

51. Cha, Y.J., W. Choi, and O. Büyüköztürk, *Deep learning-based crack damage detection using convolutional neural networks.* Computer-Aided Civil and Infrastructure Engineering, 2017. **32**(5): p. 361-378.

52. Chen, F.-C. and M.R. Jahanshahi, *NB-CNN: deep learning-based crack detection using convolutional neural network and Naïve Bayes data fusion.* IEEE Transactions on Industrial Electronics, 2017. **65**(5): p. 4392-4400.

53. Kim, I.-H., et al., *Application of crack identification techniques for an aging concrete bridge inspection using an unmanned aerial vehicle.* Sensors, 2018. **18**(6): p. 1881.

54. Fan, W. and P. Qiao, *Vibration-based damage identification methods: a review and comparative study.* Structural Health Monitoring, 2011. **10**(1): p. 83-111.

55. Pandey, A. and M. Biswas, *Damage detection in structures using changes in flexibility.* Journal of Sound and Vibration, 1994. **169**(1): p. 3-17.

56. Chang, P.C., A. Flatau, and S. Liu, *Health monitoring of civil infrastructure.* Structural health monitoring, 2003. **2**(3): p. 257-267.

57. Wahab, M.A. and G. De Roeck, *Damage detection in bridges using modal curvatures: application to a real damage scenario.* Journal of Sound and Vibration, 1999. **226**(2): p. 217-235.

58. Zonta, D. and D. Bernal. *Strain-based approaches to damage localization in civil structures*. in *IMAC XXIV*. 2006. St. Louis, USA.

59. Bagchi, A., *Updating the mathematical model of a structure using vibration data.* Modal Analysis, 2005. **11**(12): p. 1469-1486.

60. Friswell, M., D. Inman, and D.F. Pilkey, *Direct updating of damping and stiffness matrices.* AIAA journal, 1998. **36**(3): p. 491-493.

61. Mottershead, J.E. and M. Friswell, *Model updating in structural dynamics: a survey.* Journal of Sound and Vibration, 1993. **167**(2): p. 347-375.

62. Imregun, M., W. Visser, and D. Ewins, *Finite element model updating using frequency response function data: I. Theory and initial investigation.* Mechanical Systems and Signal Processing, 1995. **9**(2): p. 187-202.

63. Farhat, C. and F.M. Hemez, *Updating finite element dynamic models using an element-by-element sensitivity methodology.* AIAA journal, 1993. **31**(9): p. 1702-1711.

64. Friswell, M. and J.E. Mottershead, *Finite element model updating in structural dynamics*. Vol. 38. 2013: Springer Science & Business Media.

65. Administration, F.H., *National bridge inspection standards*, in *Fed. Regist.* 2009. p. 68377-68379.

66. Ritter, M.A., *Timber bridges: Design, construction, inspection, and maintenance*. 1990: US Department of Agriculture, Forest Service, Engineering Staff.

67. Koh, H.M., et al., *Monitoring of Bridges in K orea.* Encyclopedia of Structural Health Monitoring, 2009.

68. Institute, K.R.R., *Construction Rule and Regulation on Korean Railroad*. 2017.

69. Thong, Y., et al., *Numerical double integration of acceleration measurements in noise.* Measurement, 2004. **36**(1): p. 73-92.

70. Lee, H.S., Y.H. Hong, and H.W. Park, *Design of an FIR filter for the displacement reconstruction using measured acceleration in low-frequency dominant structures.* International Journal for Numerical Methods in Engineering, 2010. **82**(4): p. 403-434.

71. Artese, S., V. Achilli, and R. Zinno, *Monitoring of bridges by a laser pointer: dynamic measurement of support rotations and elastic line displacements: methodology and first test.* Sensors, 2018. **18**(2): p. 338.

72. Yau, M.H., *Vertical displacement measurement using fibre Bragg grating (FBG) sensors for structural health monitoring of bridges*. 2014, Queensland University of Technology.

73. Kim, N.-S. and N.-S. Cho, *Estimating deflection of a simple beam model using fiber optic Bragg-grating sensors.* Experimental mechanics, 2004. **44**(4): p. 433-439.

74. Shin, S., et al., *Estimation of bridge displacement responses using FBG sensors and theoretical mode shapes.* Structural Engineering Mechanics, 2012. **42**(2): p. 229-245.

75. Park, J.-W., S.-H. Sim, and H.-J. Jung, *Displacement estimation using multimetric data fusion.* IEEE/ASME Transactions on Mechatronics, 2013. **18**(6): p. 1675-1682.

76. Sousa, H., et al., *Bridge deflection evaluation using strain and rotation measurements.* Smart Structures and Systems, 2013. **11**(4): p. 365-386.

77. Dissanayake, P., *Health Monitoring of Structures Using Modern Tools.* Engineer: Journal of the Institution of Engineers, Sri Lanka, 2008. **41**(2).

78. Xia, H., et al., *Experimental analysis of a high-speed railway bridge under Thalys trains.* Journal of Sound and Vibration, 2003. **268**(1): p. 103-113.

79. Cho, S., J. Lee, and S.-H. Sim, *Comparative study on displacement measurement sensors for high-speed railroad bridge.* Smart Structures and Systems, 2018. **21**(5): p. 637-652.

80. Avallone, E., T. Baumeister, and A. Sadegh, *Marks' Standard Handbook for Mechanical Engineers*. 11 ed. 2006: New York: McGraw-Hill.

81. Qian, Z., Y. Fan, and Z. Lu. *Application of draw-wire displacement sensors on structural health monitoring of Jiangyin Bridge*. in *Nondestructive Evaluation and Health Monitoring of Aerospace Materials, Composites, and Civil Infrastructure V*. 2006. International Society for Optics and Photonics.

82. Bagge, N., et al. *Punching capacity of a reinforced concrete bridge deck slab loaded to failure*. in *Nordic Concrete Federation: Residual capacity of deteriorated concrete structure*. 2015.

83. Nassif, H.H., M. Gindy, and J. Davis, *Comparison of laser Doppler vibrometer with contact sensors for monitoring bridge deflection and vibration.* Ndt & E International, 2005. **38**(3): p. 213-218.

84. Nassif, H.H., M. Gindy, and J. Davis. *Monitoring of bridge girder deflection using laser Doppler vibrometer*. in *The 10th international converence and exhibition-structural faults and repair conference 2004*. 2003. London, UK.

85. Castellini, P., M. Martarelli, and E. Tomasini, *Laser Doppler Vibrometry: Development of advanced solutions answering to technology's needs.* Mechanical Systems and Signal Processing, 2006. **20**(6): p. 1265-1285.

86. Kim, K. and H. Sohn, *Dynamic displacement estimation by fusing LDV and LiDAR measurements via smoothing based Kalman filtering.* Mechanical Systems and Signal Processing, 2017. **82**: p. 339-355.

87. Pieraccini, M., *Monitoring of civil infrastructures by interferometric radar: A review.* The Scientific World Journal, 2013. **2013**.

88. Pieraccini, M., et al., *High-speed CW step-frequency coherent radar for dynamic monitoring of civil engineering structures.* Electronics Letters, 2004. **40**(14): p. 907-908.

89. Gentile, C. and G. Bernardini, *Output-only modal identification of a reinforced concrete bridge from radar-based measurements.* Ndt & E International, 2008. **41**(7): p. 544-553.

90. Dei, D., et al., *Detection of vertical bending and torsional movements of a bridge using a coherent radar.* Ndt & E International, 2009. **42**(8): p. 741-747.

91. Zhang, Z., et al., *A new laser displacement sensor based on triangulation for gauge real-time measurement.* Optics & Laser Technology, 2008. **40**(2): p. 252-255.

92. Li, S., et al., *Error analysis and correction for color in laser triangulation measurement.* Optik, 2018. **168**: p. 165-173.

93. Jo, H., et al., *Feasibility of displacement monitoring using low-cost GPS receivers.* Structural Control and Health Monitoring, 2013. **20**(9): p. 1240-1254.

94. Im, S.B., S. Hurlebaus, and Y.J. Kang, *Summary review of GPS technology for structural health monitoring.* Journal of Structural Engineering, 2011. **139**(10): p. 1653-1664.

95. Celebi, M., et al., *GPS monitoring of dynamic behavior of long-period structures.* Earthquake Spectra, 1999. **15**: p. 55-66.

96. Fujino, Y., et al. *Monitoring system of the Akashi Kaikyo Bridge and displacement measurement*

using GPS. in *Nondestructive Evaluation of Highways, Utilities, and Pipelines IV*. 2000. International Society for Optics and Photonics.

97. Watson, C., T. Watson, and R. Coleman, *Structural monitoring of cable-stayed bridge: analysis of GPS versus modeled deflections.* Journal of Surveying Engineering, 2007. **133**(1): p. 23-28.

98. Burdet, O. *Experience in the long-term monitoring of bridges*. in *3rd fib International Congress*. 2010. 3rd fib International Congress.

99. Psimoulis, P.A. and S.C. Stiros, *Measuring deflections of a short-span railway bridge using a robotic total station.* Journal of Bridge Engineering, 2013. **18**(2): p. 182-185.

100. Stiros, S.C. and P.A. Psimoulis, *Response of a historical short-span railway bridge to passing trains: 3-D deflections and dominant frequencies derived from Robotic Total Station (RTS) measurements.* Engineering Structures, 2012. **45**: p. 362-371.

101. Cosser, E., et al. *Measuring the dynamic deformation of bridges using a total station*. in *Proceeding of the 11th FIG symposium on deformation measurements*. 2003. Santorini, Greece.

102. Attanayake, U., et al. *Non-contact bridge deflection measurement: Application of laser technology*. in *Proceedings of the Integrating Generations FIG Working Week, Stockholm*. 2013. Stockholm, Sweden.

103. Park, H.S., et al., *A new approach for health monitoring of structures: terrestrial laser scanning.* Computer-Aided Civil and Infrastructure Engineering, 2007. **22**(1): p. 19-30.

104. Fuchs, P., et al., *Laser-based instrumentation for bridge load testing.* Journal of Performance of constructed facilities, 2004. **18**(4): p. 213-219.

105. Lee, J., et al., *Computer vision-based structural displacement measurement robust to light-induced image degradation for in-service bridges.* Sensors, 2017. **17**(10): p. 2317.

106. Kim, K., et al., *Structural displacement estimation through multi-rate fusion of accelerometer and RTK-GPS displacement and velocity measurements.* Measurement, 2018. **130**: p. 223-235.

107. Koo, G., et al., *Development of a high precision displacement measurement system by fusing a low cost RTK-GPS sensor and a force feedback accelerometer for infrastructure monitoring.* Sensors, 2017. **17**(12): p. 2745.

108. LAMBROU, E. and G. PANTAZIS, *Geodetic monitoring of bridge oscillations.*

109. Xu, Y., et al., *Long-span bridges: Enhanced data fusion of GPS displacement and deck accelerations.* Engineering Structures, 2017. **147**: p. 639-651.

110. Chetverikov, D., et al. *The trimmed iterative closest point algorithm*. in *Object recognition supported by user interaction for service robots*. 2002. IEEE.

111. Yu, J., et al., *Experimental assessment of high sampling-rate robotic total station for monitoring bridge dynamic responses.* Measurement, 2017. **104**: p. 60-69.

112. Fukuda, Y., et al., *Vision-based displacement sensor for monitoring dynamic response using robust object search algorithm.* IEEE Sensors Journal, 2013. **13**(12): p. 4725-4732.

113. Feng, M.Q., et al., *Nontarget vision sensor for remote measurement of bridge dynamic response.* Journal of Bridge Engineering, 2015. **20**(12): p. 04015023.

114. Yoon, H., et al., *Target-free approach for vision-based structural system identification using consumer-grade cameras.* Structural Control and Health Monitoring, 2016. **23**(12): p. 1405-1416.

115. Shariati, A., T. Schumacher, and N. Ramanna, *Eulerian-based virtual visual sensors to detect natural frequencies of structures.* Journal of Civil Structural Health Monitoring, 2015. **5**(4): p. 457-468.

116. Schumacher, T. and A. Shariati, *Monitoring of structures and mechanical systems using virtual visual sensors for video analysis: Fundamental concept and proof of feasibility.* Sensors, 2013. **13**(12): p. 16551-16564.

117. Feng, D., et al., *A vision-based sensor for noncontact structural displacement measurement.* Sensors, 2015. **15**(7): p. 16557-16575.

118. Wahbeh, A.M., J.P. Caffrey, and S.F. Masri, *A vision-based approach for the direct measurement of displacements in vibrating systems.* Smart Materials and Structures, 2003. **12**(5): p. 785.

119. Choi, H.-S., et al., *Structural dynamic displacement vision system using digital image processing.* NDT & E International, 2011. **44**(7): p. 597-608.

120. Lee, J.J. and M. Shinozuka, *A vision-based system for remote sensing of bridge displacement.* Ndt & E International, 2006. **39**(5): p. 425-431.

121. Fukuda, Y., M.Q. Feng, and M. Shinozuka, *Cost-effective vision-based system for monitoring dynamic response of civil engineering structures.* Structural Control and Health Monitoring, 2010. **17**(8): p. 918-936.

122. Song, Y.-Z., et al., *Virtual visual sensors and their application in structural health monitoring.* Structural Health Monitoring, 2014. **13**(3): p. 251-264.

123. Zhao, X., et al., *Bridge displacement monitoring method based on laser projection-sensing technology.* Sensors, 2015. **15**(4): p. 8444-8463.

124. Shariati, A. and T. Schumacher, *Eulerian-based virtual visual sensors to measure dynamic displacements of structures.* Structural Control and Health Monitoring, 2017. **24**(10): p. e1977.

125. Chang, C. and X. Xiao, *Three-dimensional structural translation and rotation measurement using monocular videogrammetry.* Journal of engineering mechanics, 2009. **136**(7): p. 840-848.

126. Ji, Y. *A computer vision-based approach for structural displacement measurement*. in *Sensors and Smart Structures Technologies for Civil, Mechanical, and Aerospace Systems 2010*. 2010. International Society for Optics and Photonics.

127. Jeon, H., et al., *Vision-based remote 6-DOF structural displacement monitoring system using a unique marker.* Smart Structures and Systems, 2014. **13**(6): p. 927-942.

128. Kim, S.-W., et al., *Vision-based monitoring system for evaluating cable tensile forces on a*

cable-stayed bridge. Structural Health Monitoring, 2013. **12**(5-6): p. 440-456.

129. Ye, X., et al., *Vision-based structural displacement measurement: System performance evaluation and influence factor analysis.* Measurement, 2016. **88**: p. 372-384.

130. Spontón, H. and J. Cardelino, *A review of classic edge detectors.* Image Processing on Line, 2015. **5**: p. 90-123.

131. Han, K.T.M. and B. Uyyanonvara. *A survey of blob detection algorithms for biomedical images*. in *7th International Conference of Information and Communication Technology for Embedded Systems (IC-ICTES)*. 2016. IEEE.

132. Mokhtarian, F. and F. Mohanna, *Performance evaluation of corner detectors using consistency and accuracy measures.* Computer Vision and Image Understanding, 2006. **102**(1): p. 81-94.

133. Wu, L.-J., F. Casciati, and S. Casciati, *Dynamic testing of a laboratory model via vision-based sensing.* Engineering Structures, 2014. **60**: p. 113-125.

134. Dworakowski, Z., et al., *Vision-based algorithms for damage detection and localization in structural health monitoring.* Structural Control and Health Monitoring, 2016. **23**(1): p. 35-50.

135. Kohut, P., K. Holak, and A. Martowicz, *An uncertainty propagation in developed vision based measurement system aided by numerical and experimental tests.* Journal of Theoretical and Applied Mechanics, 2012. **50**(4): p. 1049-1061.

136. Jeong, Y., D. Park, and K. Park, *PTZ camera-based displacement sensor system with perspective distortion correction unit for early detection of building destruction.* Sensors, 2017. **17**(3): p. 430.

137. Sładek, J., et al., *Development of a vision based deflection measurement system and its accuracy assessment.* Measurement, 2013. **46**(3): p. 1237-1249.

138. Cao, G.H., et al., *Long-term deflection test and theoretical analysis on cracked prestressed concrete box beams.* KSCE Journal of Civil Engineering, 2018. **22**(2): p. 688-695.

139. Xu, Y., et al., *Monitoring temperature effect on a long suspension bridge.* Structural Control and Health Monitoring, 2010. **17**(6): p. 632-653.

140. Beltempo, A., et al., *A Viscoelastic Model for the Long-Term Deflection of Segmental Prestressed Box Girders.* Computer-Aided Civil and Infrastructure Engineering, 2018. **33**(1): p. 64-78.

141. Chen, J.G., et al., *Video camera–based vibration measurement for civil infrastructure applications.* Journal of Infrastructure Systems, 2016. **23**(3): p. B4016013.

142. Yoon, H., J. Shin, and B.F. Spencer Jr, *Structural displacement measurement using an unmanned aerial system.* Computer-Aided Civil and Infrastructure Engineering, 2018. **33**(3): p. 183-192.

143. Hartley, R. and A. Zisserman, *Multiple view geometry in computer vision second edition.* Cambridge University Press, 2000.

144. Watson, C., et al., *Three-dimensional terrestrial LIDAR for operational bridge clearance measurements.* Journal of Performance of Constructed Facilities, 2011. **26**(6): p. 803-811.

145. Santos, C.A., C.O. Costa, and J. Batista, *A vision-based system for measuring the displacements of large structures: Simultaneous adaptive calibration and full motion estimation.* Mechanical Systems and Signal Processing, 2016. **72**: p. 678-694.

146. Ben-Israel, A. and T.N. Greville, *Generalized inverses: theory and applications*. Vol. 15. 2003: Springer Science & Business Media.

147. Zhang, Z. *Flexible camera calibration by viewing a plane from unknown orientations*. in *ICCV*. 1999.

148. Fuchs, P., et al., *Applications of laser-based instrumentation for highway bridges.* Journal of Bridge Engineering, 2004. **9**(6): p. 541-549.

149. Otsu, N., *A threshold selection method from gray-level histograms.* IEEE transactions on systems, man, and cybernetics, 1979. **9**(1): p. 62-66.

150. Ltd., M.I.T.C. *Midas Civil*. [cited 2019 05 July]; Available from: https://en.midasuser.com/product/civil_overview.asp.

151. KCI, *The Korean Concrete Structure Design Code*. 2012, Korea Concrete Institute Seoul, Korea.

152. Shin, S., et al., *Estimation of bridge displacement responses using FBG sensors and theoretical mode shapes.* Structural Engineering and Mechanics, 2012. **42**(2): p. 229-245.

153. Administration, K.M. [cited 2019 2 December]; Available from: https://data.kma.go.kr/cmmn/main.do.

154. Durrett, R., *Probability: theory and examples*. Vol. 49. 2019: Cambridge university press.